The Role of Gas in Star Cluster Formation

The Role of Gas in Star Cluster Formation

By
JEREMY KARAM,
B.Sc., M.Sc.

A Thesis Submitted to the School of Graduate Studies
in the Partial Fulfillment of the Requirements for the Degree of

Doctor of Philosophy
in
Physics and Astronomy

McMaster University
Hamilton, Ontario

Doctor of Philosophy (2025)
Physics & Astronomy
McMaster University
Hamilton, Ontario, Canada

TITLE: The Role of Gas in Star Cluster Formation

AUTHOR:
Jeremy Karam,
M.Sc. (Physics and Astronomy)

SUPERVISOR:
Alison Sills
Professor, Physics and Astronomy,
McMaster University, ON, Canada

SUPERVISORY COMMITTEE MEMBERS:
Dr. Ralph Pudritz
Professor, Department of Physics and Astronomy,
McMaster University, ON, Canada

Dr. James Wadsley
Professor, Physics and Astronomy,
McMaster University

NUMBER OF PAGES: xviii, 144

Abstract

Stars form in clustered environments embedded inside giant clouds of molecular gas across galaxies throughout the observable Universe. These clouds are turbulent entities that can go on to collapse into a collection of dense filamentary structures, along which, star formation is expected. Stars form along these filaments and coalesce into small sub-clusters that eventually merge with one another inside the cloud leading to the growth of a star cluster. In this thesis, we perform a suite of simulations that model the evolution of clusters as they grow inside their host cloud through accretion of the surrounding gas and mergers with other clusters. We model our systems as collections of stars and gas using the `AMUSE` framework and the `ASURA+BRIDGE` code. We first consider gas accretion onto the cluster in the form of a background gas distribution and dense filaments with velocities directed towards the cluster centre. Both of these processes cause a change to the cluster structure and filaments in particular efficiently provide the cluster with bound, star-forming gas. Movement through an ambient background environment causes the cluster to lose a fraction of its bound gas that is dependent on the velocity of the cluster, and the density of the medium. We then consider sub-cluster mergers inside a background gas environment whose distribution we inherit from previously run, larger scale star cluster formation simulations that were unable to adequately resolve individual stars. By resolving the individual stars in our simulations, we are able to track the dynamical evolution of the clusters as they merge. We find that mergers result in clusters that are anisotropically expanding and rotating. Both of these signatures are consistent with recent observations of gas-free star clusters. The clusters that merge remain gravitationally bound because of the high mass of background gas present ($\approx 10^4 - 10^5 \mathrm{M}_\odot$) which also lowers the amount of unbound stars produced from mergers to $< 3\%$. We show that gas is necessary in promoting the increase in cluster mass through mergers by simulating a merger without background gas. This simulation results in a non-monolithic cluster contrary to the simulation that does include background gas which results in a monolithic cluster after the merger. Lastly, we improve our simulation physics through the use of the `ASURA+BRIDGE` code which allows us to simulate stars and gas simultaneously while also including prescriptions for stellar feedback and the formation of new stars. We rerun a simulation from our previous work with this new framework to constrain the effects of stellar feedback and star formation and find that new star formation contributes to the mass growth of the cluster in two key ways: star formation from gas that is compressed by the merger process, and star formation from nearby filamentary gas that becomes accreted onto the merged cluster. Star formation

also enhances the anisotropic expansion and rotation inherited from the cluster merger such that they are still present after the cluster has removed its background gas through feedback and star formation. We find that dynamical signatures that the merger took place are still present after the cluster has removed most of its background gas and argue that these signatures will have an effect on the long term evolution of the cluster.

Co-Authorship

Chapters 2, 3, and 4 are original works that were written by myself. Chapter 2 is an article published in the Monthly Notices of the Royal Astronomical Society (MNRAS). The reference is *Karam, Jeremy, and Sills, Alison 2023, MNRAS, Volume 521, Issue 4, p.5557-5569.* My supervisor is the second author on this paper. Chapter 3 is an article published in the Astrophysical Journal (ApJ). The reference is *Karam, Jeremy, and Sills, Alison 2024, ApJ, Volume 967, Issue 2, article id. 86, 12 pp.* My supervisor is the second author on this paper. Chapter 4 is an article published in ApJ as well. The reference is *Karam, Jeremy, Fujii, Michiko S., and Sills, Alison 2025, ApJ, Volume 984, Issue 1, article id. 75, 10pp.* Dr. Michiko Fujii is the second author, and my supervisor is the third author. Dr. Fujii contributed to the development and editing of the article before submission. All published articles have been reformatted to be consistent with the McMaster University thesis guidelines. I hereby grant irrevocable, non-exclusive license to McMaster University and to Library and Archives Canada to reproduce the material as part of this thesis.

Acknowledgements

I will begin by thanking my supervisor, Dr. Sills for her non-stop support and guidance throughout this degree. Her patience is extremely appreciated as is her willingness to discuss any strange jumps I took in my research interests. I left every one-on-one meeting inspired to continue research and push my limits to learn new things. I will admit that McMaster was not my first choice for graduate school. However, now that I have come to the end of my time here, I cannot imagine myself carrying out my graduate studies in any other institution with any other supervisor. Without McMaster, and Dr. Sills in particular, I would not be the researcher I am today.

The Sills research group changed a lot during my time as a graduate student, but a constant has been Claude Cournoyer-Cloutier. She and I began at the same time in the same group, and we graduate at the same time in the same group. Claude's insight, expertise, and willingness to help with any problem has given me the confidence to continue pursuing astronomy beyond McMaster and will hopefully lead to further collaborations in the future. Beyond work, Claude has become a close friend that I have come to rely on.

Along with Claude are my office mates. Work breaks were made more fun with their conversations. I would also like to thank to my office mates in Japan. Going to Japan for a summer was a daunting experience but my friends Jenny and Chi-Hong made it a summer that I will remember fondly for my entire life.

I would also like to acknowledge and thank Corey Howard, Ralph Pudritz and William Harris for allowing me to use their simulation data for the work presented throughout this thesis. Their simulations provided the foundation necessary for me to build the results shown in this thesis. Their work is greatly appreciated.

Next on the list is my family. My parents were quick to drive 3 hours from their home in Whitby to my apartment in Hamilton just for a lunch together on the weekend. I would look forward to these lunches all week leading up to them. The company of my parents is unlike any other and I am glad that I was able to see them so often despite being so far away. Conversations with my sister during the most stressful times of my studies have been indispensable in the completion of this thesis. Whether it was during my job search, during thesis writing, or during a general bad day, I could count on the

advice and calmness of my sister to guide me through the struggle I was experiencing. I could also count on the frequent (though not frequent enough if we are being honest) sending of Heidi-photos from my family.

I would like to thank Veronika for her continued support throughout thesis writing and job searching. Without her, the completion of this thesis and chapter of my academic life would have been orders of magnitude more difficult.

I would also like to send a special thank you to the Westdale and Playhouse Theaters both in Hamilton. Since the beginning of my time at McMaster in 2019, both of these institutions have housed some of my fondest memories in Hamilton. Attending the film talks and seeing weekend matinees were mainstays in my everyday life in Hamilton and without these experiences, my ability to focus on the work that went into this thesis would have been severely diminished.

Lastly, I would like to thank Bo. The technology necessary for him to read this thesis is not yet completely developed, but I hear that a cat-to-English translator should be available by 2028.

"When do I begin to learn anything at all about anything?"

-Lije Baley, The Naked Sun by Isaac Asimov (1956)

Contents

List of Figures

List of Tables

Chapter 1

Introduction

Looking up at the great bull Taurus constellation in the night sky, one can pick out a group of six stars quite tightly packed together known as the Pleiades star cluster. While it may seem like this is a small collection of only a handful of stars, the membership count of Pleiades increases the deeper you look. In 1609, Galileo Galilei published *Sidereus Nuncius* where he cataloged observations of stars in the Milky Way seen through his telescope. The Pleiades was on his list. Galileo updated the number of stars in the cluster to thirty-five. Modern day observations of the Pleiades star cluster put the membership count up to $\approx$ 1000 stars (e.g. Alfonso and García-Varela 2023) and the age at $\approx 10^8$ years (e.g. Gaia Collaboration et al. 2018). This places the Pleiades star cluster in the open cluster category.

Observations of star clusters find that they are common throughout the observable Universe and that they can range in ages from a few millions of years old (open clusters and young massive clusters), up to the age of the Universe itself (globular clusters). They can also range in mass from $\approx 10^2$ - 10^6 $M_\odot$ (e.g. Krumholz et al. 2019). Open clusters tend to be less massive and more diffuse while globular clusters and young massive clusters lie on the high mass end of clusters and can have very high densities ($\gtrapprox 10^3$ $M_\odot pc^{-3}$) (Portegies Zwart et al. 2010). Star clusters are also thought to play a very important role in the reionization of the Universe early after its formation (e.g. Ricotti 2002, Griffen et al. 2010, Vanzella et al. 2020). Thanks to groundbreaking observations from the James Webb Space Telescope (*JWST*), the connection between the populations is becoming more apparent.

JWST observations of lensed high redshift galaxies from Adamo et al. (2024) suggest proto-globular cluster formation $\approx$ 500 Myr after the Big Bang. The sizes of these observed proto-globular clusters are similar to those found for young massive clusters in starburst galaxies in the local Universe implying that the young massive clusters we see

today may go on to become globular clusters after billions of years of evolution (Portegies Zwart et al. 2010). However, the formation process of an open cluster or a young massive cluster is still under debate. So too is the exact process by which a young massive cluster can evolve into a globular cluster. The ubiquity of star clusters throughout the Universe, and their importance in shaping the evolution of the Universe points towards a need to understand the formation of star clusters and their evolution throughout cosmic time.

Beginning with cluster formation, a common opening line for papers in the literature is some variation of: "All stars form in clusters (Lada and Lada 2003)", but this leaves out a lot of detail. The same work further hints at the origin of clusters by showing that stars form in clustered environments embedded within giant clouds of molecular gas throughout galaxies. Observations of giant molecular clouds find that they are turbulent structures within galaxies whose density distributions can be very complex. Particularly dense (with number densities $\gtrapprox 10^3$ cm^{-3}) and cool (with temperatures on the order of 10K) regions of molecular clouds are associated with protostars implying that star formation does not take place everywhere within a given giant molecular cloud. Far infrared observations of the interstellar medium taken by the *Herschel* space telescope have found that the interstellar medium contains many filaments of high density gas (e.g. André et al. 2010) and that star formation is preferentially located along these filaments (e.g. Könyves et al. 2015). Filaments can intersect with each other in hub-filament systems which are regions of expected star cluster and massive star formation (e.g. Dewangan et al. 2024). Stellar feedback in the forms of protostellar outflows, winds, radiation pressure, photoionization, and supernovae all contribute to the eventual removal of surrounding molecular gas thus leading to a gas-free star cluster that is easier to observe in optical wavelengths (Krumholz et al. 2019). Because of the extinction from dust belonging to the giant molecular cloud, we must turn to numerical simulations to learn about the exact processes that dictate cluster growth in their earliest stages.

Numerical simulations of star cluster formation inside giant molecular clouds show that star cluster formation is a hierarchical process. Regions of a giant molecular cloud collapse and form small collections of stars (sub-clusters) that will eventually accrete surrounding gas to form more stars, and also merge with each other (e.g. Fujii et al. 2012, Howard et al. 2018, Cournoyer-Cloutier et al. 2021). Gas accretion from surrounding filaments and cluster mergers lead to an increase in size and mass of a star cluster throughout its embedded phase.

There are still billions of years of evolution between clusters that have recently removed their background gas and the old globular clusters that we see in the Milky Way

and beyond. In this time, a large range of dynamical processes can take place to influence the evolution and survivability of a cluster. As a cluster evolves in its host galaxy, it can evaporate due to dynamical friction, shocks from the galactic disk or bulge, and two body relaxation effects (Gnedin and Ostriker 1997). The dynamical conditions with which a star cluster exits its embedded phase can have a direct effect on its long term evolution. For example, clusters with anisotropy in their radial and tangential velocity distributions can evolve quicker towards collapse of their core (Pavlík and Vesperini 2021) which will cause them to rotate (Vesperini et al. 2014), and lose their outermost stars quicker (Livernois et al. 2022). An open question in the field is therefore: what are the dynamical signatures of clusters that have recently removed their surrounding gas? How, if at all, do these signatures depend on the gas distribution?

Answers to the above questions require simulations that can resolve individual stars during hierarchical star cluster assembly. Simulations that look to model the formation of young massive clusters (e.g. Howard et al. 2018, Fukushima and Yajima 2021, Ali et al. 2023) cannot resolve down to the formation of individual stars meaning they cannot accurately resolve the dynamics of the cluster that forms. By resolving the individual stars in hierarchical assembly simulations (and allowing for the formation of new stars from dense gas as well as stellar feedback prescriptions), we can learn what dynamical signatures are left on a star cluster after it merges with other star clusters and interacts with its surrounding gas environment.

In this thesis, I present simulations that answer some of the key questions regarding the dynamics of star cluster formation and whether or not dynamical signatures discussed above can last until a cluster has emerged from its embedded phase. I also discuss how these dynamical signatures depend on the gas distribution that is present during early star cluster formation and evolution. The remainder of this chapter will be dedicated to a summary of the current state of the field of star cluster formation and evolution.

Section 1.1 focuses on the results from observations that show the necessary conditions for star formation and star cluster buildup inside giant molecular clouds. There is a focus on the gas morphologies found to be associated with star formation.

Section 1.2 concerns the current observations of cluster dynamics. There is a focus on the gas-free cluster observations.

Section 1.3 focuses on a history up to the current state of star cluster formation simulations. The discussion includes improvements made in recent years regarding the handling of gas in these simulations.

Section 1.4 concerns the simulation techniques we use for our studies of star cluster formation with an emphasis on the improvements of our numerical methods compared to previous works.

1.1 From Giant Molecular Clouds to Star Clusters

The clouds of molecular hydrogen within which star formation and star cluster buildup take place are not simple isolated structures in a galaxy. Studies of dust and ^{12}CO(1-0) emission show that these clouds are enveloped by diffuse atomic gas and are highly filamentary (Chevance et al. 2023).

Filamentary structures are ubiquitous across observations of star forming regions. there is even evidence that they may be common regardless of metallicity, though their parameters may change (Tokuda et al. 2025). The nearest example of a filamentary star forming cloud is found in the Orion constellation and seen in figure 1.1. Filaments are often classified as objects with an aspect ratio $A > 3$ where:

$$A = \frac{L}{2R} \tag{1.1}$$

Here, L is the length of the filament, and R is its radius (Hacar et al. 2025). The distribution of gas within the cloud is emblematic of a long cylinder with particularly dense regions along the spines. It is along these spines that we see protostars. These are the earliest stages of star formation and can often be segmented into different classes. Class 0 protostars are the earliest stages of protostar ($\lessapprox 10^4$yr) (Andre et al. 1993), while Class I and Class II protostars represent later states of evolution towards fusion in the stellar core (Lada 1987).

Early theoretical studies of isolated filamentary distributions of gas showed that they experience equilibrium between self gravity and pressure if their line mass ($M_{line} \equiv M/L$ where M is the mass of the filament and L is its length) is close to a critical value given by:

$$M_{line,crit} = \frac{2\sigma^2}{G} \tag{1.2}$$

where σ is the velocity dispersion the filament gas, and G is the gravitational constant (Ostriker 1964, Inutsuka and Miyama 1992). This can be related to the sound speed (c_s) of the gas using

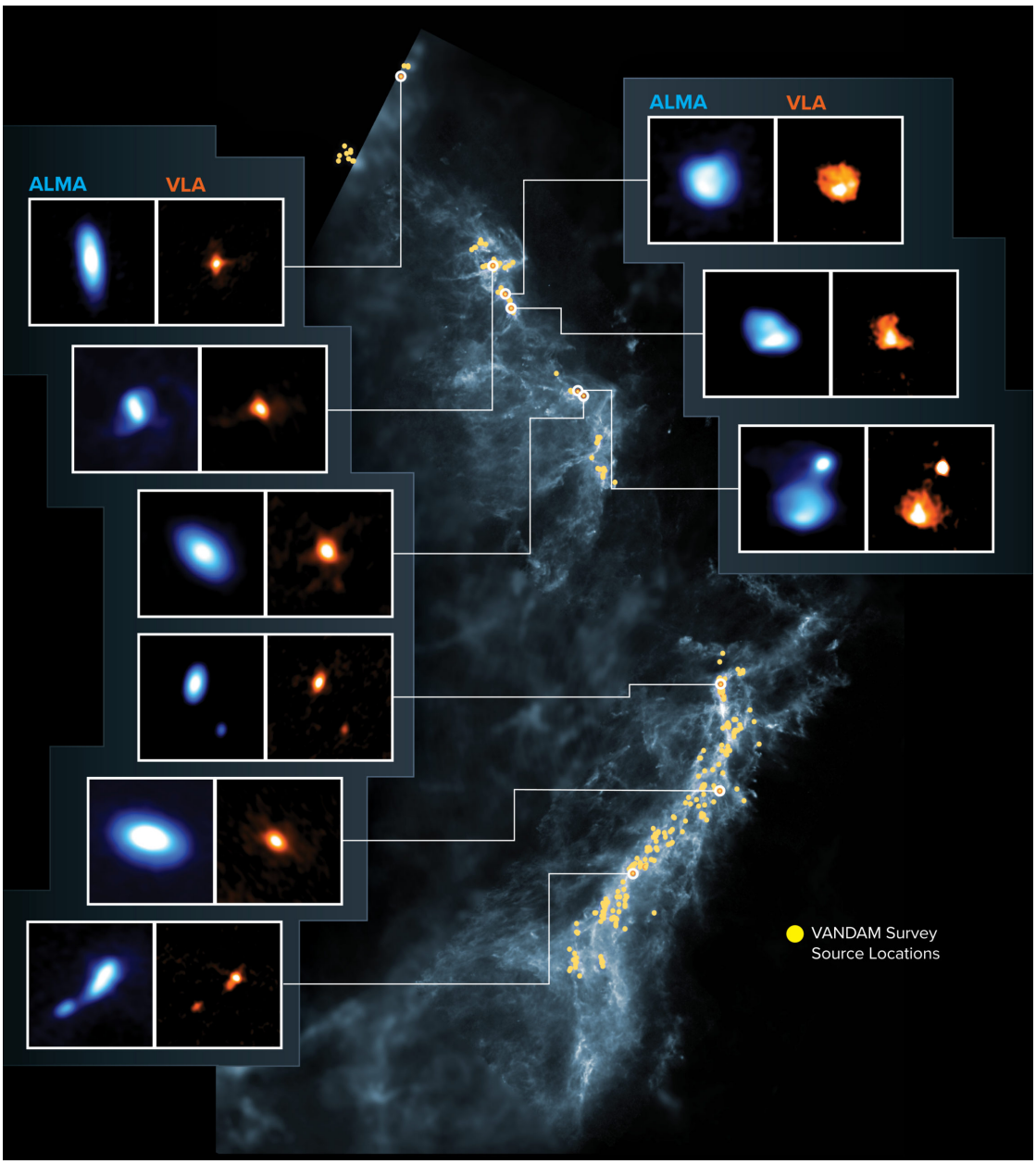

FIGURE 1.1: The molecular clouds in the Orion constellation taken as part of the VANDAM survey. The blue background is the gas distribution of the clouds while the yellow dots are the protostars. Zoom-ins of protostars show data from the Atacama Large Millimeter Array (left, blue) and the Karl G. Jansky Very Large Array (right, orange). *Credit: ALMA (ESO/NAOJ/NRAO), J. Tobin; NRAO/AUI/NSF, S. Dagnello; Herschel/ESA.*

$$\sigma = c_s \left(1 + \frac{L}{0.5pc}\right)^{0.5} \tag{1.3}$$

where L is the filament length (Hacar et al. 2025).

An isolated cylindrical distribution of gas whose $M_{line} < M_{line,crit}$ will disperse without reaching densities high enough to form stars because the internal pressure of the gas will overpower its self gravity. Conversely, a cylindrical distribution of gas with $M_{line} > M_{line,crit}$ will collapse under its own gravity leading it to fragment into spherical cores that are evenly spaced along the filament (Nagasawa 1987, Inutsuka and Miyama 1997).

It is within these spherical cores that stars are expected to form. It is important to note that one single core will not necessarily go on to form one single star with a mass equal to that of the core. There has been considerable effort in the observation literature to establish a connection between the core mass function (CMF) and the stellar initial mass function (IMF) with varying results depending on the region considered and the spatial resolution of the observation (e.g. Könyves et al. 2015, Motte et al. 2018, Kong 2019, Pouteau et al. 2022). While the CMF can look similar to commonly accepted IMFs (i.e. Chabrier 2003), there are regions where the CMF contains higher mass cores than the high mass stars present in the IMF which would result in a mass conversion factor of core mass to stellar mass that is less than unity.

Not all filamentary clouds are exactly the same. For example, while the Orion clouds have only a single main filament along which star formation is expected, radio and infrared observations have found the existence of hub-filament systems (e.g. Fukui et al. 2019, Wong et al. 2022, Kumar et al. 2022, Seshadri et al. 2024, Zhang et al. 2024). These are gas clouds with multiple, often overlapping filaments and are thought to be the formation sites of massive stars (Dewangan et al. 2024). As these filaments are present throughout star forming molecular clouds, it is important to understand the behavior of filamentary gas distributions if we are to understand the exact mechanisms by which star formation occurs.

The *Herschel* space telescope has provided the astronomical community with ample data of filamentary molecular clouds and has shed light on some of the fundamental parameters governing filament evolution. In particular, the *Herschel* Gould Belt Survey (HGBS) (André et al. 2010), which focuses on the ring of molecular clouds inclined to the Milky Way Plane known as the Gould Belt provides a catalog of nearby star forming regions to study allowing for high resolution observations. The study of the clouds in this region by Arzoumanian et al. (2011) and Arzoumanian et al. (2019) have shown that

filaments make up roughly 80% of the mass of molecular clouds, have a characteristic width of ≈0.1 pc, and can have a range of masses, and lengths. Though filaments tend to exist in the high column density regime of molecular clouds ($> 7\times10^{21}$ cm^{-2}), they can have a range of central column densities and have density profiles consistent with Plummer (Plummer 1911) profiles along their short axis.

The range of masses and lengths of filaments implies a range of possible line masses and, in turn, a range of possible equilibrium configurations meaning that not all filaments will fragment and form dense cores and stars. A study of the Aquila star forming region in the HGBS by André et al. (2010) finds that core formation prefers supercritical filaments (see figure 1.2). From this figure, we see that most (>60%) of the bound prestellar cores (blue triangles) are found within filamentary structures whose line mass exceed the critical line mass. Furthermore, all supercritical filaments host prestellar cores or protostars (green stars). This is further supported by an in depth study of the dense cores performed by Könyves et al. (2015) which places the fraction of dense cores within supercritical filaments at $75\%^{+15\%}_{-5\%}$ within the Aquila region. But, how do we know that cores along these filament systems will coalesce and go on to form clusters of stars? For this question, we can look at the dynamics of the star forming gas within these molecular clouds.

Monoceros R2 (Mon R2) is a massive star forming region located only 830 pc away from Earth (Racine 1968). This, along with its morphology of interconnected supercritical filaments makes it an excellent candidate for the study of star formation and star cluster buildup. Pictured in figure 1.3 the Mon R2 region consists of many connected filaments attached to a central hub. Treviño-Morales et al. (2019) show that the main filaments (filaments whose names begin with 'F' in figure 1.3) converge to the central hub and fragment along their long axes because of their high line mass implying new star formation in the region. Conversely, secondary filaments (those filaments whose names begin with 's' in figure 1.3) only fragment sporadically and converge onto the main filaments. Furthermore, an analysis of the distribution of young stellar objects (YSOs) in the region shows a clustering of YSOs in the gas distributions dense with filaments unlike the YSO distribution in the sparser gas regions which are more diffuse (Megeath et al. 2022). Considering velocity gradients along the main filaments of Mon R2 (Rayner et al. 2017, Treviño-Morales et al. 2019) a model is proposed which suggests that secondary filaments feed gas onto main filaments which in turn feed gas to the central hub where the gravitational potential is highest in the region. Since this gas is dense and star forming (and star forming cores are detected along these filaments, see Keown

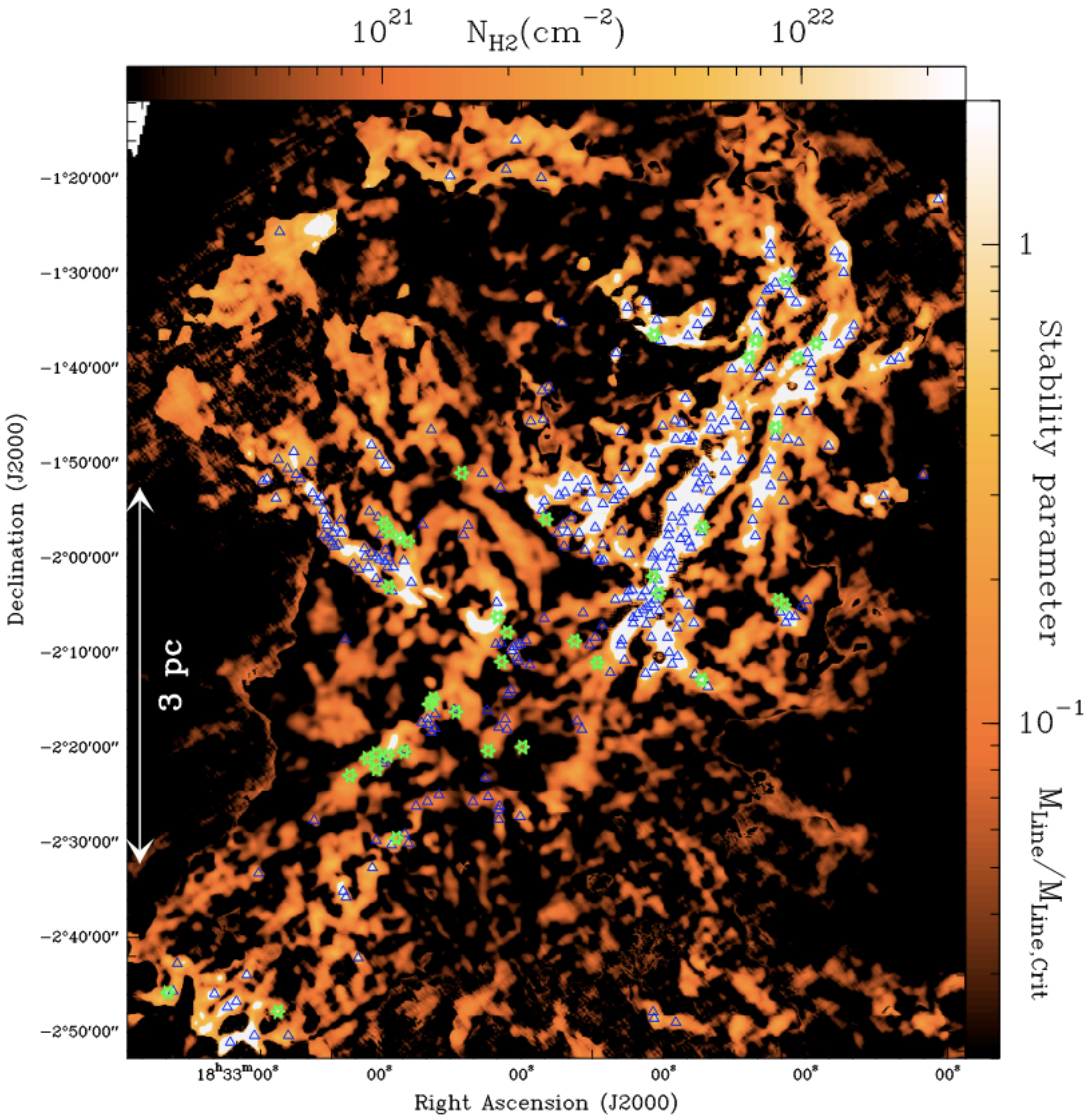

FIGURE 1.2: *Herschel* column density map of the Aquila star forming region. Brighter colours correspond to both higher column densities, and higher $M_{line}/M_{line,crit}$ (those regions which are likely gravitationally unstable are shown in white). Green stars show candidate class 0 protostars and blue triangles show bound prestellar cores in the region. *Credit: André et al., A&A, 518, L102, 2010, reproduced with permission ©ESO.*

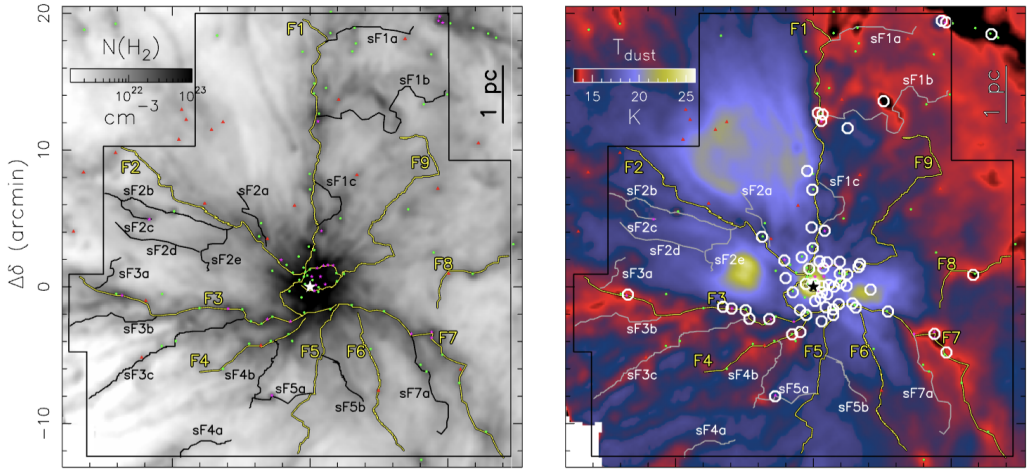

FIGURE 1.3: Left: Column density map of the molecular hydrogen in the Mon R2 region. Right: Temperature of the dust in the Mon R2 region. Yellow and black lines show main and sub filament skeletons. The blue points show protostars, green points show bound gas cores, and red points shown unbound gas clumps (Rayner et al. 2017). The white circles show cores from Sokol et al. (2019). *Credit: Treviño-Morales et al., A&A, 629, A81, 2019, reproduced with permission ©ESO.*

et al. 2019) it is expected that the system will coalesce into a cluster of stars. Mon R2 currently has a stellar component as well. *Gaia* space telescope data from the second data release analyzed by Kuhn et al. (2019) suggest that the stellar component of Mon R2 is contracting, likely due to the large potential from the surrounding hub (Kumar et al. 2022). More recent third data release *Gaia* data from Jiang and Hillenbrand (2024) show that the stars in Mon R2 are subclustered in both position and velocity space (we discuss cluster substructure more in Section 1.2).

Kirk et al. (2013) showed evidence of accretion flows along the Serpens South filament which are bringing gas onto a forming star cluster (protocluster) in the centre of the region. The authors used this system to calculate the rate of gas accretion along the Serpens South filament ($\dot{M}_{||}$) using:

$$\dot{M}_{||} = v_{||}\frac{M}{L} \tag{1.4}$$

where $v_{||}$ is the velocity of material along the filament, M is the mass of the filament, and L is its length. This can also be written in terms of the velocity gradient along the filament ($\nabla v_{||} = v_{||}/L$). Accretion along the Serpens South filament onto the central cluster takes place at a rate of ≈ 28 $M_{\odot}Myr^{-1}$ (Kirk et al. 2013).

This process is present within hub-filament systems as well as shown by the observed collapse along the filaments towards a common centre in the SDC13 infrared dark cloud (Peretto et al. 2014, see figure 1.4). The authors find that each filament in the hub-filament system is collapsing to a common centre and determine that the smooth gradient observed along the filaments towards that centre is the result of gravity (as opposed to a different mechanism such as filament motions driven by nearby stellar winds). Furthermore, the two most massive cores in the SDC13 system are located at the centre of the system implying that the flows along the filaments driven by gravity are feeding gas onto the potentially star forming cores (which may go on to result in star cluster formation because cores are present along the filaments as well). Not all cores that are fed gas from filaments will go on to form stars due to the increase in velocity dispersion imparted on the cores from filament accretion which can prevent collapse by increasing turbulence. It is important to note that SDC13 is only $\approx 600M_{\odot}$ meaning that, if a star cluster forms in this system, it will be low mass (this is also evidenced by the fact that only 18 dense cores were observed in the system). An example of a much more massive complex hub-filament system is the 30 Doradus HII region surrounding the young massive cluster R136 (Wong et al. 2022). The accretion rates inside hub-filament

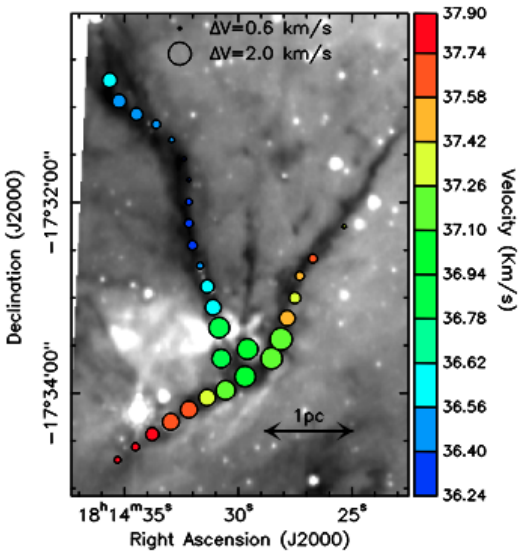

FIGURE 1.4: Greyscale shows gas density of the SDC 13 region with darker regions showing denser gas. Coloured circles show velocity of a given region with the size of the circle representing the velocity dispersion. *Credit: Peretto et al., A&A, 561, A83, 2014, reproduced with permission ©ESO.*

systems are $\dot{M} \approx 20-4500$ $M_{\odot}Myr^{-1}$ with a mean value of ≈ 1000 $M_{\odot}Myr^{-1}$. They are also positively correlated with the mass of the hub-filament system (Hacar et al. 2025).

From this discussion, we see the interconnectedness between gas phase space morphology and star cluster formation. Allowing star forming hub-filament systems to collapse under their own gravity may lead to the formation of a star cluster because of the high number of star forming cores distributed along the many filaments. These star clusters can vary in mass depending on the gas distribution from which they formed. However, there is a problem when it comes to observing the cluster formation process. The fact that these star clusters form embedded deep inside dense molecular gas means that observations are unable to pierce through the cloud and see the clusters as they assemble because of the high extinction of stellar light. A key question therefore arises when considering star cluster formation: can we use observations of the star clusters that we can see in the Milky Way (i.e. those that are devoid of their natal gas) to constrain the formation histories of star clusters?

1.2 Cluster Dynamics

1.2.1 Expansion

A key dynamical signature that affects cluster evolution is cluster expansion. Understanding the expansion of star clusters allows us to better understand the formation mechanisms of these clusters as we can trace back the stars to determine what physical processes caused the expansion signatures we observe. It is also vital in predicting the long term evolution of a cluster because as gas-free clusters expand, the velocities of the expanding stars coupled with the change in potential of the system implies that such expanding systems can lose mass as time goes on.

Expansion of young star clusters is expected as a cluster removes its surrounding gas through stellar feedback which causes a decrease in the overall potential of the system. The stellar component that remains reacts to the change in potential by expanding. Previous studies of cluster expansion focused on indirect observations through a comparison of cluster sizes with cluster age where a trend is present showing an increase in cluster size with cluster age for massive Milky Way clusters (Pfalzner 2009) and extragalactic clusters (Portegies Zwart et al. 2010). This trend has been interpreted as a sign of cluster expansion (clusters grow in size as they expand and age) and is present in both compact and diffuse clusters (Pfalzner 2009, Pfalzner and Kaczmarek 2013). Results from Pfalzner and Kaczmarek (2013) suggest that diffuse clusters are the ones which are more affected by gas expulsion while expansion present in more compact clusters comes from the internal dynamics of very dense systems.

Bastian and Goodwin (2006) indirectly detect cluster expansion by comparing density profiles of young clusters to those expected of relaxed systems. Evidence for expansion comes from the excess cluster light they find in the outer regions of the cluster which is expected of an expanding cluster. The authors show that as a cluster loses its background gas, it becomes supervirial. This is defined as a state where $\alpha > 1$ where α is the virial parameter defined as

$$\alpha = \frac{2K}{|U|} \tag{1.5}$$

where K is the total kinetic energy of the cluster, and U is the potential energy of the cluster. The end product of a supervirial cluster could be a complete dissolution of the cluster in tens of Myr after it removes its surrounding gas. However, recent observations of cluster expansion in gas-rich clusters show that they can be expanding while still being bound (i.e. $\alpha < 1$) because the expansion is induced through dynamical

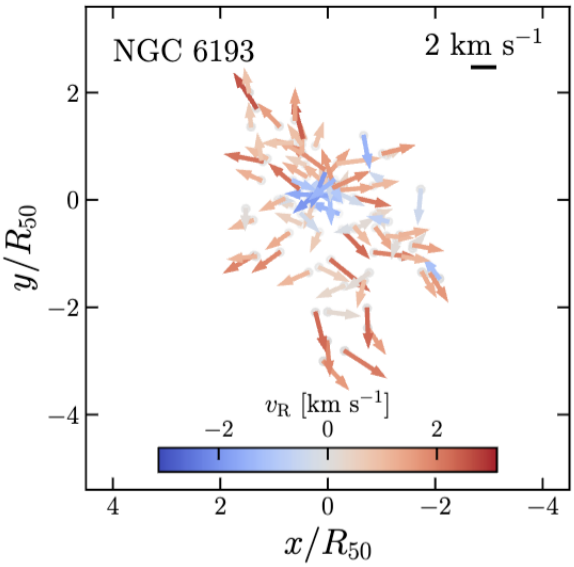

FIGURE 1.5: Kinematic properties of NGC 6193. Arrows show direction of velocity vectors of the stars with their length showing the speed of the star on the plane of the sky, and their colours showing the magnitude of the radial component of their velocities. *Credit: Della Croce et al., 683, A10, 2024.*

interactions (Kounkel et al. 2022).

The *Gaia* space telescope has been vital in forwarding our understanding of star cluster dynamics by providing proper motions of over a billion stars in the Milky Way thus opening a new avenue for direct detection of cluster expansion. Kuhn et al. (2019) performed a study of 28 clusters with ages between 1 Myr and 5 Myr that were in various stages of gas expulsion using *Gaia* data. Through calculating the outwards (radial) velocity vector of member stars, the authors found direct evidence of expansion in the majority of clusters studied. When this process was extended to include a few thousands of Milky Way clusters (from catalogs compiled in Cantat-Gaudin and Anders 2020, and Cantat-Gaudin et al. 2020), Della Croce et al. (2024) find that the expansion rates of clusters decrease with age implying that stars that are expanding away from the cluster centre are potentially becoming unbound thus lowering the overall expansion velocity of the remaining cluster. Now that we see evidence for cluster expansion, how can we use these expansion signatures to tell us about the formation process of star clusters?

If the gas distribution within which a cluster is initially born is uniform, there is no preferred direction of stellar feedback, and the cluster is spherical, then the cluster should expand uniformly in every direction. This, however, is not the case when looking at observations of young cluster expansion signatures. A qualitative example can be seen in figure 1.5 which shows the distributions of stars belonging to the young cluster NGC 6193. Arrows represent the velocity of each star (Della Croce et al. 2024). As can be seen by the orientations of the velocity vectors, the expansion of the cluster is non-spherical. There is a preferred direction of expansion along the y-axis.

Evidence for anisotropic expansion also comes from observations of the young (1-2 Myr old) cluster NGC 6530 analyzed by Wright et al. (2019). They looked at the distribution of stars in position and velocity space along a given axis (for example, in cartesian coordinates this would be the position of a star along the x-axis against its velocity along the x-axis). Velocity gradients along a given axis imply expansion (or contraction if the slope is negative). Stars farther away from the cluster centre have higher velocities implying the overall expansion of the cluster. The authors analyzed the expansion signatures present along the right ascension and declination axes separately and found expansion rates of 0.00 ± 0.06 $\mathrm{kms^{-1}pc^{-1}}$ and 0.74 ± 0.06 $\mathrm{kms^{-1}pc^{-1}}$ respectively implying a preferred expansion along the declination axis of the cluster. Larger surveys of young clusters (Wright et al. 2024) find similar anisotropic expansion signatures for clusters over a range of ages (from 1 to 19 Myr old). These results hint at the requirement for a non-spherical mode of star cluster formation.

1.2.2 Rotation

Bulk cluster rotation has recently become a dynamical signature of interest because of its presence in the oldest globular clusters. Originally, globular clusters were thought to be non-rotating systems because relaxation effects over long timescales would smooth out any dynamical complexity. Recently, however, it has been shown that long term evolution of clusters with initial rotation are able to maintain rotational signatures (Tiongco et al. 2017) implying the existence of rotating globular clusters. And indeed, rotating globular clusters have been observed in recent years (e.g. Leanza et al. 2022, Leanza et al. 2024). The question is therefore the following: do observations of young clusters show signs of cluster rotation or do globular clusters gain their rotation through another source?

Rosolowsky et al. (2003) studied potentially star cluster forming molecular clouds in the galaxy M33 and found signatures of angular momentum in these clouds. Indeed, it

is possible for such rotating clouds to impart their angular momentum on star clusters should the cloud meet the conditions to form a star cluster (e.g. Wright et al. 2016). While radial velocity was used to study expansion or contraction of a cluster's stellar component, tangential velocities inherited from *Gaia* data have proven useful for studying cluster rotation. Kamann et al. (2019) studied the 3D rotation present in NGC 6791 and NGC 6819 (aged 8 Gyr and 2.4 Gyr respectively) and found signs of rotation in NGC 6791. One cluster studied in the Wright et al. (2024) sample mentioned in the previous subsection, λ Ori, is studied in further detail in Armstrong and Tan (2024). Along with anisotropic expansion signatures, Armstrong and Tan (2024) also find signatures of rotation in the young cluster λ Ori (aged 4-6 Myr). Kounkel et al. (2022) did a deconstruction of the stars in the Orion Nebula Cluster by looking for rotational trends with age and find that the youngest stars have the highest rates of rotation around the cluster centre of mass. Comparing with the rotation present in the gas within the Orion Nebula Cluster (Theissen et al. 2022), the authors conclude that this is a by-product of the stellar motions which are inherited from gas motions.

It is also useful to determine where the rotation is located within a cluster. As a result, rotation profiles as a function of radial distance away from the cluster centre have been constructed for young massive clusters and open clusters (e.g. Hénault-Brunet et al. 2012, Hao et al. 2024) as well as for older globular star clusters (e.g. Mackey et al. 2013). Regardless of age, there is a trend that shows higher rotation signatures in the cluster centre and lower rotation signatures in the cluster outskirts for many star clusters. This rotation profile is expected for clusters that are not yet relaxed. Furthermore, measurements of tangential velocities of young clusters (e.g. Wright et al. 2016) show that not all stars rotate in the same directions around their cluster centre implying a complex star cluster formation scenario. Because rotation is present in young clusters, it is expected that they gained their rotation from their formation history.

1.2.3 Substructure in Associations

Further dynamical complexities are found when looking at larger OB associations (named such because of their propensity to contain high mass O and B stars). OB Associations are large ($\gtrapprox$100 pc) collections of stars that are gravitationally unbound from one another giving them low spatial densities ($<0.1 M_\odot$ pc^{-3}). An association that has been studied for many years is Sco-Cen (seen in figure 1.6) which is the nearest OB Association to Earth making it also the nearest location of massive star formation. When considering the brightest stars belonging to Sco-Cen in position space, Blaauw (1946) first subdivided the collection of stars into three subgroups. Wright and Mamajek (2018) used *Gaia*

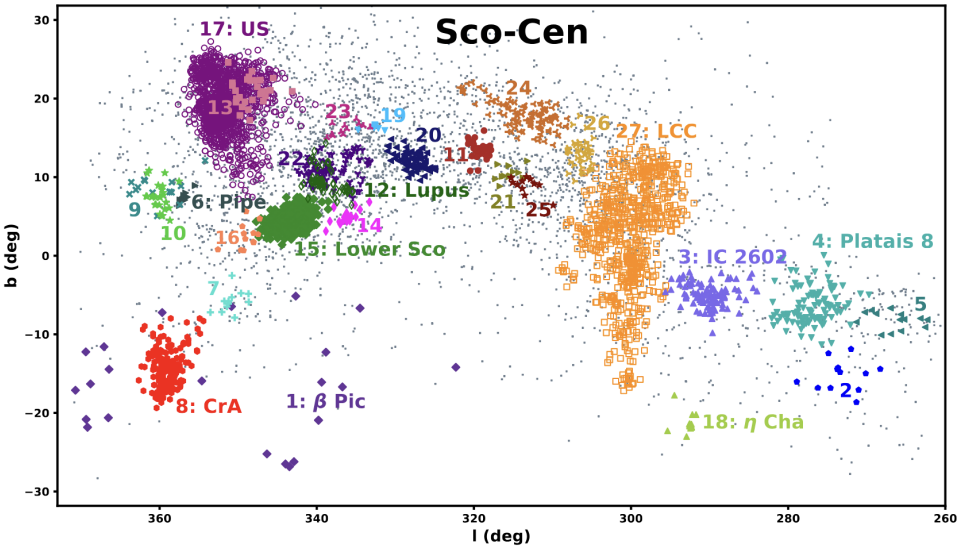

FIGURE 1.6: The distribution of stars in the Sco-Cen OB association as shown in Kerr et al. (2021). Each colour corresponds to a different subgroup in Sco-Cen, and gray points show stars that do not belong to any subgroup. *©AAS. Reproduced with permission. doi: 10.3847/1538-4357/ac0251*

DR1 data to determine the presence of kinematic substructure in each of these three subgroups. With *Gaia* DR2 data and the ability to observe lower mass stars, Kerr et al. (2021) subdivided the Sco-Cen region into 27 subclusters. Coupling this with age data for the stellar members, the authors find that the Sco-Cen region contains stars with a range of ages from ≈2 - 23 Myr (similar age gradients are also observed in the more dense young massive cluster R136, see Fahrion and De Marchi 2024). Therefore, we can say that Sco-Cen is substructured not only in position space, but in kinematic and age spaces as well. Other OB associations show signs of substructure. For example, the Cassiopeia OB association shows signs of subclustering in position space with some subclusters showing expansion signatures (Lim et al. 2023). Furthermore, more compact star clusters show signs of spatial and kinematic substructure (i.e. Mon R2, see Jiang and Hillenbrand 2024).

Substructure points towards a fractal star formation model wherein star formation takes place in clumps distributed throughout a molecular cloud likely originating from the filamentary nature of the cloud which promotes dense core formation (see Section 1.1). Dynamical interactions between the clumps, coupled with the removal of natal

gas through feedback can cause the entire system to expand thus providing an explanation for the substructure observed in these associations. As the clumps travel along their host filaments, they may merge with eachother. These mergers take place from different directions throughout the evolution of the cluster inside the GMC. Therefore, hierarchical star cluster assembly may be an explanation for the non-spherical dynamical characteristics observed in gas-free clusters.

1.3 Star Cluster Formation and Evolution Simulations

Observations of star cluster dynamics from *Gaia* are of clusters that are mostly devoid of gas because of the high extinction of deeply embedded clusters. Determining cluster formation histories from observations of cluster dynamics involves extrapolating backwards in time from the current state of the cluster. This is by no means the only method for understanding star cluster formation histories.

Early numerical simulations of star cluster evolution inside their natal molecular clouds did not include a direct prescription for gas. Many simulations (e.g. Geyer and Burkert 2001, Boily and Kroupa 2003, Baumgardt and Kroupa 2007) used purely N-body techniques to study the dynamical response of a star cluster to the removal of its surrounding gas. In these simulations, gas was modeled as a changing external potential (represented by an analytical function) to which the stars would react. This was often used to mimic gas expulsion and study the resultant star cluster expansion. The general trend was that, as the potential from the gas changes, the star cluster expands and loses a fraction of its bound mass. This fraction is dependent on the star formation efficiency defined as

$$\epsilon_{SFE} = \frac{M_{st}}{M_{st} + M_{gas}} \tag{1.6}$$

where M_{st} is the stellar mass, and M_{gas} is the gas mass. Clusters that formed from clouds with higher star formation efficiency tend to lose less stellar mass from expansion because there was less gas mass to remove. This means that the removal of said gas mass results in less of a decrease in the overall potential compared to systems with high initial gas mass. Geyer and Burkert (2001) did also consider implementing hydrodynamics to represent the gas component of their clusters, but did not account for realistic gas expulsion mechanisms (i.e. stellar feedback).

As simulation codes became more advanced so too did our ability to model the evolution of embedded star clusters realistically. Pelupessy and Portegies Zwart (2012) advanced the field by modeling star clusters with the inclusion of a stellar component

using N-body techniques, a gas component using computational hydrodynamics solvers, and stellar feedback for more realistic gas expulsion. Through these detailed simulations, the authors were able to provide a requirement that $\epsilon_{SFE} > 0.05$ for cluster survival after gas expulsion. They were also able to constrain the timescale for gas expulsion and find that clusters become gas-free in $\approx 5-10$ Myr after they form depending on the strength of the feedback chosen. A caveat to the above simulations is the initial conditions of the stars and gas which which were chosen to be idealized Plummer (Plummer 1911) spheres. This is not an accurate representation of the phase space distribution of young star clusters (as discussed in Section 1.2).

To better determine the structure of star clusters during their embedded phase, simulators have begun their simulations from the molecular cloud within which the star cluster forms. These simulations account for the formation of new stars, and eventually star clusters, allowing for a self consistent view of star cluster formation. This allows simulators to study the formation of the star cluster while accounting for the environment and, depending on computational resources, the physics of stellar feedback. A standard simulation of this kind begins with molecular gas distributed spherically. Turbulence is then induced in the cloud as observations of giant molecular clouds (e.g. Heyer and Brunt 2004) find that they are turbulent entities. This promotes a non-uniform density distribution where regions of the cloud can have higher densities than others. As well, filaments form as the cloud evolves. One example of this can be seen in figure 1.7 which shows a giant molecular cloud that has evolved up to ≈3 Myr (Li et al. 2019). The top right snapshot shows regions of high density (yellow) which have gone to form stars (white points) before the low density regions of the cloud. This is because bound high density gas collapses before bound low density gas thanks to its low free-fall time defined as:

$$t_{ff} = \sqrt{\frac{3\pi}{32G\rho}} \tag{1.7}$$

where ρ is the density of the region of interest. Higher density gas will collapse quicker than its low density counter part implying non-uniform star formation distributed across turbulent molecular clouds. As the cloud evolves in the Li et al. (2019) simulation, the clumps of stars that form in the densest regions of the cloud eventually merge with each other and form more massive clumps and eventually, clusters. By the end of the simulation, feedback from stars has removed the surrounding gas.

Mergers of clumps of stars inside clouds tells us that clusters grow hierarchically before they remove their surrounding gas through stellar feedback affects. The strength

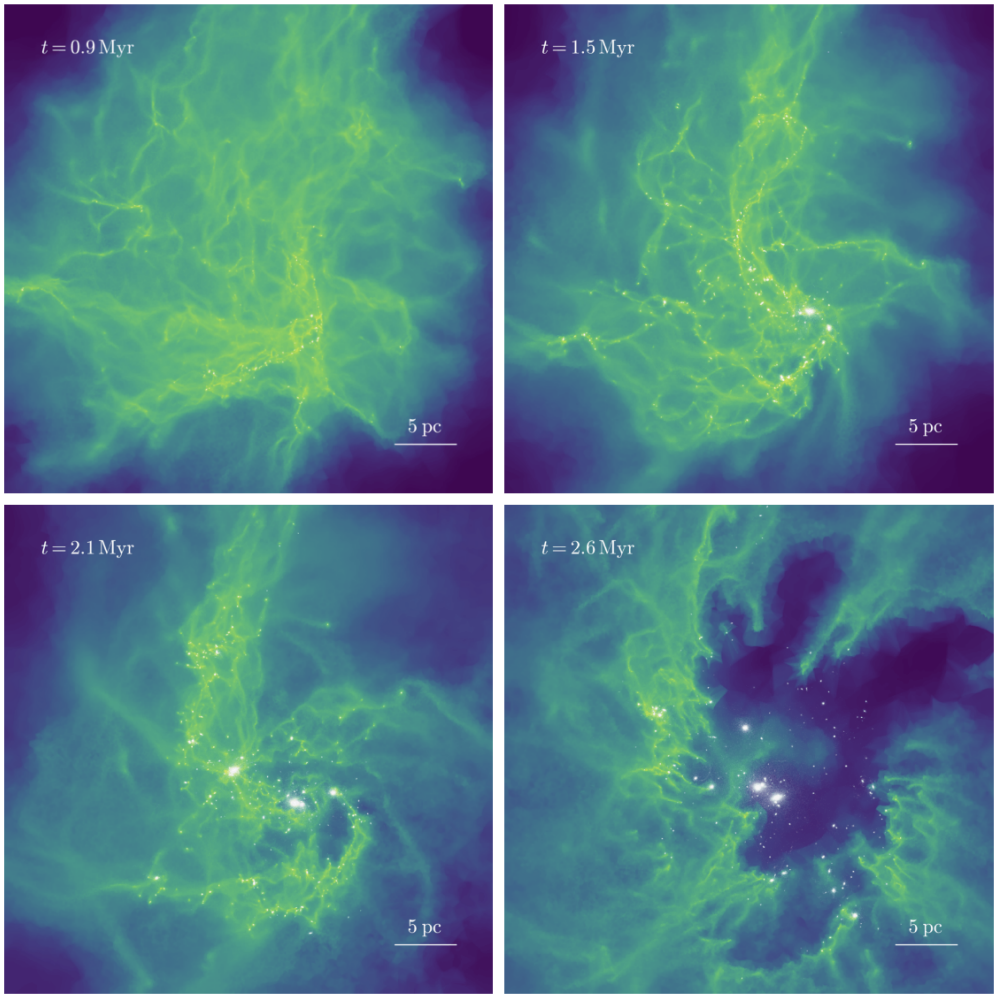

FIGURE 1.7: Evolution of a giant molecular cloud. The colour range shows the gas surface density with a range of $50 M_{\odot} pc^{-2}$ up to $10^{6} M_{\odot} pc^{-2}$. The white dots show star particles. (Figure 1 from Li et al. 2019).

of clump mergers as a cluster growth mechanism was studied explicitly in Howard et al. (2018) where the authors performed star cluster formation simulations from turbulent giant molecular clouds. They quantified the amount of mass inherited by the final star cluster from mergers and found this fraction to be $\approx 50\%$ for the most massive star clusters meaning that young massive clusters (and globular clusters) gain a significant fraction of their mass through hierarchical cluster mergers in their embedded phase. The other mechanism responsible for cluster growth was accretion of the surrounding gas onto the star cluster. Fujii et al. (2012) showed that subcluster mergers are required to create clusters whose density profiles best match observations of young massive clusters. They also showed that the presence of high-velocity unbound stars around the young massive cluster R136 can be explained through subcluster mergers on the timeframe of 3 Myr (consistent with the lifetime of the clusters embedded phase suggested by Pelupessy and Portegies Zwart 2012). In Karam and Sills (2022), we showed that these mergers can induce cluster expansion before gas expulsion and cause a fraction of stars to become ejected from the host cluster even though the entire cluster remains bound. This fraction was shown to be $<10\%$ for merging star clusters (Grudić et al. 2018). Because hierarchical star cluster buildup is non uniform (cluster mergers happen along random directions inside their host environment), it may be the case that the dynamical signatures discussed in Section 1.2 come about because of cluster mergers.

The amount of cluster mergers and their ability to grow cluster mass has been shown to be dependent on local gas properties. For example, Dobbs et al. (2022) studied the assembly histories of clusters in different galactic environments (with different gas distributions) and determined that higher mass gas distributions lead to more mergers and, in turn, higher mass clusters. Lewis et al. (2023) showed that feedback from particularly massive stars (50-100 $M_\odot$) suppresses mergers because of the complete disruption of the surrounding gas distribution.

Simulations have also shown that accretion from surrounding gas onto star clusters is a key way by which a cluster can gain angular momentum (e.g. Lahén et al. 2020). Chen et al. (2021) has shown that clouds with centrally concentrated density profiles form clusters with higher angular momentum. The inherited angular momentum of central clusters from such clouds can be up to five times higher than clusters that form from clouds with constant densities. The authors also show that stars that are ejected thanks to mergers carry with them more angular momentum than the stars that remain implying that mergers can decrease cluster angular momentum. It is still uncertain how this process depends on the direction of the merger.

1.4 Numerical Methods

The following section of this chapter is dedicated to a discussion of the numerical methods used in the simulations presented in Chapters 2, 3, and 4.

1.4.1 `AMUSE`

The simulations presented in Chapters 2 and 3 of this thesis are performed using the `AMUSE` interface (Portegies Zwart et al. 2009, Portegies Zwart et al. 2013, Pelupessy et al. 2013). `AMUSE` is a `python` interface which connects community codes written to perform a wide array of astrophysical calculations from stellar evolution to hydrodynamics. For our simulations, we use the smoothed particle hydrodynamics (SPH) code `Gadget-2` (Springel 2005) to model hydrodynamics and a fourth order Hermite integrator (Makino and Aarseth 1992) for N-body stellar dynamics. In order for the stars handled as N-body particles to interact with the surrounding gas, we use the `BRIDGE` (Fujii et al. 2007) scheme. `BRIDGE` updates the stellar positions based on the gas distribution and vice versa using a gravity code. For details regarding the physics behind these codes, see Karam (2021). The remainder of this subsection is dedicated to a discussion regarding the choices we made for these codes.

Beginning with the hydrodynamics, the smoothing length of each SPH particle is chosen such that a constant mass is enclosed within one smoothing volume of each particle. The mass of each SPH particle is held constant for the simulations presented in Chapters 2 and 3. We choose the smoothing length of the gas particles to be $0.01 r_{scale}$ where r_{scale} is the scale radius of the Plummer (1911) sphere used to initialize the cluster. Gas temperature (T) is set to 10 K and the mean molecular weight (μ) of the gas is set to 2.4 amu allowing us to calculate the internal energy (u) of each gas particle using:

$$u = \frac{3 k_B T}{2 \mu} \tag{1.8}$$

where k_B is the Boltzmann constant.

For the N-body calculations, we need initial positions, velocities and masses of our stars. We initialize our star clusters using the Plummer sphere scheme described in Karam (2021) to calculate the positions and velocities. The gravitational softening of the star particles is set to $0.001 r_{scale}$ meaning that binary stars are not considered in the simulations presented in Chapters 2 and 3. Lastly, the masses of each star are randomly sampled from a Kroupa (2001) IMF.

For the `BRIDGE` scheme, we need to choose a timestep for the interaction between the gas and stars. We choose this to be 870 yr as we find that this best conserves energy throughout the simulation.

1.4.2 `ASURA+BRIDGE`

The simulation performed in Chapter 4 makes use of the `ASURA+BRIDGE` (Fujii, Saitoh, Hirai and Wang 2021, Fujii, Saitoh, Wang and Hirai 2021) simulation code. The gas component of `ASURA+BRIDGE` is evolved using `ASURA`, an SPH method presented in Saitoh et al. (2008) and Saitoh et al. (2009). The N-body component is evolved using `PeTar` (Wang, Iwasawa, Nitadori and Makino 2020). Our use of `ASURA+BRIDGE` is a direct upgrade from our previous simulations in the following key ways.

The first improvement in `ASURA+BRIDGE` is through the N-body solver. `PeTar` combines a Hermite integrator with a Barnes-Hut tree (Barnes and Hut 1986) (used for long range interactions) and a slow down regularization algorithm (SDAR, Wang, Nitadori and Makino 2020) to help model the evolution of binary stars. SDAR combines the slow-down (SD) method (Mikkola and Aarseth 1996) with algorithmic regularization (AR) which is efficient at solving the long term evolution of few body systems.

The goal of the SD method is to reduce the number of integration steps needed to forward model weakly perturbed binary systems. This is done by modifying the Hamiltonian of a binary system:

$$H_{SD} = \frac{1}{\kappa} H_b + (H - H_b) \tag{1.9}$$

where H_{SD} is the modified Hamiltonian, H_b is the Hamiltonian of the binary system, H is the original Hamiltonian, and κ is a slow down factor. This lowers the effective period of the binary system by a factor of κ^{-1}. By solving the equations of motions using H_{SD}, Mikkola and Aarseth (1996) showed that the positions and velocities of the binary can be accurately retrieved. However, the orbital phase information of the binary system is lost through this method. Coupling the SD and AR methods together allows for the accurate resolution of binary and multiple systems over the timescales necessary for our simulations. The gravitational softening for stars is therefore set to 0.

`ASURA+BRIDGE` also allows for the formation of new stars from SPH gas particles. To form stars, gas particles must satisfy the following conditions:

- The gas must be above a given density threshold (typically between $\approx 10^3 - 10^5 \mathrm{cm}^{-3}$)
- The gas must by below a given temperature threshold (typically ≈ 10 K)
- The gas must be converging (i.e. $\nabla \cdot v < 0$ where v is the gas velocity)

Once gas that satisfies all of the above conditions has been identified, a probability is calculated using:

$$p = \frac{m_{gas}}{\langle m_* \rangle} \left[1 - \exp\left(-c_* \frac{\Delta t}{t_{dyn}} \right) \right] \tag{1.10}$$

where m_{gas} is the mass of a gas particle, $\langle m_* \rangle$ is the average stellar mass from the Kroupa (2001) IMF, c_* is the dimensionless star formation efficiency, Δt is the time interval for star formation, and t_{dyn} is the dynamical time of the gas. If the value p is greater than a random number chosen between 0 and 1, that gas is assigned a stellar mass sampled from the Kroupa (2001) IMF.

There are two different regimes that can occur to form a star particle. The first is where the sampled stellar mass is lower than the gas particle mass from which the star forms. In this case, the star particle is placed in the simulation and the gas particle has its mass reduced by $\Delta m = m_{gas} - m_*$. The positions and velocities of the newly formed star particle are taken from the parent gas particle.

The second case occurs when the gas particle mass is lower than the sampled star particle mass. In this case, a search radius is used to assemble the gas required to equal the star particle mass. The search radius is estimated using:

$$r_{th} = \left(\frac{3 m_*}{4 \pi n_H m_H} \right)^{\frac{1}{3}} \tag{1.11}$$

where n_H is the number density of hydrogen, and m_H is the mass of hydrogen. The gas particle at the centre of this region is then converted into a star particle. In this case, the positions and velocities of the newly formed star particle are chosen to conserve momentum. They are calculated using the following two equations respectively:

$$\vec{x}_{*,new} = \frac{m_* \vec{x}_{gas,p} + f \sum_{i=0}^{N_{list}} m_{gas,i} \vec{x}_{gas,i}}{m_* + f \sum_{i=0}^{N_l ist} m_{gas,i}} \tag{1.12}$$

$$\vec{v}_{*,new} = \frac{m_* \vec{v}_{gas,p} + f \sum_{i=0}^{N_{list}} m_{gas,i} \vec{v}_{gas,i}}{m_* + f \sum_{i=0}^{N_{list}} m_{gas,i}} \tag{1.13}$$

Here, $\vec{x}_{gas,i}$ is the position of the ith particle used to assemble the stellar mass, $\vec{v}_{gas,i}$ is the velocity of the ith particle used to assemble the stellar mass, $m_{gas,i}$ is the mass of the ith particle used to assemble the stellar mass, and $f = (m_* - m_{gas})/m_{inc}$ is the amount of reduced gas mass. Lastly, m_{inc} is the total mass of gas in the enclosed region. The final step is to reduce the masses of the particles surrounding the newly formed star to ensure mass conservation. The masses are reduced by $(1 - f)m_{gas}$.

The last key addition brought by the use of `ASURA+BRIDGE` is the inclusion of stellar feedback which is handled using a Strömgren radius (Strömgren 1939) calculation. The Strömgren radius is calculated using:

$$R_{St} = \left(\frac{3Q}{4\pi\alpha_B n_H^2} \right)^{\frac{1}{3}} \tag{1.14}$$

where Q is the rate at which ionizing photons are emitted from the source star, and $\alpha_B = 2.6 \times 10^{-13}\text{cm}^3\text{s}^{-1}$ is the recombination coefficient (Osterbrock and Ferland 2006). The value of Q is obtained using tables constructed from stellar atmosphere models presented in Lanz and Hubeny (2003) and a single star evolution code (Hurley et al. 2000) to estimate the effective temperature and radius of a star. From this, a relation between Q and m_* is found:

$$\log Q = a + bx + cx^2 + dx^3 + ex^4 + fx^5 \tag{1.15}$$

where $x \equiv \log m_*$, and a, b, c, d, e, and f are constant coefficients that are solved for. Thermal energy is provided to the gas within the Strömgren radius around a given star by giving the gas a temperature of 10^4K.

Momentum is given to the gas within the Strömgren radius using a series of velocity kicks. The first kick comes from the radiation pressure felt by the surrounding gas and is given by Kim et al. (2016) as:

$$\Delta v_i = \frac{Q\langle h\nu \rangle_i}{M_{H_{II}} c} \Delta t \tag{1.16}$$

where $\langle h\nu \rangle_i = 18.6$eV is the mean photon energy above the Lyman alpha limit, $M_{H_{II}}$ is the gas mass within the H_{II} region, c is the speed of light, and Δt is the time interval over which the velocity kick is given to the gas particles.

The second kick is calculated using a model that accounts for dust absorption of photons whose energies are greater than 13.3eV which results in a velocity kick. To

calculate this kick, we first note that the dust grains absorb both ionizing and nonionizing radiation meaning that we need to take into account both components in the luminosity of the star. Kim et al. (2016) show that the total luminosity can be given by

$$L = L_i \phi(r) + L_n e^{-\tau_d(r)} \tag{1.17}$$

where L_i is the ionizing luminosity, $\phi(r)$ is the attenuation for ionizing photons which is set to a constant 1, L_n is the luminosity of the non-ionizing photons, and τ_d is the optical depth of the non-ionizing photons. The optical depth can be calculated using

$$\tau_d(r) = \int_0^r n \sigma_d dr \tag{1.18}$$

where $\sigma_d = 1.0 \times 10^{21} \mathrm{cm}^2 \mathrm{H}^{-1}$ is the cross section per hydrogen nucleus. Using the Strömgren radius, we can calculate the volume density in the HII region around the star using

$$\rho = \frac{3 M_{H_{II}}}{4\pi (R_{St}^3 - R_{min}^3)} \tag{1.19}$$

where R_{min} is the distance to the innermost gas particle from the star. This allows us to get the number density n for equation 1.18 using $n = \rho / m_H$. Finally, noting that $Q = L_i / \langle h\nu \rangle_i$ and putting all this together into the velocity kick given by equation 1.16, we get the velocity kick from the absorption by dust grains:

$$\Delta v_{dusty}(r) = \left[\phi + \beta e^{-\tau_d(r)} \right] \frac{Q \langle h\nu \rangle}{M_{H_{II}} c} \Delta t \tag{1.20}$$

where $\beta \equiv L_n / L_i = 1.5$ is assumed following Kim et al. (2016). A final kick from stellar winds is included and calculated using

$$\Delta v_{sw} = 0.673 \Delta v_i \tag{1.21}$$

following the prescription from Dekel and Krumholz (2013).

Because the simulation in Chapter 4 is run for 2 Myr, supernovae are not included.

1.5 Thesis Outline

The above discussion provides the background and motivation necessary for the simulations presented in this thesis. I urge a connection between the observations of star cluster dynamics and the processes that may lead to their formation throughout the

thesis. In order to understand the processes that may lead to their formation, a clear and concise prescription for the gaseous component of young star cluster evolution is necessary. The key aspect of our simulations is this inclusion.

Below, I provide a brief summary of the published works that comprise each chapter of the thesis.

- Chapter 2: *Modelling Star Cluster Formation: Gas Accretion*
  Summary: We study the interaction between a star cluster and its environment by simulating its motion through an ambient background of gas and accretion from nearby filaments. We initialize different instances of background gas with densities of 0.05 $M_{\odot}pc^{-3}$, 0.5 $M_{\odot}pc^{-3}$, and 1 $M_{\odot}pc^{-3}$ and cluster velocities of 4 kms^{-1}, 6 kms^{-1} and 10 kms^{-1}. The filament densities are motivated by observations and are in the range of 310 $M_{\odot}pc^{-3}$ to 1250 $M_{\odot}pc^{-3}$. Both of these processes result in change to the cluster structure through removing or adding bound gas. The fraction of mass change is dependant on the background medium density and cluster velocity but remains relatively constant (within 5%) when we change the filament parameters.

- Chapter 3: *Dynamics of Star Cluster Formation: Mergers in Gas Rich Environments*
  Summary: We study the dynamical imprints of cluster mergers on the clusters involved. We take three regions from the previously run Howard et al. (2018) star cluster formation simulation and resolve the star cluster mergers while including the background gas distribution. Each region contains at least one cluster merger with one region containing two. All three regions create clusters with dynamics matching recent observations. We also compare to simulations of mergers without an ambient gas distribution and find that the background gas is vital in promoting mergers. Mergers that take place along the x-axis with high offsets along the y-axis are more likely to be non-monolithic at lower velocities (<10 kms^{-1}).

- Chapter 4: *Dynamics of Star Cluster Formation: The Effect of Ongoing Star Formation and Stellar Feedback*
  Summary: We rerun the `region1` simulation presented in Chapter 3 with our improved computational methods to study star formation and stellar feedback in cluster mergers. Star formation enhances the magnitude of the dynamical fingerprints of cluster mergers found in Chapter 3 (i.e. increase in velocity dispersion, rotation, and anisotropic expansion). We simulate the cluster until it has removed

its background gas to study its structure and to determine the survivability of these dynamical fingerprints.

Bibliography

Adamo, A., Bradley, L. D., Vanzella, E., Claeyssens, A., Welch, B., Diego, J. M., Mahler, G., Oguri, M., Sharon, K., Abdurro'uf, Hsiao, T. Y.-Y., Xu, X., Messa, M., Lassen, A. E., Zackrisson, E., Brammer, G., Coe, D., Kokorev, V., Ricotti, M., Zitrin, A., Fujimoto, S., Inoue, A. K., Resseguier, T., Rigby, J. R., Jiménez-Teja, Y., Windhorst, R. A., Hashimoto, T. and Tamura, Y. (2024). Bound star clusters observed in a lensed galaxy 460 Myr after the Big Bang, Nature **632**(8025): 513–516.

Alfonso, J. and García-Varela, A. (2023). A Gaia astrometric view of the open clusters Pleiades, Praesepe, and Blanco 1, A&A **677**: A163.

Ali, A. A., Dobbs, C. L., Bending, T. J. R., Buckner, A. S. M. and Pettitt, A. R. (2023). Star cluster formation and feedback in different environments of a Milky Way-like galaxy, MNRAS **524**(1): 555–568.

André, P., Men'shchikov, A., Bontemps, S., Könyves, V., Motte, F., Schneider, N., Didelon, P., Minier, V., Saraceno, P., Ward-Thompson, D., di Francesco, J., White, G., Molinari, S., Testi, L., Abergel, A., Griffin, M., Henning, T., Royer, P., Merín, B., Vavrek, R., Attard, M., Arzoumanian, D., Wilson, C. D., Ade, P., Aussel, H., Baluteau, J. P., Benedettini, M., Bernard, J. P., Blommaert, J. A. D. L., Cambrésy, L., Cox, P., di Giorgio, A., Hargrave, P., Hennemann, M., Huang, M., Kirk, J., Krause, O., Launhardt, R., Leeks, S., Le Pennec, J., Li, J. Z., Martin, P. G., Maury, A., Olofsson, G., Omont, A., Peretto, N., Pezzuto, S., Prusti, T., Roussel, H., Russeil, D., Sauvage, M., Sibthorpe, B., Sicilia-Aguilar, A., Spinoglio, L., Waelkens, C., Woodcraft, A. and Zavagno, A. (2010). From filamentary clouds to prestellar cores to the stellar IMF: Initial highlights from the Herschel Gould Belt Survey, A&A **518**: L102.

Andre, P., Ward-Thompson, D. and Barsony, M. (1993). Submillimeter Continuum Observations of rho Ophiuchi A: The Candidate Protostar VLA 1623 and Prestellar Clumps, ApJ **406**: 122.

Armstrong, J. J. and Tan, J. C. (2024). Expansion kinematics of young clusters: I. Lambda Ori, A&A **692**: A166.

Arzoumanian, D., André, P., Didelon, P., Könyves, V., Schneider, N., Men'shchikov, A., Sousbie, T., Zavagno, A., Bontemps, S., di Francesco, J., Griffin, M., Hennemann, M., Hill, T., Kirk, J., Martin, P., Minier, V., Molinari, S., Motte, F., Peretto, N., Pezzuto, S., Spinoglio, L., Ward-Thompson, D., White, G. and Wilson, C. D. (2011). Characterizing interstellar filaments with Herschel in IC 5146, A&A **529**: L6.

Arzoumanian, D., André, P., Könyves, V., Palmeirim, P., Roy, A., Schneider, N., Benedettini, M., Didelon, P., Di Francesco, J., Kirk, J. and Ladjelate, B. (2019). Characterizing the properties of nearby molecular filaments observed with Herschel, A&A **621**: A42.

Barnes, J. and Hut, P. (1986). A hierarchical O(N log N) force-calculation algorithm, *Nature Astronomy* **324**(6096): 446–449.

Bastian, N. and Goodwin, S. P. (2006). Evidence for the strong effect of gas removal on the internal dynamics of young stellar clusters, MNRAS **369**(1): L9–L13.

Baumgardt, H. and Kroupa, P. (2007). A comprehensive set of simulations studying the influence of gas expulsion on star cluster evolution, MNRAS **380**(4): 1589–1598.

Blaauw, A. (1946). A Study of the Scorpio-Centaurus Cluster, *Publications of the Kapteyn Astronomical Laboratory Groningen* **52**: 1–132.

Boily, C. M. and Kroupa, P. (2003). The impact of mass loss on star cluster formation - II. Numerical N-body integration and further applications, MNRAS **338**(3): 673–686.

Cantat-Gaudin, T. and Anders, F. (2020). Clusters and mirages: cataloguing stellar aggregates in the Milky Way, A&A **633**: A99.

Cantat-Gaudin, T., Anders, F., Castro-Ginard, A., Jordi, C., Romero-Gómez, M., Soubiran, C., Casamiquela, L., Tarricq, Y., Moitinho, A., Vallenari, A., Bragaglia, A., Krone-Martins, A. and Kounkel, M. (2020). Painting a portrait of the Galactic disc with its stellar clusters, A&A **640**: A1.

Chabrier, G. (2003). Galactic Stellar and Substellar Initial Mass Function, PASP **115**(809): 763–795.

Chen, Y., Li, H. and Vogelsberger, M. (2021). Effects of initial density profiles on massive star cluster formation in giant molecular clouds, MNRAS **502**(4): 6157–6169.

Chevance, M., Krumholz, M. R., McLeod, A. F., Ostriker, E. C., Rosolowsky, E. W. and Sternberg, A. (2023). The Life and Times of Giant Molecular Clouds, *in* S. Inutsuka, Y. Aikawa, T. Muto, K. Tomida and M. Tamura (eds), *Protostars and Planets VII*, Vol. 534 of *Astronomical Society of the Pacific Conference Series*, p. 1.

Cournoyer-Cloutier, C., Tran, A., Lewis, S., Wall, J. E., Harris, W. E., Mac Low, M.-M., McMillan, S. L. W., Portegies Zwart, S. and Sills, A. (2021). Implementing primordial

binaries in simulations of star cluster formation with a hybrid MHD and direct N-body method, MNRAS **501**(3): 4464–4478.

Dekel, A. and Krumholz, M. R. (2013). Steady outflows in giant clumps of high-z disc galaxies during migration and growth by accretion, MNRAS **432**(1): 455–467.

Della Croce, A., Dalessandro, E., Livernois, A. and Vesperini, E. (2024). Young, wild, and free: The early expansion of star clusters, A&A **683**: A10.

Dewangan, L. K., Bhadari, N. K., Maity, A. K., Eswaraiah, C., Sharma, S. and Jadhav, O. R. (2024). Galactic 'Snake' IRDC G11.11-0.12: a site of multiple hub-filament systems and colliding filamentary clouds, MNRAS **527**(3): 5895–5915.

Dobbs, C. L., Bending, T. J. R., Pettitt, A. R., Buckner, A. S. M. and Bate, M. R. (2022). The formation of clusters and OB associations in different density spiral arm environments, MNRAS **517**(1): 675–696.

Fahrion, K. and De Marchi, G. (2024). The hierarchical formation of 30 Doradus as seen by JWST, A&A **681**: A20.

Fujii, M., Iwasawa, M., Funato, Y. and Makino, J. (2007). BRIDGE: A Direct-Tree Hybrid N-Body Algorithm for Fully Self-Consistent Simulations of Star Clusters and Their Parent Galaxies, *PASJ* **59**: 1095.

Fujii, M. S., Saitoh, T. R., Hirai, Y. and Wang, L. (2021). SIRIUS project. III. Star-by-star simulations of star cluster formation using a direct N-body integrator with stellar feedback, PASJ **73**(4): 1074–1099.

Fujii, M. S., Saitoh, T. R. and Portegies Zwart, S. F. (2012). The Formation of Young Dense Star Clusters through Mergers, ApJ **753**(1): 85.

Fujii, M. S., Saitoh, T. R., Wang, L. and Hirai, Y. (2021). SIRIUS project. II. A new tree-direct hybrid code for smoothed particle hydrodynamics/N-body simulations of star clusters, PASJ **73**(4): 1057–1073.

Fukui, Y., Tokuda, K., Saigo, K., Harada, R., Tachihara, K., Tsuge, K., Inoue, T., Torii, K., Nishimura, A., Zahorecz, S., Nayak, O., Meixner, M., Minamidani, T., Kawamura, A., Mizuno, N., Indebetouw, R., Sewiło, M., Madden, S., Galametz, M., Lebouteiller, V., Chen, C. H. R. and Onishi, T. (2019). An ALMA View of Molecular Filaments in the Large Magellanic Cloud. I. The Formation of High-mass Stars and Pillars in the N159E-Papillon Nebula Triggered by a Cloud-Cloud Collision, ApJ **886**(1): 14.

Fukushima, H. and Yajima, H. (2021). Radiation hydrodynamics simulations of massive star cluster formation in giant molecular clouds, MNRAS **506**(4): 5512–5539.

Gaia Collaboration, Babusiaux, C., van Leeuwen, F., Barstow, M. A., Jordi, C., Vallenari, A., Bossini, D., Bressan, A., Cantat-Gaudin, T., van Leeuwen, M., Brown, A. G. A., Prusti, T., de Bruijne, J. H. J., Bailer-Jones, C. A. L., Biermann, M., Evans, D. W., Eyer, L., Jansen, F., Klioner, S. A., Lammers, U., Lindegren, L., Luri, X., Mignard, F., Panem, C., Pourbaix, D., Randich, S., Sartoretti, P., Siddiqui, H. I., Soubiran, C., Walton, N. A., Arenou, F., Bastian, U., Cropper, M., Drimmel, R., Katz, D., Lattanzi, M. G., Bakker, J., Cacciari, C., Castañeda, J., Chaoul, L., Cheek, N., De Angeli, F., Fabricius, C., Guerra, R., Holl, B., Masana, E., Messineo, R., Mowlavi, N., Nienartowicz, K., Panuzzo, P., Portell, J., Riello, M., Seabroke, G. M., Tanga, P., Thévenin, F., Gracia-Abril, G., Comoretto, G., Garcia-Reinaldos, M., Teyssier, D., Altmann, M., Andrae, R., Audard, M., Bellas-Velidis, I., Benson, K., Berthier, J., Blomme, R., Burgess, P., Busso, G., Carry, B., Cellino, A., Clementini, G., Clotet, M., Creevey, O., Davidson, M., De Ridder, J., Delchambre, L., Dell'Oro, A., Ducourant, C., Fernández-Hernández, J., Fouesneau, M., Frémat, Y., Galluccio, L., García-Torres, M., González-Núñez, J., González-Vidal, J. J., Gosset, E., Guy, L. P., Halbwachs, J. L., Hambly, N. C., Harrison, D. L., Hernández, J., Hestroffer, D., Hodgkin, S. T., Hutton, A., Jasniewicz, G., Jean-Antoine-Piccolo, A., Jordan, S., Korn, A. J., Krone-Martins, A., Lanzafame, A. C., Lebzelter, T., Löffler, W., Manteiga, M., Marrese, P. M., Martín-Fleitas, J. M., Moitinho, A., Mora, A., Muinonen, K., Osinde, J., Pancino, E., Pauwels, T., Petit, J. M., Recio-Blanco, A., Richards, P. J., Rimoldini, L., Robin, A. C., Sarro, L. M., Siopis, C., Smith, M., Sozzetti, A., Süveges, M., Torra, J., van Reeven, W., Abbas, U., Abreu Aramburu, A., Accart, S., Aerts, C., Altavilla, G., Álvarez, M. A., Alvarez, R., Alves, J., Anderson, R. I., Andrei, A. H., Anglada Varela, E., Antiche, E., Antoja, T., Arcay, B., Astraatmadja, T. L., Bach, N., Baker, S. G., Balaguer-Núñez, L., Balm, P., Barache, C., Barata, C., Barbato, D., Barblan, F., Barklem, P. S., Barrado, D., Barros, M., Bartholomé Muñoz, L., Bassilana, J. L., Becciani, U., Bellazzini, M., Berihuete, A., Bertone, S., Bianchi, L., Bienaymé, O., Blanco-Cuaresma, S., Boch, T., Boeche, C., Bombrun, A., Borrachero, R., Bouquillon, S., Bourda, G., Bragaglia, A., Bramante, L., Breddels, M. A., Brouillet, N., Brüsemeister, T., Brugaletta, E., Bucciarelli, B., Burlacu, A., Busonero, D., Butkevich, A. G., Buzzi, R., Caffau, E., Cancelliere, R., Cannizzaro, G., Carballo, R., Carlucci, T., Carrasco, J. M., Casamiquela, L., Castellani, M., Castro-Ginard, A., Charlot, P., Chemin, L., Chiavassa, A., Cocozza, G., Costigan, G., Cowell, S., Crifo, F., Crosta, M., Crowley, C., Cuypers, J., Dafonte, C., Damerdji, Y.,

Dapergolas, A., David, P., David, M. and de Laverny, P. (2018). Gaia Data Release 2. Observational Hertzsprung-Russell diagrams, A&A **616**: A10.

Geyer, M. P. and Burkert, A. (2001). The effect of gas loss on the formation of bound stellar clusters, MNRAS **323**(4): 988–994.

Gnedin, O. Y. and Ostriker, J. P. (1997). Destruction of the Galactic Globular Cluster System, ApJ **474**(1): 223–255.

Griffen, B. F., Drinkwater, M. J., Thomas, P. A., Helly, J. C. and Pimbblet, K. A. (2010). Globular cluster formation within the Aquarius simulation, MNRAS **405**(1): 375–386.

Grudić, M. Y., Guszejnov, D., Hopkins, P. F., Lamberts, A., Boylan-Kolchin, M., Murray, N. and Schmitz, D. (2018). From the top down and back up again: star cluster structure from hierarchical star formation, MNRAS **481**(1): 688–702.

Hacar, A., Konietzka, R., Seifried, D., Clark, S. E., Socci, A., Bonanomi, F., Burkert, A., Schisano, E., Kainulainen, J. and Smith, R. (2025). Emergence of high-mass stars in complex fiber networks (EMERGE): V. From filaments to spheroids: the origin of the hub-filament systems, A&A **694**: A69.

Hao, C. J., Xu, Y., Hou, L. G., Bian, S. B., Lin, Z. H., Li, Y. J., Dong, Y. W. and Liu, D. J. (2024). Probing the Nature of Rotation in the Pleiades, Alpha Persei, and Hyades Clusters, ApJ **963**(2): 153.

Hénault-Brunet, V., Gieles, M., Evans, C. J., Sana, H., Bastian, N., Maíz Apellániz, J., Taylor, W. D., Markova, N., Bressert, E., de Koter, A. and van Loon, J. T. (2012). The VLT-FLAMES Tarantula Survey. VI. Evidence for rotation of the young massive cluster R136, A&A **545**: L1.

Heyer, M. H. and Brunt, C. M. (2004). The Universality of Turbulence in Galactic Molecular Clouds, ApJ **615**(1): L45–L48.

Howard, C. S., Pudritz, R. E. and Harris, W. E. (2018). A universal route for the formation of massive star clusters in giant molecular clouds, *Nature Astronomy* **2**: 725–730.

Hurley, J. R., Pols, O. R. and Tout, C. A. (2000). Comprehensive analytic formulae for stellar evolution as a function of mass and metallicity, MNRAS **315**(3): 543–569.

Inutsuka, S.-I. and Miyama, S. M. (1992). Self-similar Solutions and the Stability of Collapsing Isothermal Filaments, ApJ **388**: 392.

Inutsuka, S.-i. and Miyama, S. M. (1997). A Production Mechanism for Clusters of Dense Cores, ApJ **480**(2): 681–693.

Jiang, S. D. and Hillenbrand, L. A. (2024). The Emerging Stellar Complex in Mon R2: Membership and Optical Variability Classification, AJ **167**(5): 221.

Kamann, S., Bastian, N. J., Gieles, M., Balbinot, E. and Hénault-Brunet, V. (2019). Linking the rotation of a cluster to the spins of its stars: the kinematics of NGC 6791 and NGC 6819 in 3D, MNRAS **483**(2): 2197–2206.

Karam, J. (2021). *Modelling young massive cluster formation: Mergers*, Master's thesis, McMaster University.
URL: *http://hdl.handle.net/11375/27342*

Karam, J. and Sills, A. (2022). Modelling star cluster formation: mergers, MNRAS **513**(4): 6095–6104.

Keown, J., Di Francesco, J., Rosolowsky, E., Singh, A., Figura, C., Kirk, H., Anderson, L. D., Chen, M. C.-Y., Elia, D., Friesen, R., Ginsburg, A., Marston, A., Pezzuto, S., Schisano, E., Bontemps, S., Caselli, P., Liu, H.-L., Longmore, S., Motte, F., Myers, P. C., Offner, S. S. R., Sanhueza, P., Schneider, N., Stephens, I., Urquhart, J. and KEYSTONE Collaboration (2019). KFPA Examinations of Young STellar Object Natal Environments (KEYSTONE): Hierarchical Ammonia Structures in Galactic Giant Molecular Clouds, ApJ **884**(1): 4.

Kerr, R. M. P., Rizzuto, A. C., Kraus, A. L. and Offner, S. S. R. (2021). Stars with Photometrically Young Gaia Luminosities Around the Solar System (SPYGLASS). I. Mapping Young Stellar Structures and Their Star Formation Histories, ApJ **917**(1): 23.

Kim, J.-G., Kim, W.-T. and Ostriker, E. C. (2016). Disruption of Molecular Clouds by Expansion of Dusty H II Regions, ApJ **819**(2): 137.

Kirk, H., Myers, P. C., Bourke, T. L., Gutermuth, R. A., Hedden, A. and Wilson, G. W. (2013). Filamentary Accretion Flows in the Embedded Serpens South Protocluster, ApJ **766**(2): 115.

Kong, S. (2019). The Core Mass Function in the Infrared Dark Cloud G28.37+0.07, ApJ **873**(1): 31.

Könyves, V., André, P., Men'shchikov, A., Palmeirim, P., Arzoumanian, D., Schneider, N., Roy, A., Didelon, P., Maury, A., Shimajiri, Y., Di Francesco, J., Bontemps,

S., Peretto, N., Benedettini, M., Bernard, J. P., Elia, D., Griffin, M. J., Hill, T., Kirk, J., Ladjelate, B., Marsh, K., Martin, P. G., Motte, F., Nguyên Luong, Q., Pezzuto, S., Roussel, H., Rygl, K. L. J., Sadavoy, S. I., Schisano, E., Spinoglio, L., Ward-Thompson, D. and White, G. J. (2015). A census of dense cores in the Aquila cloud complex: SPIRE/PACS observations from the Herschel Gould Belt survey, A&A **584**: A91.

Kounkel, M., Stassun, K. G., Covey, K. and Hartmann, L. (2022). A gravitational and dynamical framework of star formation: the Orion nebula, MNRAS **517**(1): 161–174.

Kroupa, P. (2001). On the variation of the initial mass function, MNRAS **322**(2): 231–246.

Krumholz, M. R., McKee, C. F. and Bland-Hawthorn, J. (2019). Star Clusters Across Cosmic Time, *Annual Reviews of* A&A **57**: 227–303.

Kuhn, M. A., Hillenbrand, L. A., Sills, A., Feigelson, E. D. and Getman, K. V. (2019). Kinematics in Young Star Clusters and Associations with Gaia DR2, ApJ **870**(1): 32.

Kumar, M. S. N., Arzoumanian, D., Men'shchikov, A., Palmeirim, P., Matsumura, M. and Inutsuka, S. (2022). Filament coalescence and hub structure in Mon R2. Implications for massive star and cluster formation, A&A **658**: A114.

Lada, C. J. (1987). Star formation: from OB associations to protostars., *in* M. Peimbert and J. Jugaku (eds), *Star Forming Regions*, Vol. 115 of *IAU Symposium*, p. 1.

Lada, C. J. and Lada, E. A. (2003). Embedded Clusters in Molecular Clouds, *Annual Reviews of* A&A **41**: 57–115.

Lahén, N., Naab, T., Johansson, P. H., Elmegreen, B., Hu, C.-Y. and Walch, S. (2020). Structure and Rotation of Young Massive Star Clusters in a Simulated Dwarf Starburst, ApJ **904**(1): 71.

Lanz, T. and Hubeny, I. (2003). A Grid of Non-LTE Line-blanketed Model Atmospheres of O-Type Stars, ApJS **146**(2): 417–441.

Leanza, S., Pallanca, C., Ferraro, F. R., Lanzoni, B., Dalessandro, E., Origlia, L., Mucciarelli, A., Valenti, E., Tiongco, M., Varri, A. L. and Vesperini, E. (2022). The ESO-VLT MIKiS Survey Reloaded: Velocity Dispersion Profile and Rotation Curve of NGC 1904, ApJ **929**(2): 186.

Leanza, S., Pallanca, C., Ferraro, F. R., Lanzoni, B., Vesperini, E., Cadelano, M., Origlia, L., Fanelli, C., Dalessandro, E. and Valenti, E. (2024). The ESO-VLT MIKiS survey reloaded: The internal kinematics of the core of M75, A&A **688**: A133.

Lewis, S. C., McMillan, S. L. W., Mac Low, M.-M., Cournoyer-Cloutier, C., Polak, B., Wilhelm, M. J. C., Tran, A., Sills, A., Portegies Zwart, S., Klessen, R. S. and Wall, J. E. (2023). Early-forming Massive Stars Suppress Star Formation and Hierarchical Cluster Assembly, ApJ **944**(2): 211.

Li, H., Vogelsberger, M., Marinacci, F. and Gnedin, O. Y. (2019). Disruption of giant molecular clouds and formation of bound star clusters under the influence of momentum stellar feedback, MNRAS **487**(1): 364–380.

Lim, B., Hong, J., Lee, J., Yun, H.-S., Hwang, N. and Park, B.-G. (2023). The Kinematics of the Young Stellar Population in the W5 Region of the Cassiopeia OB6 Association: Implication for the Formation Process of Stellar Associations, AJ **166**(3): 97.

Livernois, A. R., Vesperini, E., Varri, A. L., Hong, J. and Tiongco, M. (2022). Long-term evolution of multimass rotating star clusters, MNRAS **512**(2): 2584–2593.

Mackey, A. D., Da Costa, G. S., Ferguson, A. M. N. and Yong, D. (2013). A VLT/FLAMES Study of the Peculiar Intermediate-age Large Magellanic Cloud Star Cluster NGC 1846. I. Kinematics, ApJ **762**(1): 65.

Makino, J. and Aarseth, S. J. (1992). On a Hermite Integrator with Ahmad-Cohen Scheme for Gravitational Many-Body Problems, *PASJ* **44**: 141–151.

Megeath, S. T., Gutermuth, R. A. and Kounkel, M. A. (2022). Low Mass Stars as Tracers of Star and Cluster Formation, PASP **134**(1034): 042001.

Mikkola, S. and Aarseth, S. J. (1996). A Slow-down Treatment for Close Binaries, *Celestial Mechanics and Dynamical Astronomy* **64**(3): 197–208.

Motte, F., Nony, T., Louvet, F., Marsh, K. A., Bontemps, S., Whitworth, A. P., Men'shchikov, A., Nguyen Luong, Q., Csengeri, T., Maury, A. J., Gusdorf, A., Chapillon, E., Könyves, V., Schilke, P., Duarte-Cabral, A., Didelon, P. and Gaudel, M. (2018). The unexpectedly large proportion of high-mass star-forming cores in a Galactic mini-starburst, *Nature Astronomy* **2**: 478–482.

Nagasawa, M. (1987). Gravitational Instability of the Isothermal Gas Cylinder with an Axial magnetic Field, *Progress of Theoretical Physics* **77**(3): 635–652.

Osterbrock, D. E. and Ferland, G. J. (2006). *Astrophysics of gaseous nebulae and active galactic nuclei*.

Ostriker, J. (1964). The Equilibrium of Polytropic and Isothermal Cylinders., ApJ **140**: 1056.

Pavlík, V. and Vesperini, E. (2021). New insights into star cluster evolution towards energy equipartition, MNRAS **504**(1): L12–L16.

Pelupessy, F. I. and Portegies Zwart, S. (2012). The evolution of embedded star clusters, MNRAS **420**(2): 1503–1517.

Pelupessy, F. I., van Elteren, A., de Vries, N., McMillan, S. L. W., Drost, N. and Portegies Zwart, S. F. (2013). The Astrophysical Multipurpose Software Environment, A&A **557**: A84.

Peretto, N., Fuller, G. A., André, P., Arzoumanian, D., Rivilla, V. M., Bardeau, S., Duarte Puertas, S., Guzman Fernandez, J. P., Lenfestey, C., Li, G. X., Olguin, F. A., Röck, B. R., de Villiers, H. and Williams, J. (2014). SDC13 infrared dark clouds: Longitudinally collapsing filaments?, A&A **561**: A83.

Pfalzner, S. (2009). Universality of young cluster sequences, A&A **498**(2): L37–L40.

Pfalzner, S. and Kaczmarek, T. (2013). The expansion of massive young star clusters - observation meets theory, A&A **559**: A38.

Plummer, H. C. (1911). On the problem of distribution in globular star clusters, MNRAS **71**: 460–470.

Portegies Zwart, S. F., McMillan, S. L. W. and Gieles, M. (2010). Young Massive Star Clusters, *Annual Reviews of* A&A **48**: 431–493.

Portegies Zwart, S., McMillan, S., Harfst, S., Groen, D., Fujii, M., Nualláin, B. Ó., Glebbeek, E., Heggie, D., Lombardi, J., Hut, P., Angelou, V., Banerjee, S., Belkus, H., Fragos, T., Fregeau, J., Gaburov, E., Izzard, R., Jurić, M., Justham, S., Sottoriva, A., Teuben, P., van Bever, J., Yaron, O. and Zemp, M. (2009). A multiphysics and multiscale software environment for modeling astrophysical systems, *New Astronomy* **14**(4): 369–378.

Portegies Zwart, S., McMillan, S. L. W., van Elteren, E., Pelupessy, I. and de Vries, N. (2013). Multi-physics simulations using a hierarchical interchangeable software interface, *Computer Physics Communications* **184**(3): 456–468.

Pouteau, Y., Motte, F., Nony, T., Galván-Madrid, R., Men'shchikov, A., Bontemps, S., Robitaille, J. F., Louvet, F., Ginsburg, A., Herpin, F., López-Sepulcre, A., Dell'Ova, P., Gusdorf, A., Sanhueza, P., Stutz, A. M., Brouillet, N., Thomasson, B., Armante, M., Baug, T., Bonfand, M., Busquet, G., Csengeri, T., Cunningham, N., Fernández-López, M., Liu, H. L., Olguin, F., Towner, A. P. M., Bally, J., Braine, J., Bronfman, L., Joncour, I., González, M., Hennebelle, P., Lu, X., Menten, K. M., Moraux, E., Tatematsu, K., Walker, D. and Whitworth, A. P. (2022). ALMA-IMF. III. Investigating the origin of stellar masses: top-heavy core mass function in the W43-MM2&MM3 mini-starburst, A&A **664**: A26.

Racine, R. (1968). Stars in reflection nebulae., AJ **73**: 233–245.

Rayner, T. S. M., Griffin, M. J., Schneider, N., Motte, F., Könyves, V., André, P., Di Francesco, J., Didelon, P., Pattle, K., Ward-Thompson, D., Anderson, L. D., Benedettini, M., Bernard, J. P., Bontemps, S., Elia, D., Fuente, A., Hennemann, M., Hill, T., Kirk, J., Marsh, K., Men'shchikov, A., Nguyen Luong, Q., Peretto, N., Pezzuto, S., Rivera-Ingraham, A., Roy, A., Rygl, K., Sánchez-Monge, Á., Spinoglio, L., Tigé, J., Treviño-Morales, S. P. and White, G. J. (2017). Far-infrared observations of a massive cluster forming in the Monoceros R2 filament hub, A&A **607**: A22.

Ricotti, M. (2002). Did globular clusters reionize the Universe?, MNRAS **336**(2): L33–L37.

Rosolowsky, E., Engargiola, G., Plambeck, R. and Blitz, L. (2003). Giant Molecular Clouds in M33. II. High-Resolution Observations, ApJ **599**(1): 258–274.

Saitoh, T. R., Daisaka, H., Kokubo, E., Makino, J., Okamoto, T., Tomisaka, K., Wada, K. and Yoshida, N. (2008). Toward First-Principle Simulations of Galaxy Formation: I. How Should We Choose Star-Formation Criteria in High-Resolution Simulations of Disk Galaxies?, PASJ **60**(4): 667–681.

Saitoh, T. R., Daisaka, H., Kokubo, E., Makino, J., Okamoto, T., Tomisaka, K., Wada, K. and Yoshida, N. (2009). Toward First-Principle Simulations of Galaxy Formation: II. Shock-Induced Starburst at a Collision Interface during the First Encounter of Interacting Galaxies, PASJ **61**: 481.

Seshadri, A., Vig, S., Ghosh, S. K. and Ojha, D. K. (2024). Massive star formation in the hub-filament system of RCW 117, MNRAS **527**(2): 4244–4259.

Sokol, A. D., Gutermuth, R. A., Pokhrel, R., Gómez-Ruiz, A. I., Wilson, G. W., Offner, S. S. R., Heyer, M., Luna, A., Schloerb, F. P. and Sánchez, D. (2019). Early science

with the Large Millimetre Telescope: An LMT/AzTEC 1.1 mm Survey of dense cores in the Monoceros R2 giant molecular cloud, MNRAS **483**(1): 407–424.

Springel, V. (2005). The cosmological simulation code GADGET-2, MNRAS **364**(4): 1105–1134.

Strömgren, B. (1939). The Physical State of Interstellar Hydrogen., ApJ **89**: 526.

Theissen, C. A., Konopacky, Q. M., Lu, J. R., Kim, D., Zhang, S. Y., Hsu, C.-C., Chu, L. and Wei, L. (2022). The 3D Kinematics of the Orion Nebula Cluster: NIRSPEC-AO Radial Velocities of the Core Population, ApJ **926**(2): 141.

Tiongco, M. A., Vesperini, E. and Varri, A. L. (2017). Kinematical evolution of tidally limited star clusters: rotational properties, MNRAS **469**(1): 683–692.

Tokuda, K., Kunitoshi, Y., Zahorecz, S., Tanaka, K. E. I., Murakoso, I., Harada, N., Kobayashi, M. I. N., Inoue, T., Sewiło, M., Konishi, A., Shimonishi, T., Zhang, Y., Fukui, Y., Kawamura, A., Onishi, T. and Machida, M. N. (2025). ALMA 0.1 pc View of Molecular Clouds Associated with High-mass Protostellar Systems in the Small Magellanic Cloud: Are Low-metallicity Clouds Filamentary or Not?, ApJ **980**(2): 269.

Treviño-Morales, S. P., Fuente, A., Sánchez-Monge, Á., Kainulainen, J., Didelon, P., Suri, S., Schneider, N., Ballesteros-Paredes, J., Lee, Y. N., Hennebelle, P., Pilleri, P., González-García, M., Kramer, C., García-Burillo, S., Luna, A., Goicoechea, J. R., Tremblin, P. and Geen, S. (2019). Dynamics of cluster-forming hub-filament systems. The case of the high-mass star-forming complex Monoceros R2, A&A **629**: A81.

Vanzella, E., Caminha, G. B., Calura, F., Cupani, G., Meneghetti, M., Castellano, M., Rosati, P., Mercurio, A., Sani, E., Grillo, C., Gilli, R., Mignoli, M., Comastri, A., Nonino, M., Cristiani, S., Giavalisco, M. and Caputi, K. (2020). Ionizing the intergalactic medium by star clusters: the first empirical evidence, MNRAS **491**(1): 1093–1103.

Vesperini, E., Varri, A. L., McMillan, S. L. W. and Zepf, S. E. (2014). Kinematical fingerprints of star cluster early dynamical evolution., MNRAS **443**: L79–L83.

Wang, L., Iwasawa, M., Nitadori, K. and Makino, J. (2020). PETAR: a high-performance N-body code for modelling massive collisional stellar systems, MNRAS **497**(1): 536–555.

Wang, L., Nitadori, K. and Makino, J. (2020). A slow-down time-transformed symplectic integrator for solving the few-body problem, MNRAS **493**(3): 3398–3411.

Wong, T., Oudshoorn, L., Sofovich, E., Green, A., Shah, C., Indebetouw, R., Meixner, M., Hacar, A., Nayak, O., Tokuda, K., Bolatto, A. D., Chevance, M., De Marchi, G., Fukui, Y., Hirschauer, A. S., Jameson, K. E., Kalari, V., Lebouteiller, V., Looney, L. W., Madden, S. C., Onishi, T., Roman-Duval, J., Rubio, M. and Tielens, A. G. G. M. (2022). The 30 Doradus Molecular Cloud at 0.4 pc Resolution with the Atacama Large Millimeter/submillimeter Array: Physical Properties and the Boundedness of CO-emitting Structures, ApJ **932**(1): 47.

Wright, N. J., Bouy, H., Drew, J. E., Sarro, L. M., Bertin, E., Cuillandre, J.-C. and Barrado, D. (2016). Cygnus OB2 DANCe: A high-precision proper motion study of the Cygnus OB2 association, MNRAS **460**(3): 2593–2610.

Wright, N. J., Jeffries, R. D., Jackson, R. J., Bayo, A., Bonito, R., Damiani, F., Kalari, V., Lanzafame, A. C., Pancino, E., Parker, R. J., Prisinzano, L., Randich, S., Vink, J. S., Alfaro, E. J., Bergemann, M., Franciosini, E., Gilmore, G., Gonneau, A., Hourihane, A., Jofré, P., Koposov, S. E., Lewis, J., Magrini, L., Micela, G., Morbidelli, L., Sacco, G. G., Worley, C. C. and Zaggia, S. (2019). The Gaia-ESO Survey: asymmetric expansion of the Lagoon Nebula cluster NGC 6530 from GES and Gaia DR2, MNRAS **486**(2): 2477–2493.

Wright, N. J., Jeffries, R. D., Jackson, R. J., Sacco, G. G., Arnold, B., Franciosini, E., Gilmore, G., Gonneau, A., Morbidelli, L., Prisinzano, L., Randich, S. and Worley, C. C. (2024). The Gaia-ESO Survey: 3D dynamics of young groups and clusters from GES and Gaia EDR3, MNRAS **533**(1): 705–728.

Wright, N. J. and Mamajek, E. E. (2018). The kinematics of the Scorpius-Centaurus OB association from Gaia DR1, MNRAS **476**(1): 381–398.

Zhang, G.-Y., André, P., Men'shchikov, A. and Li, J.-Z. (2024). Probing the filamentary nature of star formation in the California giant molecular cloud, A&A **689**: A3.

Chapter 2

Gas Accretion Onto Star Clusters

The content of this chapter is a second revision of the manuscript text for publication under the following citation:

Karam, J. & Sills, A. (2023). Modelling Star Cluster Formation: Gas Accretion. The Monthly Notices of the Royal Astronomical Society, 521, 5557-5569

Modelling Star Cluster Formation: Gas Accretion

Jeremy Karam
Department of Physics and Astronomy
McMaster University, Hamilton, ON, Canada
Email: karamj2@mcmaster.ca

Alison Sills
Department of Physics and Astronomy
McMaster University, Hamilton, ON, Canada
Email: asills@mcmaster.ca

Abstract

The formation of star clusters involves the growth of smaller, gas-rich subclusters through accretion of gas from the giant molecular cloud within which the subclusters are embedded. The two main accretion mechanisms responsible for this are accretion of gas from dense filaments, and from the ambient background of the cloud. We perform simulations of both of these accretion processes onto gas-rich star clusters using coupled smoothed particle hydrodynamics to model the gas, and N-body dynamics to model the stars. We find that, for both accretion processes, the accreting star cluster loses some of its original mass while gaining mass from either the ambient background or the dense filament. The amount of mass lost from both these processes is small compared to the total mass of the cluster. However, in the case of accretion from a background medium, the net effect can be a decrease in the total mass of the cluster if it is travelling fast enough through the ambient medium ($> 4\text{kms}^{-1}$). We find that the amount of mass lost from the cluster through filamentary accretion is independent of the density, width, or number of filaments funneling gas into the cluster and is always such that the mass of the cluster is constantly increasing with time. We compare our results to idealized prescriptions used to model star cluster formation in larger scale GMC simulations and find that such prescriptions act as an upper limit when describing the mass of the star cluster they represent.

Keywords: *star clusters: general – stars: kinematics and dynamics – stars: formation*

2.1 Introduction

Star forming regions throughout galaxies are found to comprise of dense molecular gas which can collapse to form stars. These stars form in clustered groups that can contain many stars gravitationally bound to one another (called star clusters). Such clusters are embedded inside these giant molecular clouds (GMCs) in their early stages of evolution (Lada and Lada 2003). This embedded phase of the star clusters life tends to last only a few Myr after which, the cluster is able to remove surrounding gas through stellar feedback effects (Li et al. 2019, Pelupessy and Portegies Zwart 2012). Interactions between the embedded star cluster and the surrounding molecular gas in this time can have an effect on the overall evolution of the star cluster.

Because of turbulence, the distribution of the gas surrounding star clusters in GMCs can be very complicated. For example, observations performed by the Herschel telescope find that such star forming clouds are filled with filamentary structure (see André et al. 2014 and references therein). Furthermore, these filaments do not exist on their own, but are often found in hub systems, which contain many groups of filaments, that can surround young clusters or young stellar objects (YSOs) (e.g Peretto et al. 2014, Fukui et al. 2019, Kumar et al. 2022, Bhadari et al. 2022, Wong et al. 2022). As these filaments evolve, they develop dense cores (e.g. Men'shchikov et al. 2010, Arzoumanian et al. 2011) within which stars and star clusters can form. The remaining filamentary gas can then be accreted onto the cluster (e.g Kirk et al. 2013).

The sizes of these star clusters can vary, but numerical simulations of GMC evolution have shown that smaller star clusters (subclusters) can evolve into more massive ones with. Two important mechanisms for this growth are subcluster mergers, and accretion of the background gas in which the cluster is embedded (Howard et al. 2018 hereafter H18). We focus on the latter in this work and point the reader to Karam and Sills (2022) (hereafter Paper I) for a study of subcluster mergers.

Simulating star formation inside GMCs is computationally challenging because of the small timesteps required to properly model the high density gas. Therefore, in order to model star cluster formation and evolution alongside the rest of the GMC, a sink particle prescription is often used. A commonly used prescription is that described in Federrath et al. (2010), which was used in H18. This approach models a subcluster of gas and

stars as a sink with parameters that describe its overall behaviour (i.e. the total mass, position, and velocity) rather than resolving the cluster as a collection of individual stars and gas. Though sink particles drastically reduce computation time, a caveat to their use is that the internal evolution of the stars and gas that make up the star cluster is unknown. For example, in Paper I, we found that the sink particle prescription does not provide the full picture regarding subcluster mergers present in H18. We found that the merger of two clusters unbinds a fraction of the stars and gas from both clusters involved. Because sink particles do not account for this detail, we concluded that they could be overestimating the total mass of a system which is the result of a cluster merger (Karam and Sills 2022).

While simulations have been performed to study gas accretion processes onto clusters in more detail, they come with their own set of limitations. For example, simulations performed by Naiman et al. (2011) have considered the star cluster as an analytic potential allowed to move through an initially uniform distribution of background gas. This method is similar to a sink particle approach in that it does not allow one to learn how the individual components of the star cluster (stars and gas) react to gas accretion. Others such as Kaaz et al. (2019) have only considered clusters with up to $N = 32$ equal mass stars to understand accretion onto individual stellar members. This is not representative of true star clusters which can contain many more stars of varying mass.

In order to explore the effects of gas accretion on young star clusters in more detail, we model clusters at a higher resolution containing both stars and gas, and allow these components to gravitationally interact with one another. We then allow our cluster to interact with surrounding gas that would be present in a GMC. We consider accretion from ambient gas as the cluster moves through the GMC and from filaments that funnel gas towards the cluster. We analyze the cluster as it reacts to these processes to better understand how both the stellar and gas components evolve due to gas accretion inside GMCs and to use this understanding to inform large scale GMC simulations which use sink particle prescriptions to model star clusters.

In section 2.2 we discuss the initial conditions used for both our stream and filament simulations. In section 2.3, we look at the response of the cluster to accretion from a ambient background media of different densities, and accretion from one, two and three filaments. Finally, in section 2.4, we compare our results to observations to further understand star formation, and discuss how they can inform current implementations of the sink particle prescription.

Cluster Name	M_{star} [$10^4 M_\odot$]	M_{gas} [$10^4 M_\odot$]	r_{hm} [pc]
C1	0.06	0.3	0.4
C2	0.3	0.3	0.6

TABLE 2.1: Parameters of the central clusters used in this work. Column 1: the name of the cluster, column 2: the total stellar mass of the cluster, column 3: the total gas mass of the cluster, column 4: the half mass radius of the cluster. Any simulation name from table 2.3 that does not have _C2 after it, is using C1 as the central cluster.

Run Name	Ambient Background Density [$M_\odot pc^{-3}$]	Background Medium Velocity [kms^{-1}]
CtS005	0.05	4
CtS05	0.5	4
CtS1	1	4
CtS005_6v	0.05	6
CtS05_6v	0.5	6
CtS1_6v	1	6
CtS005_10v	0.05	10
CtS05_10v	0.5	10
CtS1_10v	1	10

TABLE 2.2: Parameters for our simulations of a star cluster moving through an ambient background medium. Column 1: the name of the simulation, column 2: the density of the ambient background medium ($1 M_\odot pc^{-3} = 7\times10^{-23} gcm^{-3} \approx 17 cm^{-3}$), column 3: the velocity of the ambient background medium. All of these simulations use C1 as the central cluster (see table 2.1).

Run Name	Ambient Background Density [$M_\odot pc^{-3}$]	Filament Density [$M_\odot pc^{-3}$]	Filament Width [pc]	Number of Filaments
FwC1250	-	1250	0.3	1
FwC850	-	850	0.3	1
FwC600	-	600	0.3	1
FwC310	-	310	0.6	1
2FwC1250	-	(1250,1250)	0.3	2
2FwC850	-	(850,850)	0.3	2
2FwC600	-	(600,600)	0.3	2
2FwC310	-	(310,310)	0.6	2
FCS1250_1	1	1250	0.3	1
FCS1250_05	0.5	1250	0.3	1
2FCS1250_1	1	(1250,1250)	0.3	2
2FCS1250_05	0.5	(1250,1250)	0.3	2
FwC1250_C2	-	1250	0.3	1
FwC850_C2	-	850	0.3	1
FwC600_C2	-	600	0.3	1
FwC310_C2	-	310	0.6	1
2FwC1250_C2	-	(1250,1250)	0.3	2
2FwC850_C2	-	(850,850)	0.3	2
2FwC600_C2	-	(600,600)	0.3	2
2FwC310_C2	-	(310,310)	0.6	2
SDC	-	(850,600,600)	0.3	3

TABLE 2.3: Parameters for our simulations of accretion from filaments onto a central star cluster. Column 1: the name of the simulation, column2: the density of the ambient medium, column 3: the density of the filament(s), column 4: the filament width, column 5: the number of filaments present in the simulation.

2.2 Methods

In the following sections, we discuss the computational methods used in our simulations. We also discuss the initial conditions of our two different simulation setups: a star cluster accreting gas from movement through a background medium, and a star cluster accreting gas from a dense filament.

2.2.1 Numerical Methods

Our simulations are performed using the Astrophysical Multipurpose Software Environment (AMUSE) (Portegies Zwart et al. 2009, Pelupessy and Portegies Zwart 2012) which contains codes that evolve the equations of gravity and hydrodynamics. AMUSE also allows for communication between these codes. This allows us to simulate the dynamics of the stars and hydrodynamics of the gas simultaneously in the cluster and focus on how they interact with one another.

We use `hermite0` (Makino and Aarseth 1992) for our N-Body code and for our smoothed particle hydrodynamics (SPH) code we use `GADGET-2` (Springel 2005). For the communication scheme, we use `BRIDGE` (Fujii et al. 2007) with `BHTree` (written by

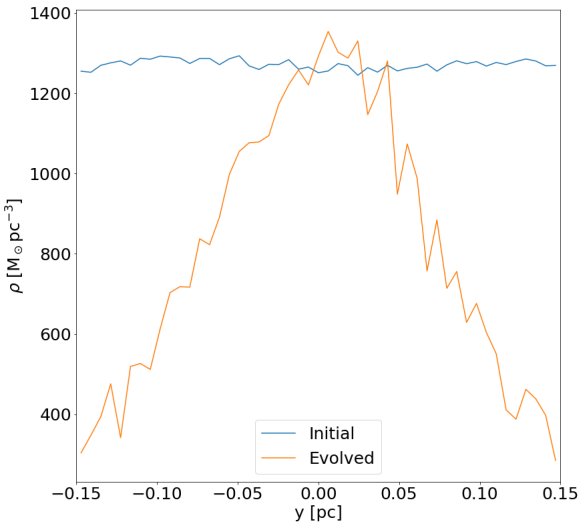

FIGURE 2.1: An example of filament density as a function of position across the y-axis of filament. We set up the filament with a constant density of $\rho = 1250 \mathrm{M}_\odot \mathrm{pc}^{-3}$ (blue line) and let it relax to a density profile given by the orange line after interaction with a point mass.

Jun Makino based on Barnes and Hut 1986) as the connecting algorithm. We describe our numerical scheme in more detail in Paper I.

We set up our star clusters using Plummer (Plummer 1911) spheres of stars and gas that we numerically relax. We assign the masses to the stars by sampling a Kroupa (Kroupa 2001) IMF from $0.15M_{\odot}$ to $100M_{\odot}$. For the gas, we give our SPH gas particles a mass of $M_{SPH} = 0.06M_{\odot}$ and set the gas temperature to $T = 10$K. We sample the velocities of the stars and gas using the method outlined in Aarseth (1974) and scale them to ensure that our clusters are initially in virial equilibrium ($2K_{s,g}/|P_{s,g}| = 1$ where $K_{s,g}$ is the kinetic energy of the stars or gas, and $P_{s,g}$ is the potential energy of the stars or gas).

We ensure that the size of our cluster is such that the density at its half mass radius is consistent with young massive cluster observations as shown in Portegies Zwart et al. (2010) ($\rho_{hm} \approx 10^3$-$10^4 M_{\odot}pc^{-3}$). We show the parameters that describe the clusters used in this work in table 2.1. For more information regarding our set up of the star cluster, see Paper I.

2.2.2 Cluster Moving Through a Uniform Background

We begin with describing our simulations of the motion of a cluster through an ambient medium of background gas. We place the cluster at the centre of the simulation box and set up a cube of constant density gas distributed in a glass configuration (White 1994). We give the background gas a velocity towards the cluster, thus placing our reference frame on the cluster as it moves through an ambient medium. We choose this velocity to be $v_{\rm inj} = 4 {\rm kms}^{-1}$ which is consistent with velocity dispersion values used in GMC evolution simulations (e.g. Guszejnov et al. 2022). We also study the effects of increasing this velocity to 6 and 10 $\rm kms^{-1}$, the former being the average collision velocity of subcluster mergers in H18 and the latter being the velocity limit beyond which we found that cluster collisions may not result in a single merged cluster (see Paper I). As the background gas moves through the simulation box, we continuously inject material of the same density on the left side of the box so that we can study the cluster for longer times.

The size of the ambient background gas (and the simulation box) is 15x15x15pc. Because the cluster has a radius of $\approx$ 2pc, this box size is sufficient to include all the original cluster material. Any gas or star particle that moves outside the boundaries of our simulation box is removed from the simulation. To study the response of our isolated cluster in varying environments throughout a GMC, we consider three different

density values for our background gas: $\rho = 0.05, 0.5$ and $1 \mathrm{M}_{\odot}\mathrm{pc}^{-3}$. This covers the low density regime used in previous works (e.g. Calura et al. 2019) and the average densities observed in GMC catalogues from Rosolowsky et al. (2021). We show the parameters for all of our simulations of a cluster moving through an ambient background medium in table 2.2. Higher density regions throughout the GMC will likely be in the form of filaments which we cover in the next subsection.

2.2.3 Filaments

The equilibrium state of a filamentary (thin and elongated) gas distribution is heavily dependant on the line mass ($M_{\rm line}$) of that distribution, defined as the mass per unit distance across the distribution (Inutsuka and Miyama 1997, Inutsuka and Miyama 1992). Inutsuka and Miyama (1997) show that filaments whose $M_{\rm line}$ exceeds a critical value given by $M^{\rm c}_{\rm line} = 2c_s^2/G$ where c_s is the thermal sound speed can collapse into dense, spherical cores. As well, Fischera and Martin (2012) show that filaments require sufficient external pressure to survive if their $M_{\rm line} < M^{\rm c}_{\rm line}$. We define a ratio of the line mass of a filament to the critical line mass as $f_{\rm fil} = M_{\rm line}/M^{c}_{\rm line}$. With this definition, $f_{\rm fil} > 1$ corresponds to filaments which will collapse under their own self-gravity, and $f_{\rm fil} < 1$ corresponds to filaments which require external pressure to remain stable.

We initially set up our filament as a thin, elongated distribution of SPH particles with uniform density ρ_0 and a width w. To give our filament a density distribution that more accurately resembles observations by Arzoumanian et al. (2011) and theoretical models of cylindrical equilibrium states presented in Ostriker (1964), we give our initial distribution a velocity ($v_{\rm fil}$) towards a point mass and let it evolve. An example of the change in our filament density profile can be seen in figure 2.1 for a filament whose long axis is situated along the x-axis. In this example, we use the distribution given by the orange line as our filament that will accrete onto our central cluster. We take this filament and place it along the $y = 0$ axis with the cluster situated at the center of our simulation box. As the filament travels towards the cluster, we continue to inject material from the edge of the filament to ensure that matter is continuously flowing.

We select filament densities and widths that are consistent with observations of star forming regions within the Milky Way, namely, the SDC13 (Peretto et al. 2014), and IC5146 (Arzoumanian et al. 2011) regions. These values have a direct effect on the line mass of our filaments because $M_{\rm line} = \rho_0 \pi w^2$. Therefore, we distinguish between our filaments using $f_{\rm fil}$ throughout the rest of this paper. We give our filaments a velocity of

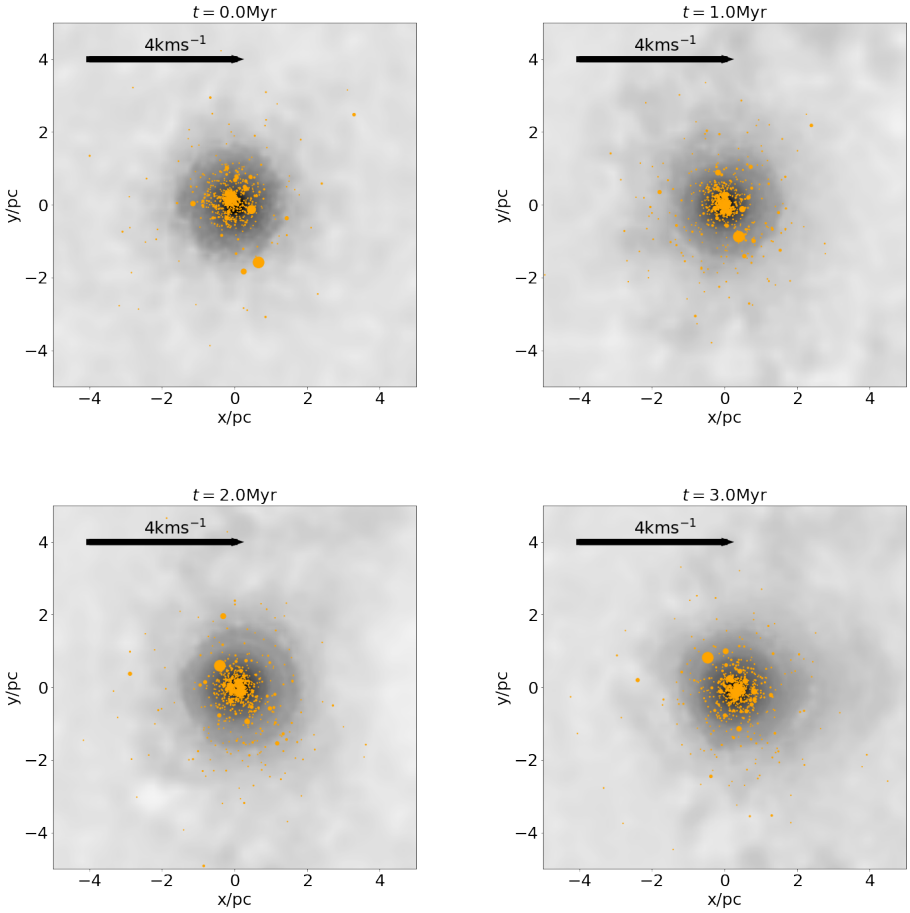

FIGURE 2.2: Snapshots of the stars and gas from ambient background gas accretion run CtS1. The orange circles represent the stars from the cluster with their size scaled to the mass of the star. Gas is shown in greyscale with darker regions showing higher density gas (minimum corresponds to $\rho = 0.1 M_{\odot} pc^{-3}$ and maximum corresponds to $\rho = 10^{4} M_{\odot} pc^{-3}$). The black arrow in the top left shows the velocity of the ambient background gas.

$v_{\rm fil} = 2{\rm kms}^{-1}$ which is consistent with simulations preformed by Gómez and Vázquez-Semadeni (2014). We show the parameters for these simulations in table 2.3.

Observations of filamentary regions give us a wide array of possible filament configurations that often include accretion onto a cluster from more than one filament. We therefore simulate this accretion from 1, 2 and 3 of our filaments with the orientation of our 3 filament simulation matching observations of SDC13 (Peretto et al. 2014, Wang et al. 2022).

2.3 Cluster Evolution

In this section, we first discuss how our cluster is affected by movement through diffuse background gas. We then focus on how filamentary gas accretion impacts the cluster.

2.3.1 Ambient Background Gas

We begin with a discussion of the evolution of our star cluster as it moves through ambient background gas with different velocities and different ambient background gas densities. These correspond to the simulations from table 2.2. We show snapshots of one of these simulations in figure 2.2. Here, our ambient background gas has a density of $\rho_{BG} = 1{\rm M}_\odot{\rm pc}^{-3}$ and is travelling with positive velocity of $4{\rm kms}^{-1}$ along the x direction towards the cluster initiated at the centre of the simulation box. The cluster has a stellar mass of $M_s \approx 0.06 \times 10^4{\rm M}_\odot$ and the gas mass is $M_g \approx 0.3 \times 10^4{\rm M}_\odot$.

We find that the stellar component of the cluster is mostly unaffected by this evolutionary process regardless of ambient background gas density, or velocity. The gas is affected however. As the diffuse background gas pushes past the cluster, it starts to interact with the gas component of the cluster. At later times, we can start to see some of the gas being pushed away from the cluster (this can be seen as the dense gas directly to the right of the cluster in the bottom right snapshot of figure 2.2). This modifies the spherical symmetry that was present in the gas component of the cluster. Along with this loss of gas, the potential from the cluster leads to accretion of background gas implying that the total mass of the cluster is changing constantly throughout the simulation.

2.3.1.1 Bound Cluster Material

We begin our analysis of these simulations by looking at the bound cluster material. This helps us better understand how the mass of the cluster is changing as a result of

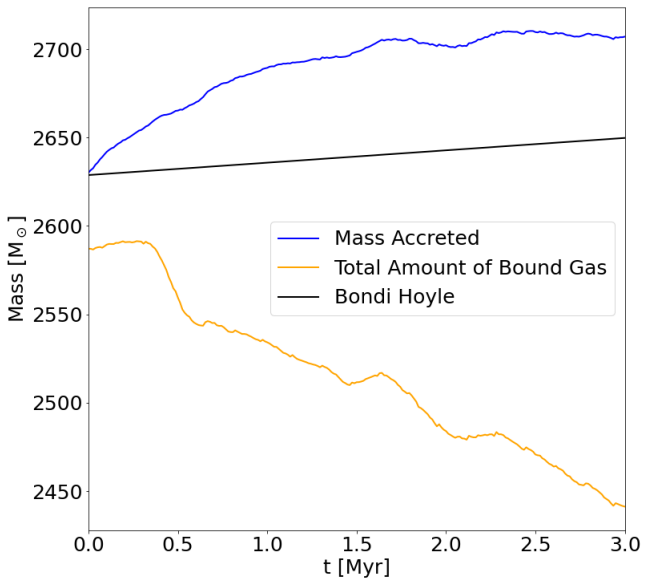

FIGURE 2.3: Total gas mass calculated assuming only accretion (blue line), using Bondi-Hoyle accretion formalism (black line), and using total bound mass of cluster (orange line) of a cluster moving through an ambient medium with a density of $\rho_{\rm BG} = 0.5 {\rm M}_\odot {\rm pc}^{-3}$ and at a velocity of $6 {\rm kms}^{-1}$.

interactions with the background medium. The total cluster mass can change through two ways: accretion of the diffuse background gas onto the cluster, or loss of some of the initially bound cluster mass (stars or gas). To determine the boundedness of any particle in our simulation, we calculate the potential energy (U) felt on a given particle (star or gas) from every other particle in the simulation (stars and gas). We then compare that to the kinetic energy of that particle (T) calculated with respect to the centre of mass of the cluster. Finally, if $T + U < 0$ for a given particle, we consider that particle bound to the cluster. If not, it is unbound.

We find that the boundedness of the stellar component of the cluster remains roughly unchanged for the entire 3Myr in every simulation in table 2.2. Each simulation loses $\approx$ 1.5 to $2 {\rm M}_\odot$ of stellar material through unbinding by the end of the simulation which is negligible compared to the total mass of the cluster.

To analyze the gas component, we first calculate the total mass gained by our cluster from the ambient background. We then compare that to the increase in mass of the

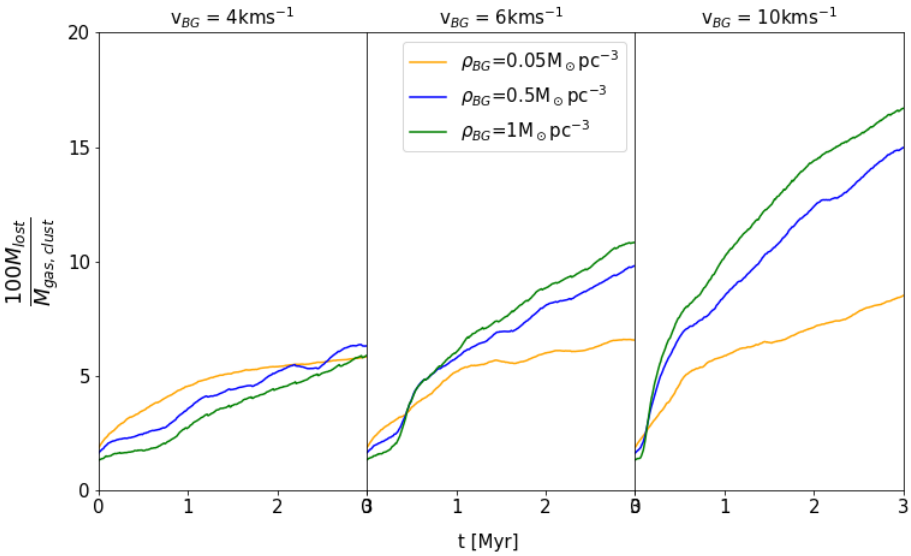

FIGURE 2.4: Percent of total initial cluster gas mass that becomes unbound throughout the simulation. Gas that is accreted onto the cluster from the background is not included. The left, middle, and right panels show the simulations of a cluster travelling through an ambient background in which the cluster velocity is 4, 6, and 10kms^{-1} respectively. The colours correspond to the density of the ambient background.

cluster calculated using the Bondi-Hoyle accretion formalism (Bondi 1952, Shima et al. 1985) which presents a theoretical accretion rate for a point mass travelling through an ambient medium. An example of these values for the simulation of a cluster moving through an ambient medium with density $\rho_{\rm BG} = 0.5{\rm M}_\odot{\rm pc}^{-3}$ and velocity 6kms^{-1} can be seen as the blue and black lines respectively in figure 2.3. We see that using the Bondi-Hoyle formalism underestimates the total mass gained by the cluster likely because our cluster is not a point mass. Varying potential distributions have been shown to have an effect on the Bondi-Hoyle accretion formalism (Naiman et al. 2011). We find the same discrepancy for all of our simulations of a cluster moving through an ambient medium implying that Bondi-Hoyle accretion may not be sufficient in describing the amount of mass gained by a cluster as it travels through an ambient medium.

We now compare the total mass accreted onto the cluster to the total bound gas mass of the cluster which considers both accretion from the background medium, and loss of cluster gas through unbinding. We show this total bound gas mass as the orange line

in figure 2.3 for the simulation with $\rho_{\rm BG} = 0.5 {\rm M}_{\odot} {\rm pc}^{-3}$ and $v_{\rm inj} = 6 {\rm kms}^{-1}$. From this plot, we see that the total bound cluster gas mass is decreasing with time. This occurs for all of our simulations with a cluster velocity above $4 {\rm kms}^{-1}$. However, the amount of mass removed from the cluster throughout this interaction is small compared to the total mass of the cluster. We calculate $M_{\rm lost}/M_{\rm gas,clust}$ where $M_{\rm lost}$ is the total mass of gas that is lost from the cluster, and $M_{\rm gas,clust}$ is the total cluster gas mass, for this simulation. Here, $M_{\rm gas,clust}$ includes all the gas that originally belonged to the cluster (column 3 in table 2.1) and gas mass from the background medium that has become bound to the cluster. We find that only ≈ 5 percent of the cluster gas mass is stripped off of the cluster from its interaction with the background medium. We perform this comparison for all of our simulations of a cluster moving through an ambient medium and show our results in figure 2.4.

When the background velocity is low, all simulations result in the cluster losing ≈ 5 per cent of its total gas mass. As we increase the velocity, the background gas density begins to play more of an important role. In the middle panel, we see that the simulation with the highest background density leads to the highest fraction of gas mass lost for that given velocity. This persists when the background velocity is $10 {\rm kms}^{-1}$. As well, increasing the velocity increases the rate at which the cluster is losing mass which leads to the cluster losing more mass than it gains in the simulations with $v_{\rm BG} > 4 {\rm kms}^{-1}$. However, in all these panels, the amount of gas mass lost remains small compared to the total mass of the cluster. Therefore, we conclude that movement through a background medium can result in a net decrease in the total mass of a cluster, but that decrease is small compared to the total mass of the cluster.

This analysis also helps us learn more about the accuracy of the sink particle prescription as it would apply to our simulations. Because sink particles do not allow for material to be removed from a sink after the sink has accreted it, our simulations show that they can be overestimating the total mass of the cluster they represent. However, because the amount of mass lost from the cluster is small compared to the total mass of the cluster, this overestimation would only be by a small fraction (< 20 per cent).

2.3.1.2 Star Forming Gas

Sink particles in the H18 simulations convert gas into stars with a constant efficiency of 20 per cent every free fall time. While our simulations do not include a star formation prescription, we can trace the amount of dense gas present to understand what effect movement through a background medium would have on the star formation efficiency of

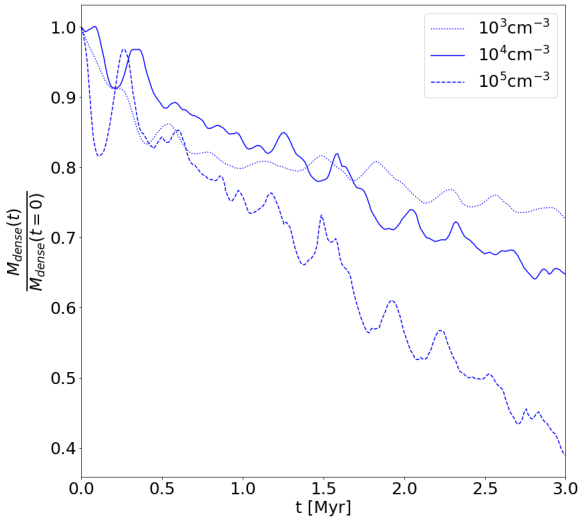

FIGURE 2.5: Mass of gas above a given threshold density normalized by that value at the beginning of the simulation for the simulation of a cluster moving through an ambient medium with density $\rho_{\rm BG} = 0.5{\rm M}_\odot{\rm pc}^{-3}$ and a velocity of $4{\rm kms}^{-1}$. The dotted, solid and dashed lines correspond to density thresholds of 10^3, 10^4, and $10^5{\rm cm}^{-3}$ respectively.

our clusters. We consider gas with densities above 10^4 and $10^5{\rm cm}^{-3}$ which are quoted density ranges above which stars begin to form (e.g Evans et al. 2009, Heiderman et al. 2010, Lada et al. 2010, Lada et al. 2012). As well, the former is the threshold density above which sinks are formed in the H18 simulations. We also consider gas above $10^3{\rm cm}^{-3}$ as this has been used as sink particle formation thresholds in previous, larger scale simulations as well (e.g. Dobbs et al. 2022).

We find that our cluster loses $\approx$ 30 per cent of its mass of gas above $10^4{\rm cm}^{-3}$ by the end of the simulation regardless of the density of the ambient background gas. An example of this can be seen as the solid line in figure 2.5 for the simulation with a background density of $\rho_{\rm BG} = 0.5{\rm M}_\odot{\rm pc}^{-3}$ and gas velocity of $4{\rm kms}^{-1}$. This consistency rises from the fact that, as the cluster moves through the diffuse medium, the outer layers are those that are most perturbed while the cluster core remains mostly unperturbed due to its higher potential. We find the same slow decrease when looking at the total mass of gas with densities above the other two thresholds regardless of the background density. The difference is that we see a decrease of $\approx$ 25 and $\approx$ 50 per cent by the ends

of the simulations for gas with densities above 10^3 and $10^5 \mathrm{cm}^{-3}$ respectively. As well, we find that these trends do not change when we change the density of the ambient background gas.

We find that the velocity of the ambient medium has no affect on the dense gas present at any time for any of the threshold densities we considered. Increasing the velocity leads to an increase in gas which becomes unbound from the cluster, and this gas is mostly located in the outer regions of the cluster meaning the dense core remains mostly unaffected.

Therefore, we find that, for the values we considered, the density of the ambient background, and the velocity of the cluster travelling through a uniform density ambient background do not play a role in determining the amount of dense gas present in the cluster. In our simulations, we would see less star formation over time as the cluster travels through the ambient medium. This may change when a more realistic background density distribution is considered. We discuss this more in section 2.4.

2.3.2 Single Filaments

We now move on to a discussion of the accretion from a single filament onto our smaller star cluster. These correspond to the simulations FwC1250, FwC850, FwC600, and FwC310 in table 2.3. These simulations provide us with a baseline to which we can compare our simulations of multiple filament systems. Each of these four simulations have different filament densities $\rho_0 = 1250, 850, 600$, and $310 \mathrm{M}_\odot \mathrm{pc}^{-3}$ with filament widths $w = 0.3, 0.3, 0.3$, and 0.6pc respectively. These correspond to $f_{\mathrm{fil}} = 4.7, 3.2, 2.3$, and 4.7. The density and width of the last of these simulations was chosen such that its f_{fil} is the same as the first. This helps us understand whether the line mass (or accretion rate $M_{\mathrm{line}} v_{\mathrm{fil}}$) of a filament is sufficient in predicting the effect it has on an accreting cluster. The cluster is the same as that from section 2.3.1. We show snapshots of the simulation with the higher density filament ($\rho = 1250 \mathrm{M}_\odot \mathrm{pc}^{-3}$) in figure 2.6. The gas density is illustrated by the grey scale with a minimum of $10 \mathrm{M}_\odot \mathrm{pc}^{-3}$ and a maximum of $10^4 \mathrm{M}_\odot \mathrm{pc}^{-3}$. The orange circles represent the stars in the cluster and their size is scaled with the mass of the star.

At $t = 0$Myr, the filament of gas is seen on the left side of the cluster with a velocity towards the cluster centre. As the filament impacts the core of the cluster, the gas density in the inner region of the cluster starts to decrease. By the end of the simulation, the cluster core has become so diffuse that gas coming from the filament pushes through the cluster and comes out the other side (see dense region on right hand side of cluster in

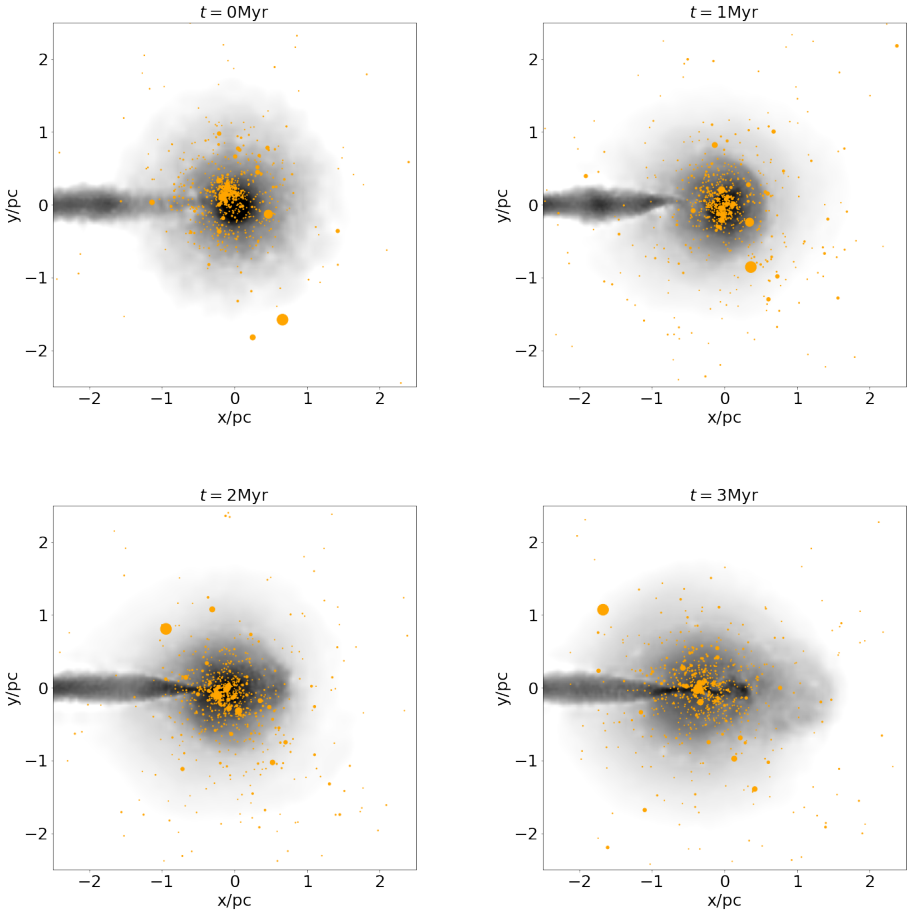

FIGURE 2.6: Snapshots of the stars and gas from filamentary accretion run FwC1250. The orange circles represent the stars from the cluster with their size scaled to the mass of the star. Gas is shown in greyscale with darker regions showing higher density gas. The minimum density shown is $10 M_{\odot} pc^{3}$ and the maximum density shown is $10^{4} M_{\odot} pc^{-3}$.

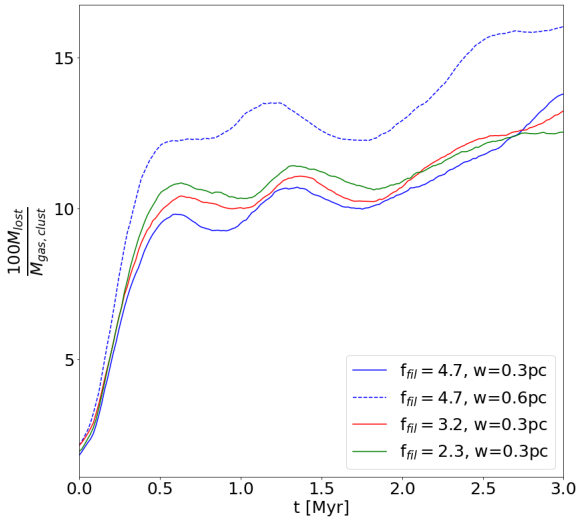

FIGURE 2.7: Percent of total cluster gas mass that is unbound throughout the simulation for all simulations of a single filament impacting our smaller cluster. Colour describes $f_{\rm fil} \propto \rho w^2$ of the filament in a given simulation and the dashed line denotes a larger filament width.

bottom right panel of figure 2.6). We see similar behaviour for all four of these single filament simulations. Energy from the impact of the filament onto the cluster causes the gas component to expand.

The stellar component responds to this accretion by expanding slightly because of the expansion of the gas component. The stellar component core radius grows by a factor of 2 for the three simulations whose filaments have a width of 0.3pc and grows by a factor 3 for the simulation whose filament width is 0.6pc.

2.3.2.1 Bound Material

First, we analyze how gas accretion from a single filament affects the total mass of the cluster by looking at the bound mass of the stellar and gas components of our cluster as it accretes gas from the filament.

We find that the boundedness of the stellar component of the cluster for these four single filament simulations is not very affected by the filamentary accretion. Throughout

the entire simulation, less than $2M_{\odot}$ of stellar mass become unbound from the cluster for each simulation similar to the simulations discussed in section 2.3.1.1.

Conversely, the total mass of the gas component of the cluster is strongly affected. The cluster is constantly gaining gas mass from interactions with the flowing filament. We find that $\approx$ 90 percent of the total mass of the filament is bound to the cluster for all four of these simulations. We also find that accretion from a filament causes a fraction of the gas originally belonging to the cluster to become unbound. To understand the effect this has on the total cluster gas mass, we calculate the fraction of the total cluster gas mass that is unbound from the cluster as a function of time. We show this as a percentage for these four single filament simulations in figure 2.7. From this plot, we see that the amount of gas mass which becomes unbound from the cluster is small compared to the total mass of the cluster. Therefore, the net effect of accretion from a filament is an increase in the mass of the cluster. Furthermore, this trend is similar for all simulations with a smaller filament width regardless of the density we considered. While a larger filament width results in more gas mass becoming unbound from the cluster, the amount remains small compared to the total mass of the cluster.

We conclude that our cluster loses a small fraction of its mass from filamentary accretion, and that this fraction is similar for all filament widths and densities considered. This result has implications for the sink particle prescription as well. Because sinks do not allow for the loss of material, and we find that this loss is small compared to the total mass of the cluster, we can conclude that sink particles are only slightly overestimating the total mass of the cluster they represent when considering accretion from a single filament.

2.3.2.2 Star Forming Gas

We now track the total mass of dense gas in these simulations to help us understand how accretion from a single filament affects star formation inside the central cluster.

We find that the total mass of gas with densities above $10^4 \mathrm{cm}^{-3}$ slowly decreases as the the cluster is impacted by the filament for each of these four simulations. By the end of the simulation, this decrease is only by $\approx$ 40 per cent for the simulations whose filaments have a width of 0.3pc. Conversely, the simulation with a filament of width 0.6pc sees a much more drastic decrease in dense gas mass, namely, by around 80 per cent by the end of the simulation. This trend persists when looking at densities above $10^5 \mathrm{cm}^{-3}$ as well. However, in this case, the total mass of dense gas decreases by $>$ 90 per cent for all four of these simulations by the end of the simulation. Lastly, we find that

the mass of gas above $10^3 cm^{-3}$ plateaus for the simulations which contains filaments of width 0.3pc and have densities of 1250 and $850 M_\odot pc^{-3}$. The remaining two simulations see consistent decrease in gas above $10^3 cm^{-3}$ with time.

Therefore, for our single filament simulations, we find that the total mass of potentially star forming dense gas present as the simulation evolves is not dependent on the line mass of the filament that is impacting the cluster. It is better to consider the density and width of the filament separately. We also conclude that the amount of potentially star forming gas in these simulations can either remain constant or decrease depending on the threshold chosen above which star formation is allowed. We do not see any net increase in the amount of potentially star forming gas in these single filament simulations.

2.3.3 Double Filaments

We now turn our discussion towards the simulations in our suite of accretion of gas from two parallel filaments onto our smaller star cluster. These simulations are more representative of the real universe than those performed using a single filament. This is a consequence of the formation mechanism of prestellar cores which sees them forming within dense filaments, and not on the edges (André 2017). These correspond to simulations 2FwC1250, 2FwC850, 2FwC600, and 2FwC310 in table 2.3. The densities and width of these filaments are the same as those from our single filament simulations discussed in section 2.3.2, but we have doubled the single filament and mirrored it on the other side of the cluster. As well, the central star cluster is the same as in our single filament simulations. Snapshots from the double filament simulation with filaments of density $1250 M_\odot pc^3$ and width 0.3pc can be seen in figure 2.8.

We see that impact onto the cluster from filamentary gas leads to expansion of the clusters gas component. In these simulations, the mass of new dense gas accreted onto the cluster core from the two filaments is sufficient enough to prevent the expansion of the stellar component found in the single filament simulations.

2.3.3.1 Bound Material

We first look at the amount of material that is bound to the cluster as it accretes filamentary gas in these double filament simulations. Similarly to the single filament simulations, a negligible amount of stellar mass is unbound from the cluster in all of these simulations ($\approx 2 M_\odot$ at most).

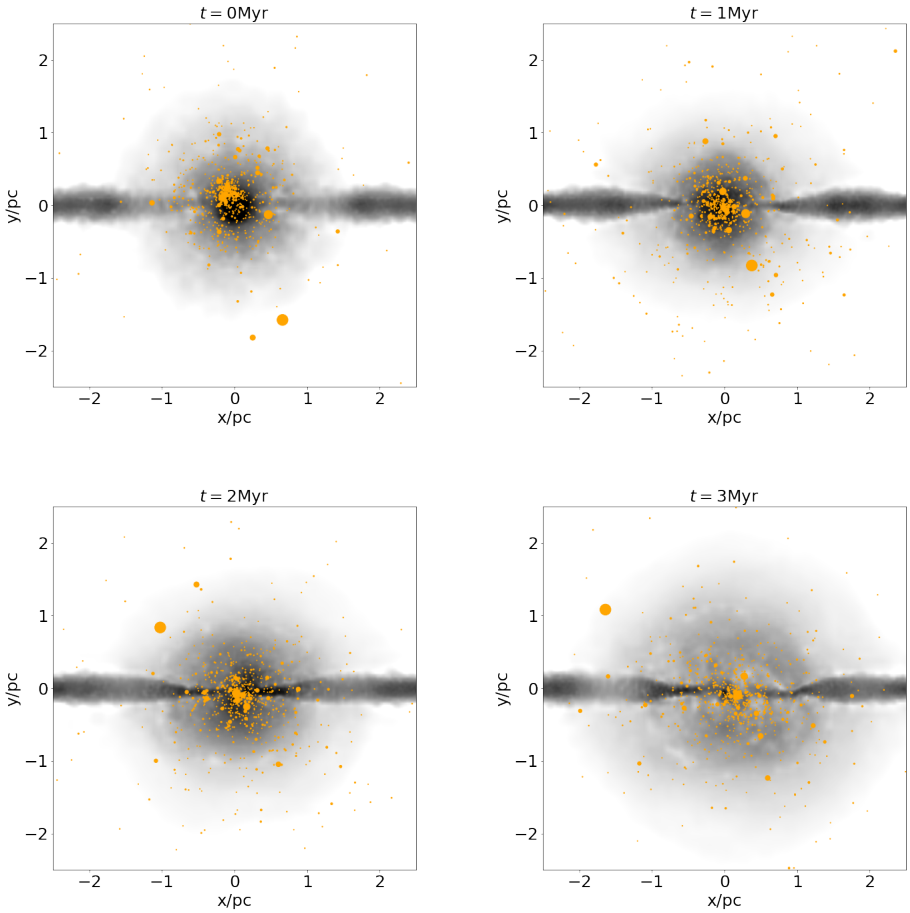

FIGURE 2.8: Same as figure 2.6 but for the simulation 2FwC1250.

However, the total mass of the gas component of the cluster increases more in the double filament simulations than in the single filament simulations, as expected. The increase in the gas mass of a cluster accreting from two filaments of a given density is roughly twice that of cluster accreting from one filament of the same width and density. The mass of gas removed from the cluster, however, does not scale this way. We find that roughly the same amount of mass is removed from the cluster in these simulations as those of accretion from a single filament. As a consequence of this, the fraction of the total cluster gas mass that becomes unbound is slightly less for these simulations than those from figure 2.7, but not substantially. We find that this percentage lies in the same range as those in figure 2.7. As well, in these double filament simulations, there is no substantial difference between the fraction of mass that becomes unbound for different filament parameters, similar to section 2.3.2.1.

This result also shows that the magnitude of the overestimation made by the sink particle prescription in calculating the total gas mass of the cluster is roughly equal between accretion from one or two filaments in our suite. We discuss the implications of this further in section 2.4.

2.3.3.2 Star Forming Gas

Similar to section 2.3.2.2, we analyze the total mass of dense gas above 10^3, 10^4 and $10^5 \mathrm{cm}^{-3}$ in our double filament simulations. We show the total mass in gas with densities above the $10^4 \mathrm{cm}^{-3}$ threshold for these four double filament simulations in figure 2.9. Our simulations involving the two densest filaments (blue and green line in figure 2.9) contain a roughly constant amount of mass above $10^4 \mathrm{cm}^{-3}$ for $\approx$ 1.5Myr. This is in contrast to the simulations containing a single filament where we saw steady decrease in gas above $10^4 \mathrm{cm}^{-3}$ regardless of filament parameters. The second filament can act as another source of dense gas to help prevent the gas core of the cluster from becoming too diffuse throughout the simulation. However, similar to the dense gas present in the single filament simulations, wider and more diffuse filaments result in a fast decrease in the total mass of gas above $10^4 \mathrm{cm}^{-3}$.

Regarding gas above $10^5 \mathrm{cm}^{-3}$, we see the same trend in these simulations as we did in our single filament simulations. However, when we consider the $10^3 \mathrm{cm}^{-3}$ threshold in these double filament simulations, we find that the total mass of gas above this density increases over time when the filament density is high (1250 or $850 \mathrm{M}_\odot \mathrm{pc}^3$) by $\approx$ 5 per cent in 3Myr. Conversely, when the filament density is low (600 or $310 \mathrm{M}_\odot \mathrm{pc}^3$), the total

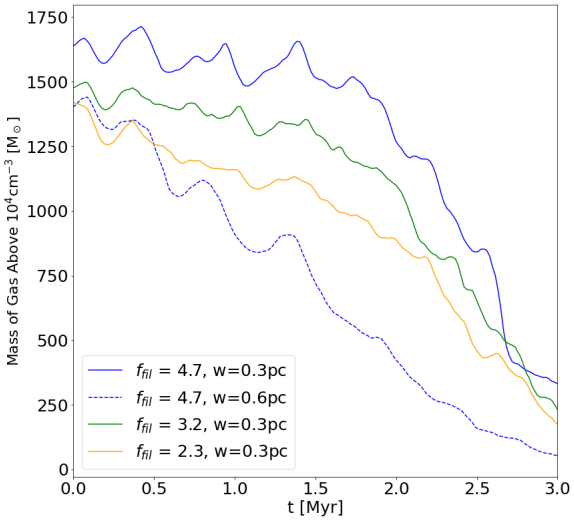

FIGURE 2.9: Total mass of gas above 10^4cm^{-3} for simulations of two filaments accreting onto our smaller star cluster. Colour describes $f_{\text{fil}} \propto \rho w^2$ of the filament in a given simulation and the dashed line denotes a larger filament width.

mass of gas above this threshold plateaus and remains roughly constant for most of the simulation.

Therefore, it is important to know both the width and density of a filament to better understand its impact on the total mass of star forming gas in the accreting cluster when two filaments are accreting. As well, accretion from two filaments has the potential to increase the amount of dense gas available for star formation over time in our simulations, unlike accretion from a single filament.

2.3.4 Dependance of Response to Filamentary Accretion on Cluster Parameters

We performed all of our single and double filament simulations with a more massive central cluster (see simulations that end in C2 in table 2.3). This allows us to determine if the trends found in the previous sections are ubiquitous across star clusters. The cluster in these simulations has a similar gas mass ($M_g \approx 3 \times 10^4 \text{M}_\odot$) as the previous cluster but an increased stellar mass ($M_s \approx 3 \times 10^4 \text{M}_\odot$) leading to an increased total mass. The

filament setups and orientations are the same as the corresponding simulations with the less massive central cluster.

We begin with a discussion of the amount of bound material present in simulations of single and double filamentary systems accreting gas onto our more massive cluster. Beginning with the stellar component, all eight simulations involving the more massive cluster lose less than 1 per cent of stellar mass by their completion. This is independent of any filament parameter including density, width, and number of filaments and is a negligible fraction of the total mass of the cluster. Regarding the gas component, we perform the same analysis as in the previous sections and reach similar conclusions. We find that the central cluster loses a small percentage of its total mass due to interactions with filaments and that this percentage lies in the same range as those from sections 2.3.2.1 and 2.3.3.1. We also find that this is independent of number of filaments, filament width, or filament density.

We now discuss the potentially star forming dense gas present in these simulations. We find that the width of the filament(s) interacting with the central cluster plays less of a role in affecting the amount of dense gas present in the simulations. When considering gas above $10^4 \mathrm{cm}^{-3}$ in the simulations with our widest filament ($w = 0.6\mathrm{pc}$), we do not see the stark decrease in potentially star forming gas that we did in figure 2.9 for example. Rather, the total mass of gas above $10^4 \mathrm{cm}^{-3}$ in these simulations follow a similar trend to that in simulations with lower filament width. Therefore, the size of a filament with respect to the total size of the central cluster is important in determining the amount of potentially star forming gas present throughout the simulation for gas above $10^4 \mathrm{cm}^{-3}$. For gas above 10^3 and $10^5 \mathrm{cm}^{-3}$, we find very similar variance between different filament setups as those found in our simulations with a smaller central cluster showing that this dependence is present for all density thresholds we considered.

Therefore, we conclude that the change in total mass and size of the clusters we considered is important when considering the fraction of dense gas available for star formation in our clusters. It does not have an affect on the fraction of the total mass of the cluster that becomes unbound.

2.3.5 SDC13

A common pattern present in many star forming regions is a distribution of filaments in a "Y" shape involving three main filaments feeding their gas into a central, often times star forming, region (e.g. Könyves et al. 2010, André et al. 2010). This pattern is also present in simulations of GMCs (e.g. Rieder et al. 2022, Grudić et al. 2022). One commonly

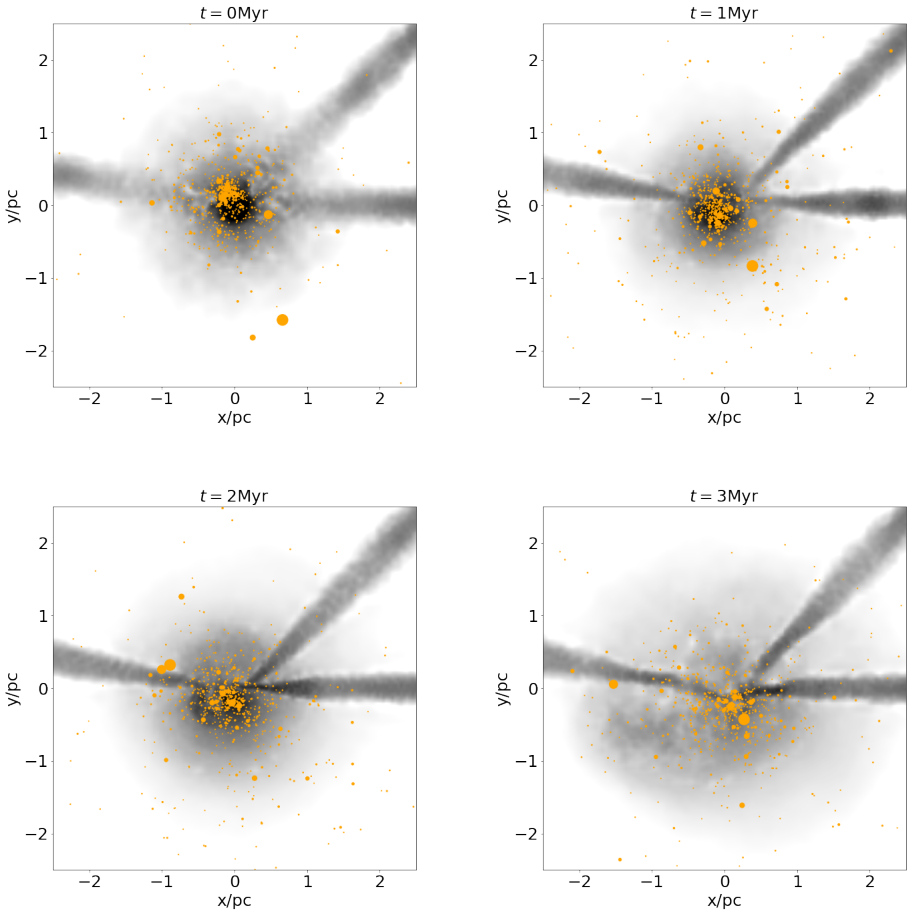

FIGURE 2.10: Same as figure 2.6 but for the simulation SDC.

observed region that contains this filament distribution is the SDC13 region. SDC13 is a hub filament infrared dark cloud located in the galactic plane at a distance of 3.6±0.4kpc (Peretto et al. 2014) and its filamentary network is distributed in a "Y" shape with the filaments feeding gas into a central star forming region. The formation of this particular filament distribution has been studied by Wang et al. (2022) and its subsequent evolution along with the orientation of the filaments has been studied in Williams et al. (2018). We take these filament orientations and create our own simulation of a central cluster accreting dense gas in a similar manner to the SDC13 region. We show snapshots of this simulation in figure 2.10. The parameters of the filaments in this simulation are shown as run SDC in table 2.3. The densities and widths of the simulations used match observations of the SDC13 filaments from Peretto et al. (2014).

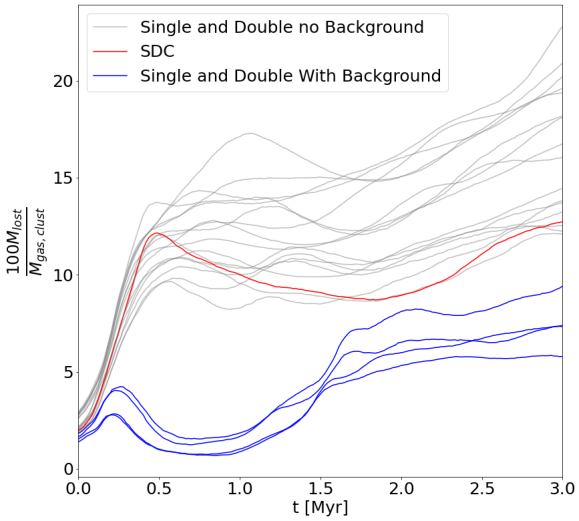

FIGURE 2.11: Same as figure 2.7 but for all filament simulations. The grey lines correspond to all single and double filament simulations with no ambient background gas (sections 2.3.2, 2.3.3, and 2.3.4), the red line shows the SDC simulation (section 2.3.5), and the blue lines correspond to single and double filament simulations that include a background medium (section 2.3.6).

This simulation behaves similarly to our double filament accretion simulation that contains higher density filaments (2FwC1250). The cluster loses very little stellar mass, and it loses a similar amount of gas mass as all previous filament accretion simulations. This can be seen as the red line in figure 2.11 where we show the percentage of the total cluster gas mass that is lost from accretion from filaments for all simulations in table 2.3. As well, we find the same trends as in 2FwC1250 regarding gas above the three density thresholds analyzed in section 2.3.3.2. We discuss this simulation in comparison to all other filament simulations in section 2.4.

This "Y" shape filament configuration is one of many configurations observed throughout star forming regions. For example, hub filament systems can contain very complex filament configurations with many more than three filaments accreting onto a star forming region. We discuss such complexities and how they connect to our work further in section 2.4.

2.3.6 Filamentary Accretion With Ambient Background Gas

Lastly, in this section, we discuss the simulations FCS1250_05, FCS1250_1, 2FCS1250_1, and 2FCS1250_05 (see table 2.3) which are mixtures of our ambient medium and filament simulations. These simulations better resemble the environments found in the real universe where a cluster has formed along a filament that is surrounded by less dense GMC gas and is accreting the surrounding gas. The first two comprise of a single filament with density $\rho = 1250 M_{\odot} pc^{-3}$ and an ambient background medium with density $\rho_{BG} = 0.5$ (FCS1250_05) or $1 M_{\odot} pc^{-3}$ (FCS1250_1) filling the simulation box. The latter two are the same but with two filaments of density $\rho = 1250 M_{\odot} pc^{-3}$ that are set up in the same way as those in section 2.3.3. In all four of these simulations, only the filamentary gas is given a velocity towards the cluster. As well, in all four of these simulation, we use the less massive cluster from table 2.1 as our accreting cluster.

We first look at the amount of bound material present in these four simulations. Similarly to all simulations thus far, the stellar component of each of these simulations does not lose any significant amount of mass through unbinding. Only $< 1 M_{\odot}$ of stellar material is unbound by the end of the simulations. As well, we find that the cluster in these simulations loses much less gas mass than that in the simulations of filamentary accretion without a diffuse background. We show the percentage of the total cluster gas mass that is removed from the cluster for these four simulations as the blue lines in figure 2.11. We also find that there is little difference between one filament and two filament accretion for a given background density regarding the amount of unbound gas present. Therefore, a background medium can be used to help lower the amount of gas removed from a cluster as it interacts with a filament. This implies that a background medium can help the sink particle prescription better represent star clusters accreting gas from filaments.

We now move on to a discussion of the amount of potentially star forming, dense gas present in these simulations. Beginning with the simulations involving accretion from a single filament, we find that gas above $10^3 cm^{-3}$ stays constant for the entirety of the simulation regardless of the background ambient density. The total mass of gas above $10^4 cm^{-3}$ stays constant for ≈ 1Myr which is contrary to the simulations with one filament and no ambient background (see section 2.3.2.2). This implies that the added pressure provided by an ambient medium can help stabilize the amount star forming gas in our single filament simulations, but only for a couple free-fall times. Lastly, gas above $10^5 cm^{-3}$ decreases consistently throughout both simulations.

When we look at the two simulations with two filaments and different ambient background densities, we find that gas above 10^3cm^{-3} increases by 10 per cent for both simulations. The mass of gas above 10^4cm^{-3} and 10^5cm^{-3} stays constant in both simulations for $\approx$ 2Myr and $\approx$ 1Myr respectively. Therefore, we conclude that the addition of a background medium does not result in a substantial change with regards to the amount of dense gas present in our filamentary accretion simulations.

2.4 Summary and Discussion

We have run simulations of gas accretion from both the ambient background medium, and dense filaments onto star clusters whose parameters we obtained from sink particles in a large scale GMC star cluster formation simulation (Howard et al. 2018 (H18)). To simulate accretion from the ambient background medium, we used observations and simulations of GMCs to choose three different background gas densities through which our cluster travelled with three different velocities. To simulate accretion from filaments, we used observations of filamentary regions such as SDC13 to obtain realistic filament densities, widths, and orientations. Throughout both simulation suites, we found that $\lessapprox 20$ per cent of the total gas mass of the cluster is removed from the cluster. Furthermore, this is independent of filament setups (number and orientation) or parameters (density and width) we considered in this work. This has applications to the sink particle prescription used in the H18 simulations. Namely, that the mass quoted by a sink particle representation of our simulations would provide an upper limit to the actual mass of the clusters in our simulations. We also found that the amount of gas above star forming densities inside a cluster can be kept constant from accretion from two filaments if the filaments are dense enough and if their width is small compared to the size of the cluster.

A boundedness check to determine gas accretion onto sinks like that used in H18 is not the only accretion prescription used by sink particles. Some prescriptions, such as that put forward by Krumholz et al. (2004) and subsequently used in the `RAMSES` N-body and SPH code (Bleuler and Teyssier 2014) use idealized Bondi-Hoyle accretion models to calculate accretion rates onto sink particles. Our work shows that, in cases where these sink particles are meant to represent young, gas-rich star clusters, such accretion formalisms may lead to different inaccuracies regarding the mass of the clusters than the H18 sink particle prescription.

Our suite of simulations of a cluster moving through an ambient medium involve a very idealized treatment for the background gas – a constant density. This was done to

test idealized models (Bondi-Hoyle) against more realistic accretion scenarios. In reality, a single GMC can have a wide range of densities through which a young subcluster can travel (Chevance et al. 2022). To accurately include this in our simulations would involve zooming into regions directly from GMC simulations such as H18 to get a more realistic distribution for the background gas. Such a realistic distribution would include regions of varying density implying that the travelling cluster would be interacting with under and over densities. Therefore, the resulting change in the mass of the cluster would be more complicated than in our current simulations. We will address this in future work.

To compare results from our filament simulations to observations, we consider measured filamentary accretion rates. Observations show that velocity gradients along filaments are useful in helping young star clusters grow in mass (e.g. Lee et al. 2013, Yuan et al. 2018, Chen et al. 2019). The corresponding accretion rate of a given filament onto such a young cluster can be calculated using the line mass of that filament. It is defined as $\dot{M}_{\rm acc} = M_{\rm line} v_{\rm inj}$ where $\dot{M}_{\rm acc}$ is the accretion rate, $M_{\rm line}$ is the line mass of the filament, and $v_{\rm inj}$ is the velocity of the filament (Kirk et al. 2013). From velocity gradient and mass observations of filaments, one can therefore conclude the accretion rate given a projection angle through assuming the above simple cylindrical model. This is an idealized cylindrical model that assumes that all of the mass being funneled to the cluster by the filament is bound. We can compare this accretion rate to the rate of change of bound mass of the cluster to see how accurately the accretion rate represents the total change in the clusters mass.

We find that, for all of our single and double filament simulations involving our smaller cluster, the rate of change of the cluster mass averages at $\approx 0.7\dot{M}_{\rm acc}$. For the simulations involving our more massive central cluster, this value averages at $\approx 0.5\dot{M}_{\rm acc}$ and is similar for all filament setups and parameters. As well, the introduction of an ambient medium increases the rate of change of the cluster mass to $\approx 0.8\dot{M}_{\rm acc}$. Lastly, our SDC13 simulation results in an accretion rate that plateaus at $\approx 1\dot{M}_{\rm acc}$ due to the increased potential from the gas funneled by all three filaments. Therefore, idealized cylindrical models represent the total mass of our simulations best when an ambient background is included, or when the common "Y" shape is used for our filament orientations. In our other simulations, they are overestimating the total mass of the cluster.

All of our filament simulations inject filamentary gas towards the cluster at the same velocity ($2{\rm kms}^{-1}$). This choice was made so that the filament would interact with the central cluster before it had a chance to form dense, potentially star forming cores. This allowed us to explore the $f_{\rm fil}$ parameter space more thoroughly. In reality, filament

kinematics can vary. For example, observation of the Mon R2 region performed by Treviño-Morales et al. (2019) show that filament accretion rates can range from 10^{-4} - $10^{-3}M_{\odot}yr^{-1}$ for filaments with line masses in the range 30-100$M_{\odot}pc^{-1}$. While filament velocities of $\approx$ 2kms^{-1} can lie in this range, it can also correspond to filaments with velocities $<$ 1kms^{-1}. Furthermore, gradients along filament widths have been observed in filaments around the Serpens South cluster (Fernández-López et al. 2014, Dhabal et al. 2018, Chen et al. 2019) implying even more complex kinematics along filaments. In this work, we did not explore the parameter space spanned by kinematics. However, because lower filament velocities result in lower kinetic energy injection into the central cluster, we can expect that less gas would be removed from the central cluster is the filament velocities were lower in our simulations. As well, probing lower filament velocities would lead to less gas mass being accreted onto the cluster. These lower velocity filaments would, however, have a chance to form stars that could be accreted onto the cluster at later times.

As well, there exists evidence of a commonality amongst filaments showing that they have characteristic widths of $\approx$ 0.1pc (André et al. 2022). In observations, this value is derived as the full width half maximum (FWHM) of a filament density distribution (Arzoumanian et al. 2011). Using the entire filament density distribution as the filament width has been shown to result in widths of 0.3pc (Peretto et al. 2014) which we used in our simulations (see figure 2.1 for an example). Though our simulations do not consider the FWHM of the filament density distribution as its width, we can still extrapolate how our simulations would behave if our filaments had a width of 0.1pc. Because our results show that the width of a filament with respect to the size of the cluster is important is determining how the cluster will react to accretion, we conclude that accretion from filaments with a width of 0.1pc will result in less gas mass becoming unbound from the cluster. Clusters accreting from filaments with a width of 0.1pc will also see an increase in the amount of potentially star forming dense gas over time. This would lead to an even better agreement with the sink particle prescription when calculating the total mass of the accreting cluster.

Our 30 simulations of gas accretion onto a central star cluster provide us with hints into the complexity of young cluster evolution inside GMCs. Coupling the results from this work with those from Paper I leads to a more comprehensive view of the sink particle prescription, and provides ways in which it can be improved in larger scale GMC simulations. We find that mergers of young gas rich subclusters do more to contribute to inaccuracies between our models and the sink particle prescription than accretion from

ambient background gas or filaments. In the future, it is important to know how the two processes, mergers and gas accretion, affect one another directly. Our future work will probe this further and lead us to simulations of the full build up of massive clusters from H18, and similar simulations, in greater detail.

Bibliography

Aarseth, S. J. (1974). Dynamical evolution of simulated star clusters. I. Isolated models., A&A **35**(2): 237–250.

André, P. (2017). Interstellar filaments and star formation, *Comptes Rendus Geoscience* **349**(5): 187–197.

André, P., Di Francesco, J., Ward-Thompson, D., Inutsuka, S. I., Pudritz, R. E. and Pineda, J. E. (2014). From Filamentary Networks to Dense Cores in Molecular Clouds: Toward a New Paradigm for Star Formation, *in* H. Beuther, R. S. Klessen, C. P. Dullemond and T. Henning (eds), *Protostars and Planets VI*, p. 27.

André, P., Men'shchikov, A., Bontemps, S., Könyves, V., Motte, F., Schneider, N., Didelon, P., Minier, V., Saraceno, P., Ward-Thompson, D., di Francesco, J., White, G., Molinari, S., Testi, L., Abergel, A., Griffin, M., Henning, T., Royer, P., Merín, B., Vavrek, R., Attard, M., Arzoumanian, D., Wilson, C. D., Ade, P., Aussel, H., Baluteau, J. P., Benedettini, M., Bernard, J. P., Blommaert, J. A. D. L., Cambrésy, L., Cox, P., di Giorgio, A., Hargrave, P., Hennemann, M., Huang, M., Kirk, J., Krause, O., Launhardt, R., Leeks, S., Le Pennec, J., Li, J. Z., Martin, P. G., Maury, A., Olofsson, G., Omont, A., Peretto, N., Pezzuto, S., Prusti, T., Roussel, H., Russeil, D., Sauvage, M., Sibthorpe, B., Sicilia-Aguilar, A., Spinoglio, L., Waelkens, C., Woodcraft, A. and Zavagno, A. (2010). From filamentary clouds to prestellar cores to the stellar IMF: Initial highlights from the Herschel Gould Belt Survey, A&A **518**: L102.

André, P., Palmeirim, P. and Arzoumanian, D. (2022). On the typical width of Herschel filaments, *arXiv e-prints* p. arXiv:2210.04736.

Arzoumanian, D., André, P., Didelon, P., Könyves, V., Schneider, N., Men'shchikov, A., Sousbie, T., Zavagno, A., Bontemps, S., di Francesco, J., Griffin, M., Hennemann, M., Hill, T., Kirk, J., Martin, P., Minier, V., Molinari, S., Motte, F., Peretto, N., Pezzuto, S., Spinoglio, L., Ward-Thompson, D., White, G. and Wilson, C. D. (2011). Characterizing interstellar filaments with Herschel in IC 5146, A&A **529**: L6.

Barnes, J. and Hut, P. (1986). A hierarchical O(N log N) force-calculation algorithm, *Nature Astronomy* **324**(6096): 446–449.

Bhadari, N. K., Dewangan, L. K., Ojha, D. K., Pirogov, L. E. and Maity, A. K. (2022). Simultaneous Evidence of Edge Collapse and Hub-filament Configurations: A Rare Case Study of a Giant Molecular Filament, G45.3+0.1, ApJ **930**(2): 169.

Bleuler, A. and Teyssier, R. (2014). Towards a more realistic sink particle algorithm for the RAMSES CODE, MNRAS **445**(4): 4015–4036.

Bondi, H. (1952). On spherically symmetrical accretion, MNRAS **112**: 195.

Calura, F., D'Ercole, A., Vesperini, E., Vanzella, E. and Sollima, A. (2019). Formation of second-generation stars in globular clusters, MNRAS **489**(3): 3269–3284.

Chen, H.-R. V., Zhang, Q., Wright, M. C. H., Busquet, G., Lin, Y., Liu, H. B., Olguin, F. A., Sanhueza, P., Nakamura, F., Palau, A., Ohashi, S., Tatematsu, K. and Liao, L.-W. (2019). Filamentary Accretion Flows in the Infrared Dark Cloud G14.225-0.506 Revealed by ALMA, ApJ **875**(1): 24.

Chevance, M., Krumholz, M. R., McLeod, A. F., Ostriker, E. C., Rosolowsky, E. W. and Sternberg, A. (2022). The Life and Times of Giant Molecular Clouds, *arXiv e-prints* p. arXiv:2203.09570.

Dhabal, A., Mundy, L. G., Rizzo, M. J., Storm, S. and Teuben, P. (2018). Morphology and Kinematics of Filaments in the Serpens and Perseus Molecular Clouds, ApJ **853**(2): 169.

Dobbs, C. L., Bending, T. J. R., Pettitt, A. R. and Bate, M. R. (2022). The formation of massive stellar clusters in converging galactic flows with photoionization, MNRAS **509**(1): 954–973.

Evans, Neal J., I., Dunham, M. M., Jørgensen, J. K., Enoch, M. L., Merín, B., van Dishoeck, E. F., Alcalá, J. M., Myers, P. C., Stapelfeldt, K. R., Huard, T. L., Allen, L. E., Harvey, P. M., van Kempen, T., Blake, G. A., Koerner, D. W., Mundy, L. G., Padgett, D. L. and Sargent, A. I. (2009). The Spitzer c2d Legacy Results: Star-Formation Rates and Efficiencies; Evolution and Lifetimes, ApJS **181**(2): 321–350.

Federrath, C., Banerjee, R., Clark, P. C. and Klessen, R. S. (2010). Modeling Collapse and Accretion in Turbulent Gas Clouds: Implementation and Comparison of Sink Particles in AMR and SPH, ApJ **713**(1): 269–290.

Fernández-López, M., Arce, H. G., Looney, L., Mundy, L. G., Storm, S., Teuben, P. J., Lee, K., Segura-Cox, D., Isella, A., Tobin, J. J., Rosolowsky, E., Plunkett, A., Kwon, W., Kauffmann, J., Ostriker, E., Tassis, K., Shirley, Y. L. and Pound, M. (2014). CARMA Large Area Star Formation Survey: Observational Analysis of Filaments in the Serpens South Molecular Cloud, ApJ **790**(2): L19.

Fischera, J. and Martin, P. G. (2012). Physical properties of interstellar filaments, A&A **542**: A77.

Fujii, M., Iwasawa, M., Funato, Y. and Makino, J. (2007). BRIDGE: A Direct-Tree Hybrid N-Body Algorithm for Fully Self-Consistent Simulations of Star Clusters and Their Parent Galaxies, *PASJ* **59**: 1095.

Fukui, Y., Tokuda, K., Saigo, K., Harada, R., Tachihara, K., Tsuge, K., Inoue, T., Torii, K., Nishimura, A., Zahorecz, S., Nayak, O., Meixner, M., Minamidani, T., Kawamura, A., Mizuno, N., Indebetouw, R., Sewiło, M., Madden, S., Galametz, M., Lebouteiller, V., Chen, C. H. R. and Onishi, T. (2019). An ALMA View of Molecular Filaments in the Large Magellanic Cloud. I. The Formation of High-mass Stars and Pillars in the N159E-Papillon Nebula Triggered by a Cloud-Cloud Collision, ApJ **886**(1): 14.

Gómez, G. C. and Vázquez-Semadeni, E. (2014). Filaments in Simulations of Molecular Cloud Formation, ApJ **791**(2): 124.

Grudić, M. Y., Guszejnov, D., Offner, S. S. R., Rosen, A. L., Raju, A. N., Faucher-Giguère, C.-A. and Hopkins, P. F. (2022). The dynamics and outcome of star formation with jets, radiation, winds, and supernovae in concert, MNRAS **512**(1): 216–232.

Guszejnov, D., Markey, C., Offner, S. S. R., Grudić, M. Y., Faucher-Giguère, C.-A., Rosen, A. L. and Hopkins, P. F. (2022). Cluster assembly and the origin of mass segregation in the STARFORGE simulations, *arXiv e-prints* p. arXiv:2201.01781.

Heiderman, A., Evans, Neal J., I., Allen, L. E., Huard, T. and Heyer, M. (2010). The Star Formation Rate and Gas Surface Density Relation in the Milky Way: Implications for Extragalactic Studies, ApJ **723**(2): 1019–1037.

Howard, C. S., Pudritz, R. E. and Harris, W. E. (2018). A universal route for the formation of massive star clusters in giant molecular clouds, *Nature Astronomy* **2**: 725–730.

Inutsuka, S.-I. and Miyama, S. M. (1992). Self-similar Solutions and the Stability of Collapsing Isothermal Filaments, ApJ **388**: 392.

Inutsuka, S.-i. and Miyama, S. M. (1997). A Production Mechanism for Clusters of Dense Cores, ApJ **480**(2): 681–693.

Kaaz, N., Antoni, A. and Ramirez-Ruiz, E. (2019). Bondi-Hoyle-Lyttleton Accretion onto Star Clusters, ApJ **876**(2): 142.

Karam, J. and Sills, A. (2022). Modelling star cluster formation: mergers, MNRAS **513**(4): 6095–6104.

Kirk, H., Myers, P. C., Bourke, T. L., Gutermuth, R. A., Hedden, A. and Wilson, G. W. (2013). Filamentary Accretion Flows in the Embedded Serpens South Protocluster, ApJ **766**(2): 115.

Könyves, V., André, P., Men'shchikov, A., Schneider, N., Arzoumanian, D., Bontemps, S., Attard, M., Motte, F., Didelon, P., Maury, A., Abergel, A., Ali, B., Baluteau, J. P., Bernard, J. P., Cambrésy, L., Cox, P., di Francesco, J., di Giorgio, A. M., Griffin, M. J., Hargrave, P., Huang, M., Kirk, J., Li, J. Z., Martin, P., Minier, V., Molinari, S., Olofsson, G., Pezzuto, S., Russeil, D., Roussel, H., Saraceno, P., Sauvage, M., Sibthorpe, B., Spinoglio, L., Testi, L., Ward-Thompson, D., White, G., Wilson, C. D., Woodcraft, A. and Zavagno, A. (2010). The Aquila prestellar core population revealed by Herschel, A&A **518**: L106.

Kroupa, P. (2001). On the variation of the initial mass function, MNRAS **322**(2): 231–246.

Krumholz, M. R., McKee, C. F. and Klein, R. I. (2004). Embedding Lagrangian Sink Particles in Eulerian Grids, ApJ **611**(1): 399–412.

Kumar, M. S. N., Arzoumanian, D., Men'shchikov, A., Palmeirim, P., Matsumura, M. and Inutsuka, S. (2022). Filament coalescence and hub structure in Mon R2. Implications for massive star and cluster formation, A&A **658**: A114.

Lada, C. J., Forbrich, J., Lombardi, M. and Alves, J. F. (2012). Star Formation Rates in Molecular Clouds and the Nature of the Extragalactic Scaling Relations, ApJ **745**(2): 190.

Lada, C. J. and Lada, E. A. (2003). Embedded Clusters in Molecular Clouds, *Annual Reviews of* A&A **41**: 57–115.

Lada, C. J., Lombardi, M. and Alves, J. F. (2010). On the Star Formation Rates in Molecular Clouds, ApJ **724**(1): 687–693.

Lee, K., Looney, L. W., Schnee, S. and Li, Z.-Y. (2013). Earliest Stages of Protocluster Formation: Substructure and Kinematics of Starless Cores in Orion, ApJ **772**(2): 100.

Li, H., Vogelsberger, M., Marinacci, F. and Gnedin, O. Y. (2019). Disruption of giant molecular clouds and formation of bound star clusters under the influence of momentum stellar feedback, MNRAS **487**(1): 364–380.

Makino, J. and Aarseth, S. J. (1992). On a Hermite Integrator with Ahmad-Cohen Scheme for Gravitational Many-Body Problems, *PASJ* **44**: 141–151.

Men'shchikov, A., André, P., Didelon, P., Könyves, V., Schneider, N., Motte, F., Bontemps, S., Arzoumanian, D., Attard, M., Abergel, A., Baluteau, J. P., Bernard, J. P., Cambrésy, L., Cox, P., di Francesco, J., di Giorgio, A. M., Griffin, M., Hargrave, P., Huang, M., Kirk, J., Li, J. Z., Martin, P., Minier, V., Miville-Deschênes, M. A., Molinari, S., Olofsson, G., Pezzuto, S., Roussel, H., Russeil, D., Saraceno, P., Sauvage, M., Sibthorpe, B., Spinoglio, L., Testi, L., Ward-Thompson, D., White, G., Wilson, C. D., Woodcraft, A. and Zavagno, A. (2010). Filamentary structures and compact objects in the Aquila and Polaris clouds observed by Herschel, A&A **518**: L103.

Naiman, J. P., Ramirez-Ruiz, E. and Lin, D. N. C. (2011). External Mass Accumulation onto Core Potentials: Implications for Star Clusters, Galaxies, and Galaxy Clusters, ApJ **735**(1): 25.

Ostriker, J. (1964). The Equilibrium of Polytropic and Isothermal Cylinders., ApJ **140**: 1056.

Pelupessy, F. I. and Portegies Zwart, S. (2012). The evolution of embedded star clusters, MNRAS **420**(2): 1503–1517.

Peretto, N., Fuller, G. A., André, P., Arzoumanian, D., Rivilla, V. M., Bardeau, S., Duarte Puertas, S., Guzman Fernandez, J. P., Lenfestey, C., Li, G. X., Olguin, F. A., Röck, B. R., de Villiers, H. and Williams, J. (2014). SDC13 infrared dark clouds: Longitudinally collapsing filaments?, A&A **561**: A83.

Plummer, H. C. (1911). On the problem of distribution in globular star clusters, MNRAS **71**: 460–470.

Portegies Zwart, S. F., McMillan, S. L. W. and Gieles, M. (2010). Young Massive Star Clusters, *Annual Reviews of* A&A **48**: 431–493.

Portegies Zwart, S., McMillan, S., Harfst, S., Groen, D., Fujii, M., Nualláin, B. Ó., Glebbeek, E., Heggie, D., Lombardi, J., Hut, P., Angelou, V., Banerjee, S., Belkus,

H., Fragos, T., Fregeau, J., Gaburov, E., Izzard, R., Jurić, M., Justham, S., Sottoriva, A., Teuben, P., van Bever, J., Yaron, O. and Zemp, M. (2009). A multiphysics and multiscale software environment for modeling astrophysical systems, *New Astronomy* **14**(4): 369–378.

Rieder, S., Dobbs, C., Bending, T., Liow, K. Y. and Wurster, J. (2022). The formation and early evolution of embedded star clusters in spiral galaxies, MNRAS **509**(4): 6155–6168.

Rosolowsky, E., Hughes, A., Leroy, A. K., Sun, J., Querejeta, M., Schruba, A., Usero, A., Herrera, C. N., Liu, D., Pety, J., Saito, T., Bešlić, I., Bigiel, F., Blanc, G., Chevance, M., Dale, D. A., Deger, S., Faesi, C. M., Glover, S. C. O., Henshaw, J. D., Klessen, R. S., Kruijssen, J. M. D., Larson, K., Lee, J., Meidt, S., Mok, A., Schinnerer, E., Thilker, D. A. and Williams, T. G. (2021). Giant molecular cloud catalogues for PHANGS-ALMA: methods and initial results, MNRAS **502**(1): 1218–1245.

Shima, E., Matsuda, T., Takeda, H. and Sawada, K. (1985). Hydrodynamic calculations of axisymmetric accretion flow, MNRAS **217**: 367–386.

Springel, V. (2005). The cosmological simulation code GADGET-2, MNRAS **364**(4): 1105–1134.

Treviño-Morales, S. P., Fuente, A., Sánchez-Monge, Á., Kainulainen, J., Didelon, P., Suri, S., Schneider, N., Ballesteros-Paredes, J., Lee, Y. N., Hennebelle, P., Pilleri, P., González-García, M., Kramer, C., García-Burillo, S., Luna, A., Goicoechea, J. R., Tremblin, P. and Geen, S. (2019). Dynamics of cluster-forming hub-filament systems. The case of the high-mass star-forming complex Monoceros R2, A&A **629**: A81.

Wang, J.-W., Koch, P. M., Tang, Y.-W., Fuller, G. A., Peretto, N., Williams, G. M., Yen, H.-W., Lee, H.-T. and Chen, W.-A. (2022). Formation of the SDC13 Hub-filament System: A Cloud-Cloud Collision Imprinted on the Multiscale Magnetic Field, ApJ **931**(2): 115.

White, S. D. M. (1994). Formation and Evolution of Galaxies: Les Houches Lectures, *arXiv e-prints* pp. astro–ph/9410043.

Williams, G. M., Peretto, N., Avison, A., Duarte-Cabral, A. and Fuller, G. A. (2018). Gravity drives the evolution of infrared dark hubs: JVLA observations of SDC13, A&A **613**: A11.

Wong, T., Oudshoorn, L., Sofovich, E., Green, A., Shah, C., Indebetouw, R., Meixner, M., Hacar, A., Nayak, O., Tokuda, K., Bolatto, A. D., Chevance, M., De Marchi, G., Fukui, Y., Hirschauer, A. S., Jameson, K. E., Kalari, V., Lebouteiller, V., Looney, L. W., Madden, S. C., Onishi, T., Roman-Duval, J., Rubio, M. and Tielens, A. G. G. M. (2022). The 30 Doradus Molecular Cloud at 0.4 pc Resolution with the Atacama Large Millimeter/submillimeter Array: Physical Properties and the Boundedness of CO-emitting Structures, *arXiv e-prints* p. arXiv:2206.06528.

Yuan, J., Li, J.-Z., Wu, Y., Ellingsen, S. P., Henkel, C., Wang, K., Liu, T., Liu, H.-L., Zavagno, A., Ren, Z. and Huang, Y.-F. (2018). High-mass Star Formation through Filamentary Collapse and Clump-fed Accretion in G22, ApJ **852**(1): 12.

Chapter 3

Dynamics of Star Cluster Buildup in Realistic Environments

The content of this chapter is a second revision of the manuscript text for publication under the following citation:

Karam, J. & Sills, A. (2024). Dynamics of Star Cluster Formation: Mergers in Gas Rich Environments. The Astrophysical Journal, 967, 86

Dynamics of Star Cluster Formation: Mergers in Gas-rich Environments

Jeremy Karam
Department of Physics and Astronomy
McMaster University, Hamilton, ON, Canada
Email: karamj2@mcmaster.ca

Alison Sills
Department of Physics and Astronomy
McMaster University, Hamilton, ON, Canada
Email: asills@mcmaster.ca

Abstract

We perform high resolution simulations of forming star clusters as they merge inside giant molecular clouds (GMCs) using hydrodynamics coupled to N-body dynamics to simultaneously model both the gas and stars. We zoom in to previously run GMC simulations and resolve clusters into their stellar and gas components while including the surrounding GMC environment. We find that GMC gas is important in facilitating the growth of clusters in their embedded phase by promoting cluster mergers. Mergers induce asymmetric expansion of the stellar component of the clusters in our simulations. As well, mergers induce angular momentum in the clusters' stellar and gas components. We find that mergers can lead to an increase in the amount of dense gas present in clusters if a background gas distribution is present. We predict that this can lead to new star formation that can change the overall distribution of cluster stars in velocity space. Our results suggest that subcluster mergers in the presence of background gas can imprint dynamical signatures that can be used to constrain cluster formation histories.

Keywords: *Star Clusters (1567) — Stellar Dynamics (1596) — Stellar Kinamatics (1608) — Star Formation (1569)*

3.1 Introduction

The first few Myr of star cluster formation takes place embedded inside giant molecular clouds (GMCs) (Lada and Lada 2003). Simulations of this phase of star cluster formation have found that clusters form hierarchically, through mergers of smaller subclusters (e.g.Vázquez-Semadeni et al. 2017, Howard et al. 2018, Chen et al. 2021, Dobbs et al. 2022, Rieder et al. 2022). Recent observations from JWST have explored hierarchical buildup in the context of young massive cluster formation (e.g. Fahrion and De Marchi 2023). Mergers, alongside interaction with surrounding GMC gas, have been shown to affect cluster size, mass, and density distribution (Karam and Sills 2022, Karam and Sills 2023, hereafter Paper I and Paper II respectively).

The dynamics of stars in young clusters are important observables used to probe their formation history. One example is cluster expansion which has been observed in many young star clusters (e.g. Kuhn et al. 2019, Kuhn et al. 2022, Kounkel et al. 2022, Della Croce et al. 2023), and associations (e.g. Lim et al. 2023). Recent work has found that expansion can be anisotropic around young clusters (e.g. Wright et al. 2019, Wright et al. 2023) implying that the cluster structure before expansion may not be spherical. Further evidence of substructure has been inferred from observation of the distribution of cluster stars in velocity space. Wright and Mamajek (2018) find evidence of kinematic substructure inside components of the Sco Cen OB association, and use this to argue that the distribution of stars in position space was once substructured.

Another potential dynamical imprint of the embedded phase of star cluster formation is cluster rotation. Low rotational velocities have been observed in globular clusters (e.g. Bellazzini et al. 2012, Bianchini et al. 2018) and in young massive star clusters (e.g. Hénault-Brunet et al. 2012). If young massive clusters are present day analogues of globular clusters (see Portegies Zwart et al. 2010), then globular cluster rotation may be inherited from the evolution of young clusters inside their embedded clouds. A full understanding of the evolution of embedded clusters must factor in these dynamical observations.

Simulations of young star cluster formation and evolution have been able to reproduce some of these observed dynamical signatures. N-body simulations (Geyer and Burkert 2001, Baumgardt and Kroupa 2007), along with simulations that include N-body, hydrodynamics, and stellar feedback (e.g. Pelupessy and Portegies Zwart 2012), have shown that cluster expansion can be caused by the expulsion of the gas within which young clusters are embedded. These simulations, however, assume that the embedded phase

of star cluster formation results in a cluster that is spherical immediately before gas expulsion. To better understand the hierarchical buildup of the cluster in the embedded phase, one can turn to simulations of cluster evolution inside GMCs. Such simulations have found that star clusters can form with primordial rotation and that the strength of their rotation may depend on their mass (Lahén et al. 2020, Chen et al. 2021).

Large scale simulations like these come with their own set of limitations in the form of resolution. If GMCs are very massive (10^{6-7}M$_\odot$), one cannot resolve the evolution of the individual stars present in the GMC in a simulation while including all physical mechanisms that affect the GMC (e.g. Howard et al. 2018, Ali et al. 2023). Instead, such large scale simulations employ the use of sink particles to model their clusters. A standard procedure is to use the sink particle implementation described in Federrath et al. (2010) where the cluster is modelled as a point particle with an accretion radius. The sink carries with it parameters that describe the cluster it represents (i.e. its total mass, mass in stars, position, and velocity).

In this work, we take regions from the Howard et al. (2018) (hereafter H18) GMC simulations and isolate them so that we can resolve the sink particles as collections of stars and gas that are more representative of a young, embedded cluster. We examine how the evolution inside the GMC environment affects the stars and gas present in the clusters through the inclusion of realistic background gas from the H18 GMC simulation. We also perform simulations without background gas that build upon our work in Paper I by investigating the effects of geometry on cluster mergers.

In Section 3.2 we discuss the initial conditions of our simulations and how we convert the H18 data to our higher resolution framework. In section 3.3 we discuss the evolution of isolated star cluster mergers with varying impact parameters. In Section 3.4 we discuss the dynamics of the stellar component of the clusters in our zoom-in simulations. In Section 3.5 we discuss the evolution of the gas component of our zoom-in simulations. In Section 3.6, we summarize and discuss the implications of our results and how they relate to observations of older star clusters.

3.2 Methods

3.2.1 Numerical Methods

We perform our simulations using the Astrophysical Multipurpose Software Environment (AMUSE) (Portegies Zwart et al. 2009, Pelupessy et al. 2013, Portegies Zwart et al.

Simulation Name	$M_{BG,g}$ [$10^4 M_\odot$]	b [$L_{50,MM}$]	Cluster Name	M_s [$10^3 M_\odot$]	M_g [$10^4 M_\odot$]	L_{50} [pc]
`b0p5`	0.0	0.5	A	0.2	0.2	0.4
			B	0.2	0.4	0.4
`b1`	0.0	1.0	A	0.2	0.2	0.4
			B	0.2	0.4	0.4
`b1p5`	0.0	1.5	A	0.2	0.2	0.4
			B	0.2	0.4	0.4
`b2`	0.0	2.0	A	0.2	0.2	0.4
			B	0.2	0.4	0.4
`region1`	4.9	1.3	A	0.2	0.2	0.4
			B	0.2	0.4	0.4
			C	0.6	0.5	0.5
`region2`	7.5	1.9	A	0.7	0.8	0.7
			B	0.9	0.6	0.6
			C	6.5	2.8	0.9
`region3`	5.0	(1.1, 0.7)	A	0.6	0.4	0.6
			B	0.7	0.1	0.3
			C	9.1	1.0	0.8

TABLE 3.1: Parameters for our simulations. Column 1: the simulation name, column 2: the mass of background gas, column 3: the impact parameter of the merger(s) in units of the stellar component 50% Lagrangian radius of the cluster with the more massive stellar component in the merger, column 4: the star cluster name, column 5: the initial stellar mass of the cluster, column 6: the initial gas mass of the cluster, column 7: the initial stellar 50% Lagrangian radius of the cluster.

2013). AMUSE contains codes that evolve the equations of gravity and hydrodynamics. As well, it allows for the communication between codes meaning that we can simulate the evolution of the stellar and gas components in a cluster and analyze how both components interact with each other. We use `hermite0` (Makino and Aarseth 1992) as our N-body code, and `GADGET-2` (Springel 2005) as our smoothed particle hydrodynamics (SPH) code. We use `BRIDGE` (Fujii et al. 2007) as our communication scheme with `BHTree` (written by Jun Makino based on Barnes and Hut 1986) as the connecting algorithm. For more details on our numerical scheme, see Paper I.

We use Plummer (Plummer 1911) spheres of stars and gas to set up our star clusters. We take the total stellar and gas mass of the cluster from sinks in the H18 simulation. We assign the masses of the individual stars using a Kroupa (Kroupa 2001) IMF with a lower mass limit of $0.15\mathrm{M}_{\odot}$, and an upper mass limit of $100\mathrm{M}_{\odot}$. We give our SPH gas particles a mass of $m_{\mathrm{SPH}} = 0.03\mathrm{M}_{\odot}$ (we discuss this choice in more detail in Section 3.2.3) and set the gas temperature to 10K. We use an adiabatic equation of state for the gas. We use the method outlined in Aarseth (1974) to sample the velocities of the stars and gas in the cluster, and scale the velocities such that our clusters are initially in virial equilibrium ($2K_{\mathrm{s,g}}/|U_{\mathrm{s,g}}| = 1$ where $K_{\mathrm{s,g}}$ is the kinetic energy of the stars or gas, and $U_{\mathrm{s,g}}$ is the potential energy of the stars or gas).We chose the scale radius of both the stellar and gas Plummer spheres such that the density at the clusters half mass radius is consistent with young massive cluster observations shown in Portegies Zwart et al. (2010) ($\rho_{\mathrm{hm}} \approx 10^3 - 10^4 \mathrm{M}_{\odot}\mathrm{pc}^{-3}$). For more detail regarding the set up of our star clusters, see Paper I.

3.2.2 Isolated Merger Simulations

The merger simulations presented in Paper I were all head-on collisions. This is not necessarily true for mergers in the H18 GMC simulations. To build upon the results from Paper I we first run off-axis cluster merger simulations. We perform simulations of two clusters merging along the x-axis with their centres offset along the y-axis by some impact parameter value that we label as b. The parameters for the clusters in these simulations can be seen in the top four rows of Table 3.1. The mergers in all four of these simulations have the same collisional velocity of $6.9\mathrm{kms}^{-1}$. The stellar and gas masses of these clusters, as well as the collision velocity, were chosen to be the same as the clusters that merge in the first of our more realistic merger simulations in a background gas potential, described in the next section.

3.2.3 Clusters in Realistic Background Gas Distributions

The bulk of our results come from our simulations of clusters evolving inside realistic background gas distributions. The initial conditions for the clusters and background gas in these simulations are taken from the H18 GMC simulations. These were a set of radiative, magneto-hydrodynamical simulations that used the `FLASH` (Fryxell et al. 2000) adaptive mesh refinement (AMR) grid code to follow the formation of star clusters inside an evolving GMC.

We select three regions from their simulation of a $10^7 M_\odot$ GMC with a metallicity of $0.1 Z_\odot$ to use as our initial conditions. All three of these regions contain three sink particles each. In the H18 simulations, two sinks in `region1` will merge in the vicinity of the third, more massive sink. The same is true in `region2`. In `region3`, all three sinks merge until one sink is left by the end of the simulation. The widths along x, y, and z of `region1`, `region2`, and `region3` are (20, 10, 20)pc, (14, 20, 14)pc, (10, 20, 20)pc respectively. Once we selected our regions, we convert the background gas present in each region from the H18 grid to an SPH particle distribution. We use a method adapted from Rey-Raposo et al. (2015) where the goal was to increase the resolution of SPH simulations by decreasing the SPH particle mass.

We begin by distributing $N_{\rm SPH} = M_{\rm cell}/m_{\rm SPH}$ (where $M_{\rm cell}$ is the mass of a given grid cell) SPH particles using a Gaussian around the centre of each grid cell. Each H18 cell is either 0.67 or 1.35pc on a side in these regions of the simulation, so there are approximately 14 thousand cells in `region1`, 8 thousand cells in `region2`, and 13 thousand cells in `region3`. We could choose to uniformly distribute the SPH particles inside each grid cell, but because the grid cells from the H18 simulations had large widths, the SPH representation would maintain the grid shape for much of the simulation. We choose the standard deviation of the Gaussian to be the width of the grid cell because this choice allows for the best conservation of density between the grid and SPH representations of the gas. We choose $m_{\rm SPH} = 0.03 M_\odot$ because this allows us to adequately sample SPH particles for a given cell without unnecessarily increasing the computation runtime. For `region1`, `region2`, and `region3`, we have a total of approximately 1.6 million, 2.5 million, and 1.7 million SPH particles in background gas respectively.

Next, we give all the SPH particles the same velocity as that of the cell that they are representing. To prevent the SPH representation from clumping, we apply a velocity dispersion of $0.5 {\rm kms}^{-1}$ to the velocity of the SPH particle inherited from its parent cell. We then divide the thermal energy of a given grid cell evenly amongst all the SPH

particles we place around its centre such that $E_{\rm th,SPH} = E_{\rm th,cell}/N_{\rm SPH}$ where $E_{\rm th,SPH}$ is the thermal energy of a given SPH particle, and $E_{\rm th,cell}$ is the specific thermal energy of the cell that the particles are representing. The background gas in our selected regions is not particularly uniform, but has a density range of about 4 orders of magnitude as can be seen in Figures 3.1, 3.6, and 3.8.

We find that this method gives good overall agreement between the total mass in the grid and SPH representation for the regions of the H18 simulation we selected. The total mass of our SPH representation is within 0.1% of the total mass from the grid simulation for all three regions we selected. As well, we find that the energies are well conserved between both representations. For all regions selected, the potential energy of the SPH representation is $\approx 95\%$ that of the original grid representation, the kinetic energy of the SPH representation is $< 0.5\%$ higher than the original grid representation, and the thermal energy of the SPH and grid representation are the same.

Once we have converted the background gas into an SPH representation, we replace the sink particles present in each region with star clusters made up of stars and gas using the method outlined in Section 3.2.1 and in Paper I. We show the parameters of these simulations in the bottom three rows of Table 3.1.

3.2.4 Identifying Star Clusters

To identify clusters throughout our simulations, we begin by using DBSCAN (Ester et al. 1996, Pedregosa et al. 2011) to spatially cluster the stars ensuring that there are five neighbouring stars within a given radius away from each star (Sander et al. 1998). We choose this radius such that the initial spatial clustering by DBSCAN returns the same number of clusters as there are sink particles initially in the region from H18. Once we have spatially clustered the stars, we check that each star is bound to its respective cluster by calculating its kinetic and potential energies. Finally, we check if spatially unclustered stars are bound. If they are, we assign it to the cluster with which it is most bound.

To assign gas to each cluster, we first make sure that the gas is bound. We then calculate the potential energy felt on the gas from each cluster and assign each bound gas particle to the cluster to which it is most bound.

3.3 Isolated Off-Axis Mergers

We first analyze our off-axis isolated merger simulations. Lower impact parameter mergers only result in a slight increase in the amount of unbound stellar mass in the resultant cluster. By the end of simulations `b0p5`, `b1`, `b1p5`, and `b2`, the resultant cluster has lost of $14, 10, 7$, and 5% of its total stellar mass through the merger. Though the resultant clusters lose less gas mass than stellar mass in each simulation, we find the same trend with changing impact parameter regarding the bound gas component of the resultant cluster.

Simulations `b1`, `b1p5` and `b2` result in a cluster that is non-monolithic (two distinct stellar and gas components). In Paper I, we found non-monolithic resultant clusters for mergers with collisional velocities $\gtrapprox 10\text{kms}^{-1}$. The simulations presented here all have lower collisional velocities. Therefore, a larger impact parameter can lower the required collisional velocity to produce a non-monolithic cluster after a merger.

Though we do not include a star formation prescription in our simulations, we can track the amount of dense gas to predict how star formation would be affected. We consider gas with densities above 10^3, 10^4 and 10^5cm^{-3} as these have been considered as density thresholds above which star formation occurs in observations and simulations (e.g Elmegreen 2001, Enoch et al. 2008, Lada et al. 2012, Dobbs et al. 2022). The amount of gas with densities above these thresholds peaks at the time of the merger, and decreases below its original value by the end of the simulation. Smaller impact parameter mergers result in a larger but shorter-lived increase in gas above 10^4 and 10^5cm^{-3}. Higher impact parameter mergers result in clusters which hold on to more gas above these density thresholds at the end of the simulation.

3.4 Zoom-In Regions: Stars

3.4.1 Region1

We show snapshots of a portion of the `region1` simulation in Figure 3.1. The circles are colour-coded depending on the cluster to which they initially belong with red, blue, and orange corresponding to clusters A, B, and C respectively. Initially, cluster A is moving towards cluster B in the x-y plane. At t$\approx$0.1Myr, our cluster identification scheme determines that the merger has begun. At t$\approx$0.4Myr, the stellar components of the two clusters reach their closest approach. They stay as a monolithic cluster for the remainder

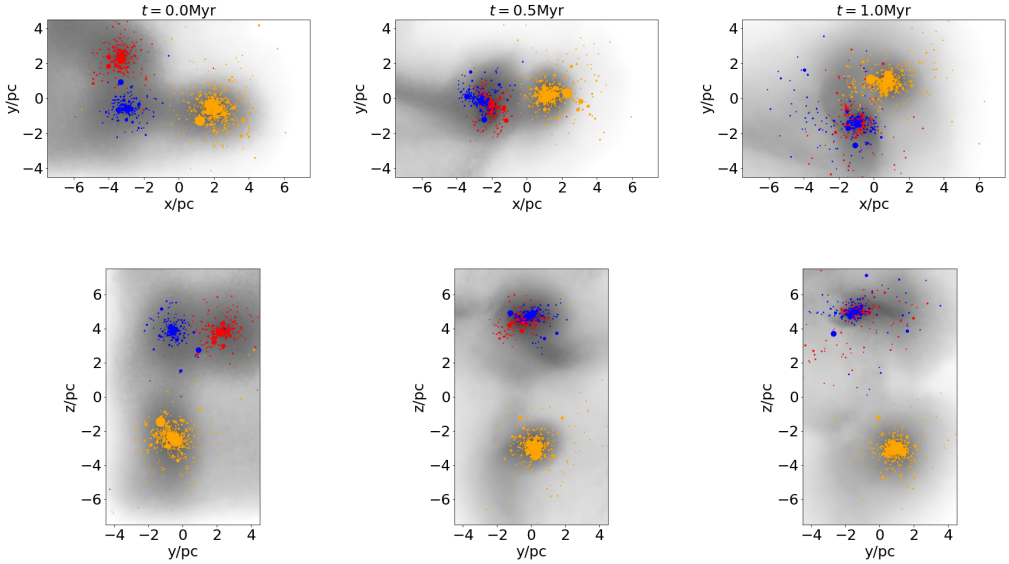

FIGURE 3.1: Snapshots of the stars and gas from the `region1` simulation in the x-y (top row) and y-z (bottom row) planes. The circles represent the stars in each cluster and their size scales with the stars mass. The lowest and highest mass stars in this simulation are $0.15 M_{\odot}$ and $41.70 M_{\odot}$ respectively. The gas is shown in black with darker regions showing gas with higher densities. The range in gas densities shown here is $0.1-10^3 M_{\odot} pc^{-3}$.

of the simulation. We call the resultant monolithic cluster "cluster AB". Cluster C does not merge with cluster A, cluster B or cluster AB throughout the simulation.

The mass ratio, defined as the total (stellar and gas) mass of the more massive cluster divided by that of the less massive cluster, of the merger of cluster A with cluster B is $f_{\rm M} = 1.9$ and the collisional velocity of the merger is 6.9 kms^{-1}. The impact parameter of the merger of cluster A with cluster B is $1.3{\rm L}_{50,{\rm A}}$ where $\rm L_{50,A}$ is the 50% Lagrangian radius of cluster A. In the previous section, we found that the simulation with similar properties (`b1`, and `b1p5`), but with no background gas resulted in a non-monolithic cluster. This demonstrates the importance of the background gas distribution on the structure of merging star clusters as it can be used to keep clusters monolithic. We confirmed the impact of the background gas on the evolution of the clusters in the `region1` simulation by running a simulation with the same setup as `region1`, but with no background gas distribution. We find that when the background gas is not included, clusters A and B do not merge to form a monolithic cluster by the end of the simulation.

The merger of cluster A and B in the `region1` simulation results in a small fraction of stars becoming unbound from cluster AB. The total mass in unbound stars in this simulation is <3% of the total stellar mass which is less than the amount of unbound stellar mass produced from our merger simulations in Paper I and in Section 3.3. This is expected as the addition of background gas in these simulations provides an added potential that helps keep the stars and gas bound to their respective clusters.

3.4.1.1 Velocity Space Distribution

Figure 3.2 shows that, around the time of the merger of cluster A and B at 0.1-0.4Myr, the velocity dispersions of the stars involved in the merger increase by more than a factor of two. Because the merger of clusters A and B results in a large and rapid change in the potential felt by the stars involved, this can be described as a violent relaxation process (Lyden-Bell; 1967). We estimate the violent relaxation timescale to be ≈0.4Myr for this merger. This increase lasts for approximately one violent relaxation time, after which the velocity dispersions stabilize. As well, we find that the velocity dispersion of the stars belonging to cluster AB are independent of their mass. This confirms that violent relaxation is occurring in the resultant cluster (Bonilla-Barroso et al.; 2022).

We use the virial parameter (defined as $\alpha = 2K/|U|$ where K is the kinetic energy of the stars and gas bound to the cluster, and U is the potential energy of the stars and gas bound to the cluster) to analyze whether cluster AB is stable after the merger. We calculate a virial parameter of $\alpha = 0.38$ at the end of the simulation implying that cluster

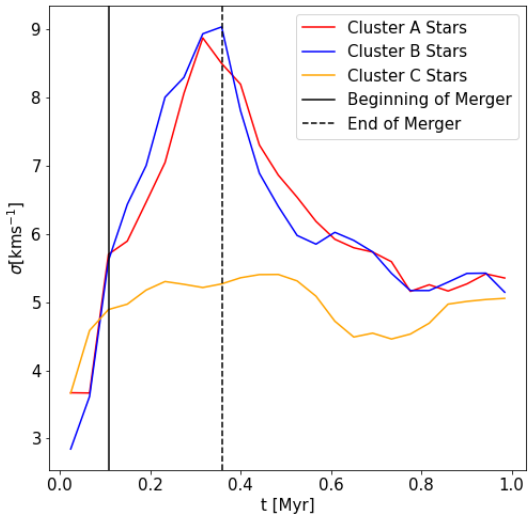

FIGURE 3.2: Velocity dispersion of the stars originally belonging to clusters A (red), B (blue), and C (orange) throughout the `region1` simulation. The solid and dashed black lines show the beginning and end of the merger of cluster A with cluster B respectively.

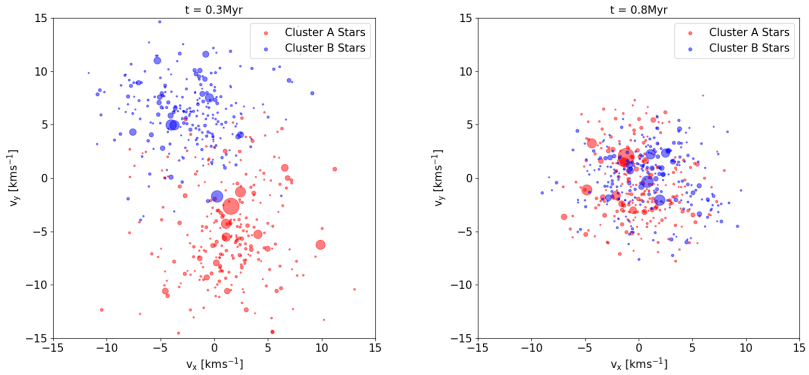

FIGURE 3.3: Velocities of stars originally belonging to clusters A (red) and B (blue) around the centre of mass velocity of cluster AB at two snapshots in the `region1` simulation. The size of the circles scales with the mass of the star.

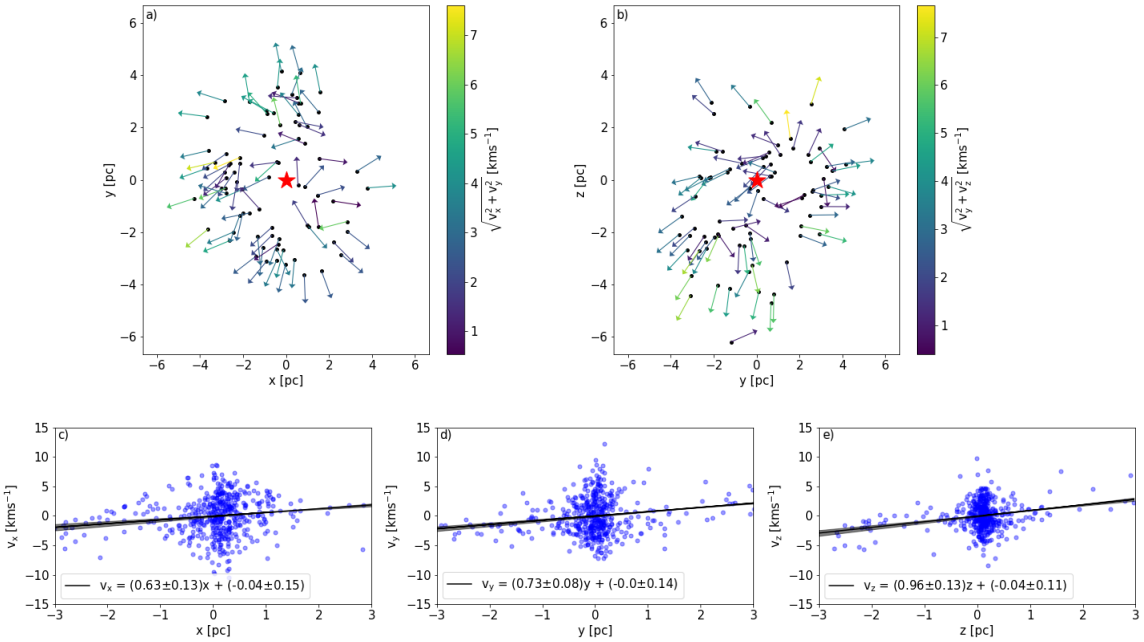

FIGURE 3.4: Expansion of cluster AB in the `region1` simulation at the end of the simulation. All positions and velocities in this figure are about the centre of mass and centre of mass velocity respectively. a), b): Location of stars (black points) beyond the 90% Lagrangian radius at the end of the simulation in x-y and y-z planes. Arrows are unit vectors which show direction of the velocity vectors in the corresponding plane. The colour of the arrows corresponds to the magnitude of the velocity vectors. The red star indicates the location of the centre of mass of cluster AB. c), d), e): Position of each star along x, y, and z plotted against velocity of the star in the same direction. Black lines show the line of best fit with shaded regions showing one sigma of the fit calculated through bootstrapping 10^5 times.

AB is bound even after the increase in the velocity dispersion of the stellar component. This is consistent with the low fraction of unbound stars after the merger.

Next, we consider whether the stars that make up the merged cluster AB carry with them any memory of their velocity space structure before the merger. We show snapshots of the x and y velocities of the cluster A and B stars subtracted by the centre of mass velocity of cluster AB in Figure 3.3 at different times in the simulation. The top panel shows a snapshot of the stars in velocity space during the merger, and the bottom panel shows a snapshot corresponding to one violent relaxation time after the merger has finished. During the merger, the two groups of stars are most distinguishable. This is quickly erased after ≈1 violent relaxation time. They stay mixed until the end of our simulation. We find the same trend in the distribution of velocities along the y and z axes. We conclude that the violent relaxation process has removed velocity signatures that were unique to the stars belonging to the clusters involved in this merger.

3.4.1.2 Expansion and Rotation

After an initial growth, the 10%, 50%, and 75% Lagrangian radii stay roughly constant after the merger. The 90% Lagrangian radius increases for the entirety of the simulation after the merger implying that the majority of the expansion of cluster AB after the merger is beyond the 75% Lagrangian radius. Figure 3.4 shows an analysis of the expansion of cluster AB. We plot different measures of the expansion around the centre of cluster AB at the end of the `region1` simulation. The top panels show the orientation of the velocity vectors of the stars beyond the 90% Lagrangian radius of cluster AB in the x-y and y-z planes. From these panels, we see that the expansion is not isotropic at the end of the simulation in either plane.

We calculate the rate of expansion throughout the merger using the method outlined in Wright and Mamajek (2018). An example of this process applied to cluster AB at the end of the simulation can be seen in the bottom panels of Figure 3.4. We first plot the position of the stars along a given axis against the velocity of the stars along that same axis (e.g. x vs v_x). Next, we fit a line to the data (black lines in panels c), d) and e) of Figure 3.4). The slope of that line gives us a measure of the rate of the expansion. A positive slope refers to expansion while a negative slope refers to contraction. We do this for all times after the merger and find that the rate of the expansion of the stellar component of cluster AB is not constant over time. During the merger, the expansion rate is negative, indicating that the stellar component is contracting as the stars of cluster A and B move towards each other. After the merger, the expansion rates in x, y

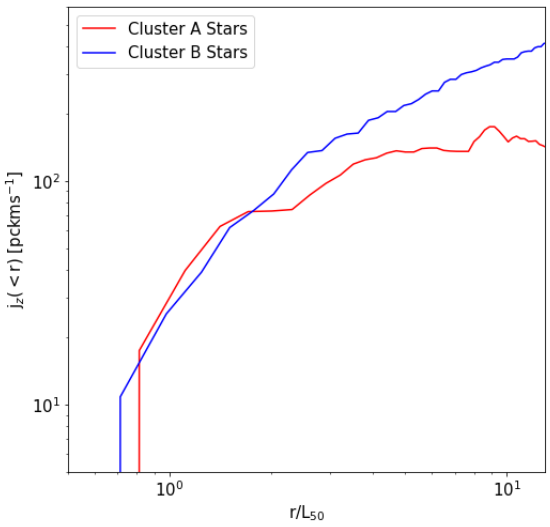

FIGURE 3.5: Cumulative z-component specific angular momentum of cluster AB stars. The red line shows stars that originally belonged to cluster A, and the blue line shows stars that originally belonged to cluster B.

and z follow a similar trend by becoming positive and decreasing slowly until the end of the simulation. This implies that the expansion is slowing down after the merger along all three axes. The expansion rates at the end of the simulation can be seen as the slopes of the lines of best fit in the bottom panels of Figure 3.4. These values are in the similar range to those found for open clusters along the plane of the sky (Wright et al. 2023).

Stars belonging to cluster AB gain angular momentum about the centre of mass of the stellar component of cluster AB from the merger of cluster A and B. The z-component of angular momentum peaks during the merger due to the counter-clockwise rotation of the stars in the x-y plane. It decreases slowly for the remainder of the simulation. The majority of the specific angular momentum inherited from this merger is in the inner regions (within $\approx 3L_{50}$) of the cluster. We show an example of this in Figure 3.5. Such a trend with rotation amplitude has been observed in intermediate age star clusters (e.g. Mackey et al. 2013). As well, we find a difference in the distribution of specific angular momentum for the stars originally belonging to cluster A and those originally belonging to cluster B in the outer regions of cluster AB similar to the result found by Lahén et al. (2020). Lastly, we find that not all stars have the same direction of angular momentum. We discuss this more in Section 3.6.

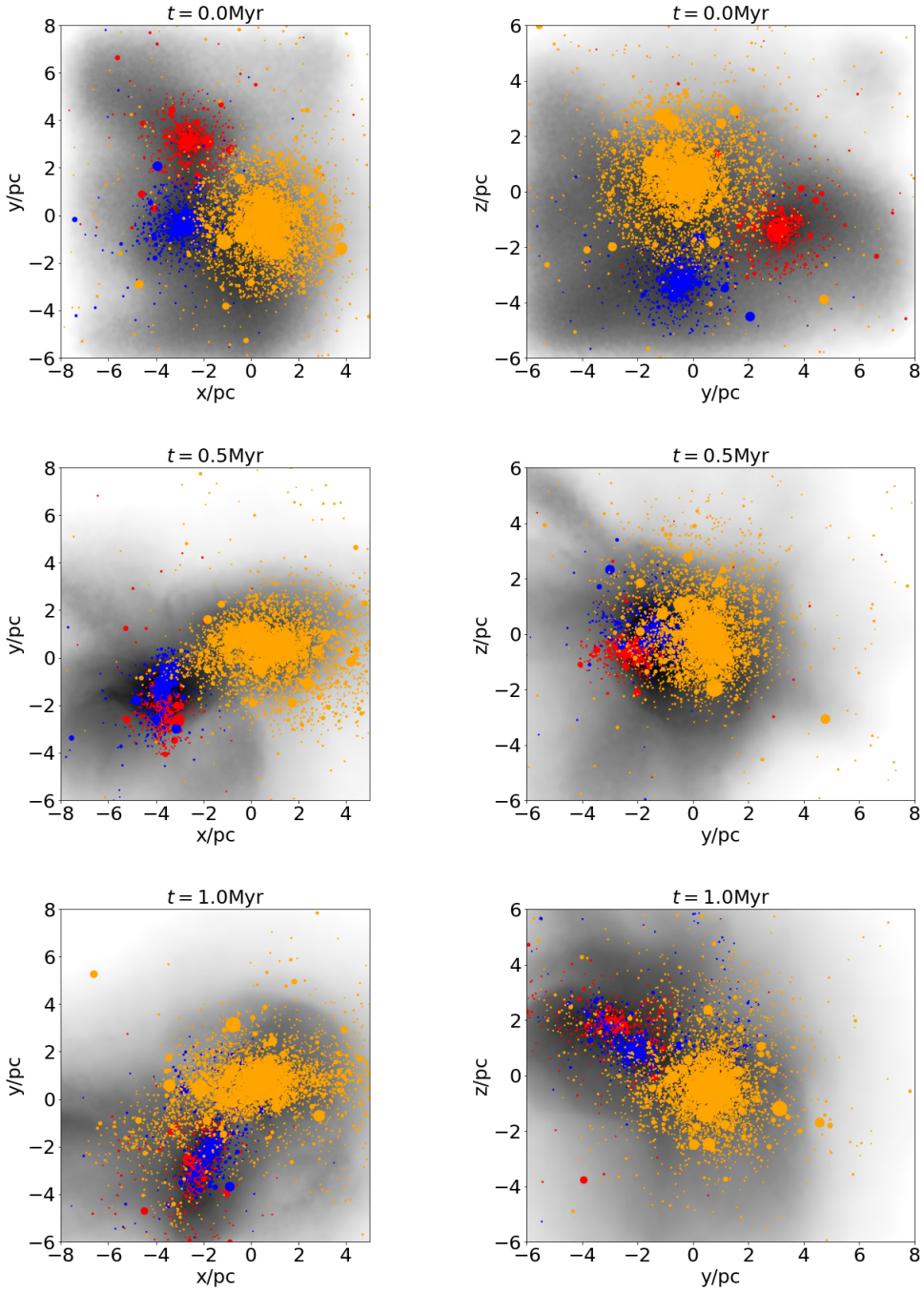

FIGURE 3.6: Same as Figure 3.1 but for the `region2` simulation. The lowest and highest mass stars in this simulation are $0.15M_{\odot}$ and $98.34M_{\odot}$ respectively.

3.4.2 Region 2

We now discuss the evolution of the stellar components of the clusters present in the `region2` simulation outlined in Table 3.1. We show snapshots of the distribution of stars and gas present in a portion of this simulation in Figure 3.6. The circles are colour-coded depending on the cluster to which they initially belong with red, blue, and orange corresponding to clusters A, B, and C respectively. Initially, clusters A and B are travelling towards one another in the x-y plane.

At t$\approx$ 0.4Myr, cluster A has begun merging with cluster B. The impact parameter of this merger is $1.9\mathrm{L}_{50,\mathrm{B}}$ where $\mathrm{L}_{50,\mathrm{B}}$ is the 50% Lagrangian radius of cluster B. At this point stars from cluster C begin moving towards the merged cluster due to the increased potential felt. As a result, the merged cluster accretes an extra $\approx 300\mathrm{M}_{\odot}$ from cluster C by the end of the simulation. We call this final resultant cluster "cluster ABc". Because only $\approx 1\%$ of the stellar mass becomes unbound by the end of the simulation, the total mass of the cluster ABc increases beyond the sum of the masses of cluster A and B.

3.4.2.1 Velocity Space Distribution

Similarly to the stars in the `region1` simulation, the merger of cluster A and cluster B results in a sharp and temporary increase in the velocity dispersion of the stars involved during the merger. The virial parameter of the merged cluster is $\alpha = 0.51$ by the end of the simulation indicating that cluster ABc is bound.

The stars originally belonging to clusters A and B are mixed in velocity space by the end of the simulation similarly to the `region1` simulation. The stars accreted onto the merged cluster from cluster C are mixed in velocity space with the rest of the stars belonging to cluster ABc by the end of the simulation. It would therefore be difficult to determine whether stars in this cluster were accreted from a nearby cluster using their distribution in velocity space.

3.4.2.2 Expansion and Rotation

The 50%, 75% and 90% Lagrangian radii of cluster ABc all increase after the merger. This increase stops by the end of the simulation. We find a positive expansion rate in the stellar component of cluster ABc along the x and y axes at the end of the simulation. There is no clear signal of expansion along the z-axis. The values of the expansion rates are 0.19 ± 0.02, and 0.14 ± 0.04 $\mathrm{kms}^{-1}\mathrm{pc}^{-1}$ along the x and y axes respectively at the end of the simulation. These expansion rates are much lower than those found along all

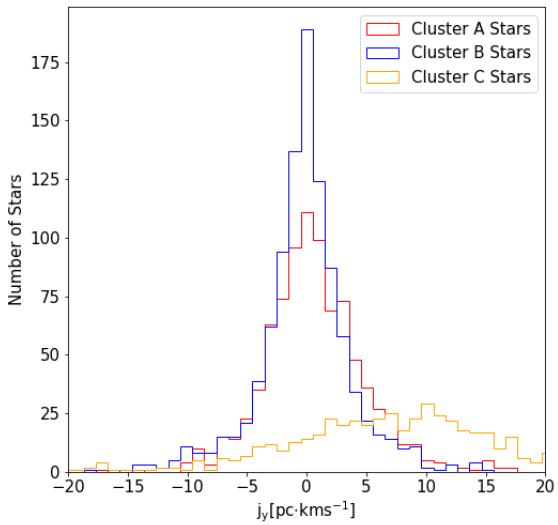

FIGURE 3.7: Distribution of y-component specific angular momentum of all stars in cluster ABc at the end of the `region2` simulation. Red, blue, and orange lines show stars which originally belonged to cluster A, B, and C respectively.

axes in cluster AB in the `region1` simulation. This could be due to the strong potential which results from the high mass in stars and gas present in the `region2` simulation. The small expansion that is present around cluster ABc in this simulation is anisotropic similar to that found in cluster AB in the `region1` simulation.

We see small changes to the shape and size of cluster C as a result of the stripped stars and the gravitational effect of the nearby cluster ABc. The presence of contraction or expansion along only two of the three axes as we see in clusters ABc and C in this simulation implies that the shape of the stellar component of the clusters has changed to become less spherical. This is consistent with results presented in Cournoyer-Cloutier et al. (2023) who find that cluster mergers can cause clusters to become more elliptical.

There is angular momentum in the stellar component of cluster ABc. Stars that are now part of cluster ABc but originally belonged to clusters A, B, or C all share a similar distribution of x-component specific angular momentum. Along both the y and z axes, we find that most of the angular momentum comes from the accreted stars. We show an example of this for the y-component of the specific angular momentum in Figure 3.7. Stars that originally belonged to cluster C have more total y-component specific

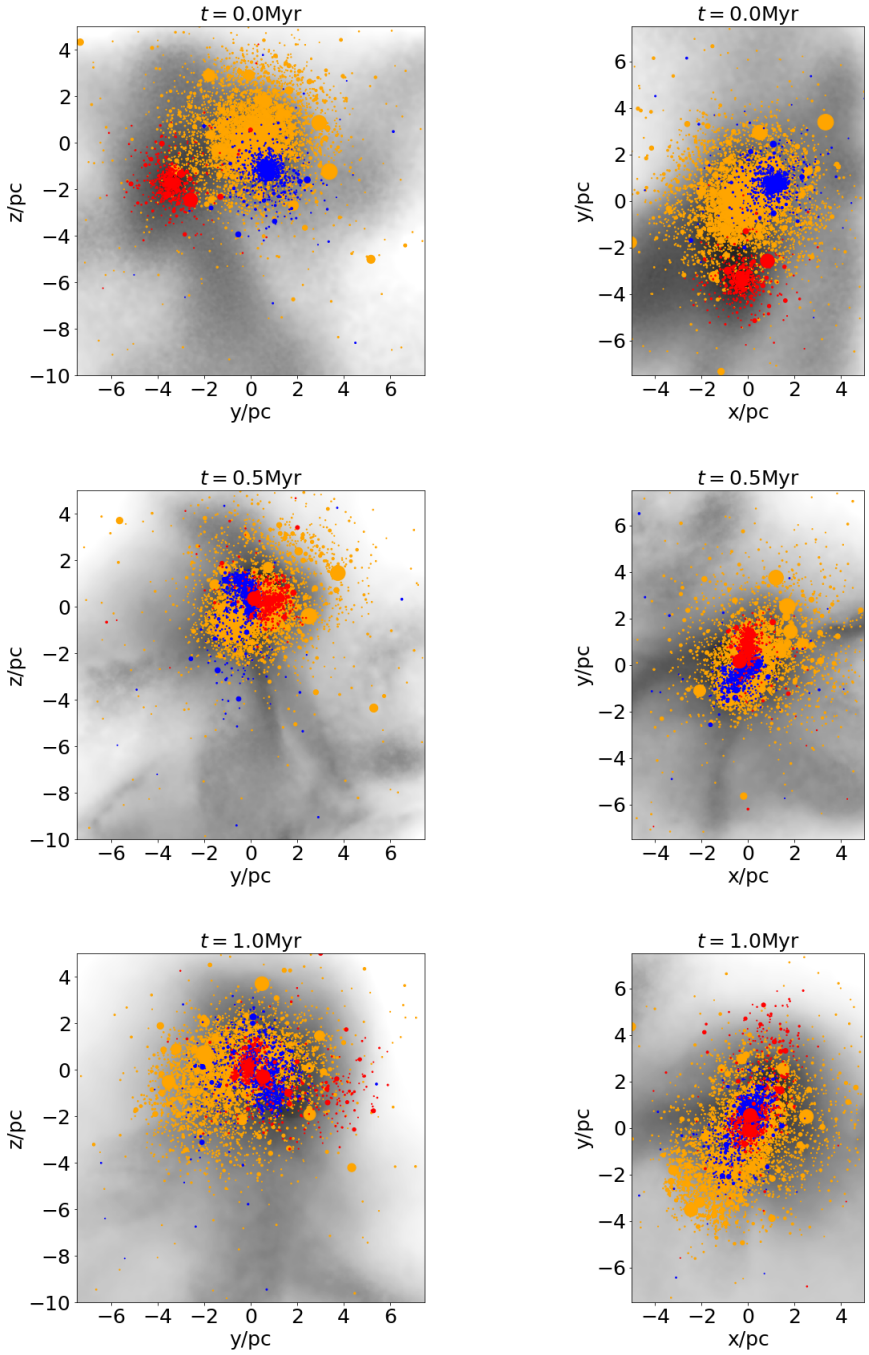

FIGURE 3.8: Same as Figure 3.1 but for the `region3` simulation. The lowest and highest mass stars in this simulation are $0.15M_{\odot}$ and $74.59M_{\odot}$ respectively.

angular momentum than stars that originally belonged to clusters A or B. Accretion from surrounding clusters can be important in inducing angular momentum onto the clusters that are accreting. Because of the high specific angular momentum of the accreted stars in the outskirts of cluster ABc, the distribution of angular momentum does not have a concentration within $3L_{50}$ as it did in cluster AB from the `region1` simulation.

3.4.3 Region3

We now discuss the evolution of the stellar components of the clusters in the `region3` simulation. We show snapshots of a portion of this simulation in Figure 3.8. In this simulation, both the red and blue coloured clusters (clusters A and B respectively), are initially moving clockwise around the much more massive orange coloured cluster (cluster C) in the y-z and x-y planes. After $\approx$ 0.2Myr, both cluster A and cluster B have merged with cluster C. We call the final resultant cluster "cluster ABC". The impact parameters of the mergers of cluster A and cluster B with cluster C are $1.1L_{50,C}$ and $0.7L_{50,C}$ respectively where $L_{50,C}$ is the 50% Lagrangian radius of cluster C.

The mergers result in <0.05% of the total stellar mass becoming unbound from cluster ABC by the end of the simulation.

3.4.3.1 Velocity Space Distribution

Similarly to the mergers in the `region1` and `region2` simulations, we find that the merger of clusters A and B with cluster C results in a sharp, but temporary, increase in the velocity dispersion of the stars. After $\approx$ 0.5Myr, the velocity dispersion decreases down to $\approx 8\text{kms}^{-1}$. The virial parameter of cluster ABC at the end of the simulation is $\alpha = 0.74$ indicating that the cluster is bound. After the mergers, the stars from all three clusters have mixed in velocity space similarly to the `region1` and `region2` simulations.

3.4.3.2 Expansion and Rotation

For a short time after the mergers of clusters A and B with cluster C in the `region3` simulation, we see signatures of contraction. The 90% and 75% Lagrangian radii are decreasing for $\approx$0.6Myr after the merger. After this time, they are increasing until the end of the simulation. Below the 75% Lagrangian radii, we do not see signatures of expansion or contraction indicating that the expansion and contraction are mostly present in the outer regions of the cluster.

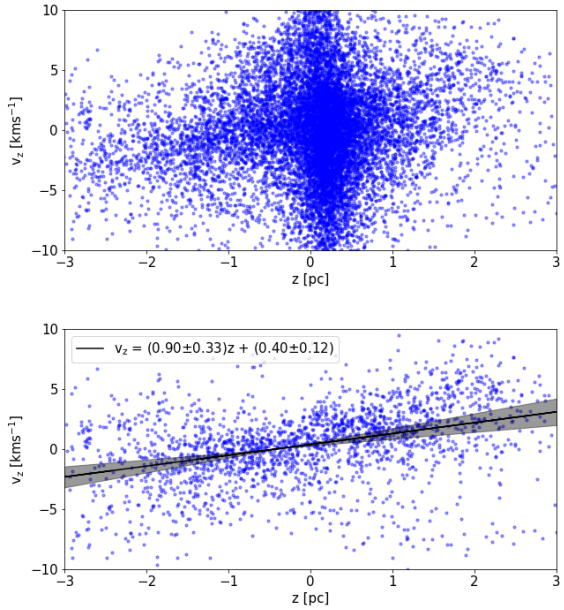

FIGURE 3.9: Position-velocity distribution of stars in cluster ABC from the `region3` simulation along the z-axis at the end of the simulation. Top panel shows all stars, and bottom panel shows all stars between the 75% and 90% Lagrangian radii of the cluster. The black line in the bottom panel shows the line of best fit with the shaded regions showing one sigma of the fit calculated through bootstrapping 10^5 times.

This can also be seen in the distribution of the cluster ABC stars in position-velocity space. An example is shown in Figure 3.9. In the top panel, we show the distribution of all stars in position-velocity space along the z axis at the end of the simulation. From this, we see no clear signature of expansion. The bottom panel of Figure 3.9 shows the position-velocity distribution along the z axis of stars between 75% and 90% Lagrangian radii of cluster ABC at the same time. Here, we see a higher linear correlation implying that the expansion signature is stronger when considering these stars. When considering stars beyond the 90% Lagrangian radius, we find that the expansion signature decreases. The same thing is true when we consider stars within the 75% Lagrangian radius. We find similar trends when looking along the x and y axes. As well, we find that the expansion is much more anisotropic along the x and y axes than it is along the z-axis with most of the expansion taking place along the negative x and y axes.

There is negative x-component angular momentum induced in cluster ABC stars after the mergers. As the stars belonging to cluster A and B rotate around cluster C, they impart angular momentum on the initially non-rotating stellar component of cluster C. As well, we find that not all stars are rotating clockwise consistent with the merger direction. This is similar to the previous simulations in this section. The angular momentum of cluster ABC is concentrated within $\approx 3L_{50}$.

3.5 Zoom-In Regions: Gas

In all three zoom-in simulations, we find that the amount of unbound gas mass is negligible throughout the simulations. In all cases, the amount of unbound gas is less than that from the merger simulations presented in Paper I and in Section 3.3 likely because of the background gas distribution providing pressure to keep gas bound to the cluster (see Paper II).

We find that the amount of gas with densities above 10^4 and $10^5 \mathrm{cm}^{-3}$ increases from the merger processes in all three zoom-in simulations. These increases last for $\approx$2 free-fall times for the gas at that density threshold. After this, they decrease back down to their original values. The amount of gas above $10^3 \mathrm{cm}^{-3}$ stays constant for most of the simulation for all three simulations. We show an example of this behaviour in the `region1` simulation in Figure 3.10. In our simulations that did not include a background gas component, we found that the amount of dense gas decreases below its original value by the end of the simulation. This illustrates another important property

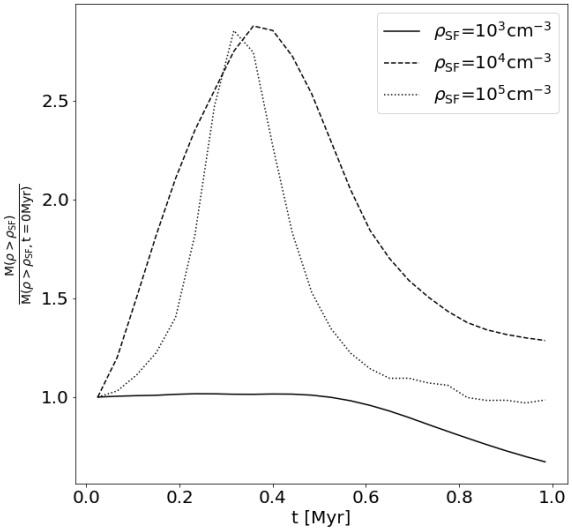

FIGURE 3.10: Change in the total mass of gas above 10^3cm^{-3} (solid), 10^4cm^{-3} (dashed) and 10^5cm^{-3} (dotted) for all gas in the `region1` simulation.

of the background gas: its presence may help in promoting star formation through cluster mergers.

At the beginning of the mergers in all three simulations, we see a bridge of gas with density above 10^4cm^{-3} connecting the cores of the clusters involved in the merger. We expect that the newly formed stars will mix with the rest of the stars in the cluster one free-fall time later because the bridge of star forming gas connecting the two cores has shrunk.

In velocity space, at the beginning of the merger, we find that the distributions of stars and gas look different from each other. In the `region1` and `region2` simulations, the distributions of the stars in velocity space are mostly flat. The gas however, is peaked around the centre of mass velocity of the merged cluster in each simulation. Such a strong distinction between the distributions of the stars and gas in velocity space is not present in the `region3` simulation. We discuss the implications of this in Section 3.6.

Converse to the velocity space distribution of stars and gas in our simulations, the distributions of specific angular momentum are similar between the stars and gas after

the mergers in each simulation. The peaks in the specific angular momentum distributions of the stars overlap the peaks in the specific angular momentum distributions of the gas in the `region1` and `region2` simulations. In the `region3` simulations, differences between the stellar and gas distribution in specific angular momentum space are not strong.

3.6 Summary and Discussion

We have analyzed the role played by the impact parameter in the merging of two gas-rich star clusters, and how environment affects the dynamics of merging clusters. We have done this through a combination of off-axis merger simulations that do not include a background gas component, and simulations that zoom into a previously run GMC simulation from Howard et al. (2018) (H18). The impact parameter of a merger can have a small role in determining the amount of bound stars and gas the resultant cluster can maintain. High impact parameters can also reduce the collisional velocity necessary to produce a non-monolithic resultant cluster. However, our zoom-in simulations show that background gas is a very important component in driving the motions of clusters as they merge. It also helps keep clusters monolithic. The dynamics of the stars are affected by the merger process. Velocity dispersions of the stars involved in the mergers increase as a result of the merger, and the stars completely mix in velocity space shortly after the merger finishes. Mergers also induce expansion and angular momentum in the stellar component of the resultant cluster. This expansion is anisotropic in all zoom-in simulations studied in this work. The angular momentum of the stellar component is concentrated in the inner regions of the resultant cluster unless that cluster accretes stars from a nearby cluster. Mergers increase the amount of potentially star-forming dense gas present in the cluster when a background gas distribution is included.

We have found that the presence of background gas is extremely important in determining the motion of clusters that are embedded inside GMCs. Through feedback and star formation, the mass in gas inside a star forming GMC decreases while the mass in stars increases (e.g. Li et al. 2019, Fujii et al. 2021). In the context of our simulations, this implies that mergers between clusters inside GMCs may become less monolithic with time.

The sink particle prescription outlined in Federrath et al. (2010) does not allow for sinks to lose mass. From our results, we find that mergers of clusters inside the GMC environment result in a negligible amount of unbound material implying that this

component of the sink particle prescription holds in our simulations. Sinks can only gain mass through mergers with other sinks and gas accretion. This results in a discrepancy between our `region2` simulation, and its sink particle analog because of the accretion of stars from cluster C onto the merged cluster. The spatial distribution of stars in a cluster should be considered in sink particle prescriptions.

The expansion of the stellar component we see in our clusters is different from expansion observed in star clusters after they have removed their gas component through feedback. For embedded clusters, expansion is expected as gas is being removed from the cluster through feedback effects because of the drastic decrease in the potential of the system (e.g. Pelupessy and Portegies Zwart 2012, Pfalzner and Kaczmarek 2013, Farias et al. 2023, Arunima et al. 2023). In particular, Pelupessy and Portegies Zwart (2012) show that through gas expulsion the 50, 75, and 90% Lagrangian radii are all expected to grow well after the initial expansion from gas loss. In our `region1` and `region2` simulations, the 50% and 75% Lagrangian radii of the merged clusters plateau after some initial growth likely because the potential from the background gas is still present. As well, the expansion found in Pelupessy and Portegies Zwart (2012) was accompanied by a drastic loss in bound stellar mass which we do not see in any of our simulations.

We also see that the expansion of all of our merged clusters is anisotropic. While the observations performed by Wright et al. (2023) have found anisotropic expansion around embedded young clusters, most observations are limited to clusters that have dispersed their natal gas clouds. It is therefore important to test whether the anisotropy of the expansion found in our simulations remains as the cluster expands its surrounding gas component.

The simulations from H18 show that clusters merge many times during their embedded phase. These mergers happened on average once every ≈0.4Myr. As we have seen from our simulations, not all stars have angular momentum in the same direction around the centre of mass of the cluster. This is expected to persist as clusters build up and merge throughout the GMCs life.

We can predict the number of stars expected to form from the dense gas present in our simulations by considering a star formation efficiency per free-fall time of $\epsilon_{\rm ff} = 3\%$ that matches recent observations of star forming molecular clouds (Pokhrel et al. 2021). Using this value we find that the stars that form from the dense gas in the `region1` and `region2` simulations will affect the overall distribution of stars in velocity space making it more peaked around the centre of mass velocity of the resultant cluster. Therefore, clusters

may be able to develop stellar age gradients associated with kinematic subgroups as as they evolve. This is similar to those observed within subgroups in older OB associations (e.g. Pecaut and Mamajek 2016, Briceño-Morales and Chanamé 2023). In the `region3` simulation, because the number of stars belonging to cluster ABC is so large, we predict that the newly formed stars will have very little effect on the overall distribution in position, velocity, or angular momentum space. This implies that mergers that involve clusters consisting of a high mass stellar component may not create easily detectable gradients in age or kinematic subgroups. Because of the high mass in gas present in GMCs early on in their evolution, we expect mergers that take place early on in the GMCs life to lead to more noticeable kinematic and age distinctions in stars. To fully understand observations of phase space subgroups in clusters and associations, we must consider multiple subcluster mergers, and employ realistic star formation and feedback prescriptions.

Bibliography

Aarseth, S. J. (1974). Dynamical evolution of simulated star clusters. I. Isolated models., A&A **35**(2): 237–250.

Ali, A. A., Dobbs, C. L., Bending, T. J. R., Buckner, A. S. M. and Pettitt, A. R. (2023). Star cluster formation and feedback in different environments of a Milky Way-like galaxy, MNRAS **524**(1): 555–568.

Arunima, A., Pfalzner, S. and Govind, A. (2023). Unbound stars hold the key to young star cluster history, A&A **670**: A128.

Barnes, J. and Hut, P. (1986). A hierarchical O(N log N) force-calculation algorithm, *Nature Astronomy* **324**(6096): 446–449.

Baumgardt, H. and Kroupa, P. (2007). A comprehensive set of simulations studying the influence of gas expulsion on star cluster evolution, MNRAS **380**(4): 1589–1598.

Bellazzini, M., Bragaglia, A., Carretta, E., Gratton, R. G., Lucatello, S., Catanzaro, G. and Leone, F. (2012). Na-O anticorrelation and HB. IX. Kinematics of the program clusters A link between systemic rotation and HB morphology?, A&A **538**: A18.

Bianchini, P., van der Marel, R. P., del Pino, A., Watkins, L. L., Bellini, A., Fardal, M. A., Libralato, M. and Sills, A. (2018). The internal rotation of globular clusters revealed by Gaia DR2, MNRAS **481**(2): 2125–2139.

Bonilla-Barroso, A., Ballesteros-Paredes, J., Hernández, J., Aguilar, L., Zamora-Avilés, M., Hartmann, L. W., Kuznetsova, A., Camacho, V. and Lora, V. (2022). Gravity or turbulence V: star-forming regions undergoing violent relaxation, MNRAS **511**(4): 4801–4814.

Briceño-Morales, G. and Chanamé, J. (2023). Substructure, supernovae, and a time-resolved star formation history for Upper Scorpius, MNRAS **522**(1): 1288–1309.

Chen, Y., Li, H. and Vogelsberger, M. (2021). Effects of initial density profiles on massive star cluster formation in giant molecular clouds, MNRAS **502**(4): 6157–6169.

Cournoyer-Cloutier, C., Sills, A., Harris, W. E., Appel, S. M., Lewis, S. C., Polak, B., Tran, A., Wilhelm, M. J. C., Mac Low, M.-M., McMillan, S. L. W. and Portegies Zwart, S. (2023). Early evolution and three-dimensional structure of embedded star clusters, MNRAS **521**(1): 1338–1352.

Della Croce, A., Dalessandro, E., Livernois, A. R. and Vesperini, E. (2023). Young, wild and free: the early expansion of star clusters, *arXiv e-prints* p. arXiv:2312.02263.

Dobbs, C. L., Bending, T. J. R., Pettitt, A. R. and Bate, M. R. (2022). The formation of massive stellar clusters in converging galactic flows with photoionization, MNRAS **509**(1): 954–973.

Elmegreen, B. G. (2001). Star Formation from Galaxies to Globules, *American Astronomical Society Meeting Abstracts*, Vol. 199 of *American Astronomical Society Meeting Abstracts*, p. 42.01.

Enoch, M. L., Evans, Neal J., I., Sargent, A. I., Glenn, J., Rosolowsky, E. and Myers, P. (2008). The Mass Distribution and Lifetime of Prestellar Cores in Perseus, Serpens, and Ophiuchus, ApJ **684**(2): 1240–1259.

Ester, M., Kriegel, H.-P., Sander, J. and Xu, X. (1996). A Density-Based Algorithm for Discovering Clusters in Large Spatial Databases with Noise, *Second International Conference on Knowledge Discovery and Data Mining (KDD'96). Proceedings of a conference held August 2-4*, pp. 226–331.

Fahrion, K. and De Marchi, G. (2023). The hierarchical formation of 30 Doradus as seen by JWST, *arXiv e-prints* p. arXiv:2311.06336.

Farias, J. P., Offner, S. S. R., Grudić, M. Y., Guszejnov, D. and Rosen, A. L. (2023). Stellar Populations in STARFORGE: The Origin and Evolution of Star Clusters and Associations, *arXiv e-prints* p. arXiv:2309.11415.

Federrath, C., Banerjee, R., Clark, P. C. and Klessen, R. S. (2010). Modeling Collapse and Accretion in Turbulent Gas Clouds: Implementation and Comparison of Sink Particles in AMR and SPH, ApJ **713**(1): 269–290.

Fryxell, B., Olson, K., Ricker, P., Timmes, F. X., Zingale, M., Lamb, D. Q., MacNeice, P., Rosner, R., Truran, J. W. and Tufo, H. (2000). FLASH: An Adaptive Mesh Hydrodynamics Code for Modeling Astrophysical Thermonuclear Flashes, ApJS **131**(1): 273–334.

Fujii, M., Iwasawa, M., Funato, Y. and Makino, J. (2007). BRIDGE: A Direct-Tree Hybrid N-Body Algorithm for Fully Self-Consistent Simulations of Star Clusters and Their Parent Galaxies, *PASJ* **59**: 1095.

Fujii, M. S., Saitoh, T. R., Hirai, Y. and Wang, L. (2021). SIRIUS project. III. Star-by-star simulations of star cluster formation using a direct N-body integrator with stellar feedback, PASJ **73**(4): 1074–1099.

Geyer, M. P. and Burkert, A. (2001). The effect of gas loss on the formation of bound stellar clusters, MNRAS **323**(4): 988–994.

Hénault-Brunet, V., Gieles, M., Evans, C. J., Sana, H., Bastian, N., Maíz Apellániz, J., Taylor, W. D., Markova, N., Bressert, E., de Koter, A. and van Loon, J. T. (2012). The VLT-FLAMES Tarantula Survey. VI. Evidence for rotation of the young massive cluster R136, A&A **545**: L1.

Howard, C. S., Pudritz, R. E. and Harris, W. E. (2018). A universal route for the formation of massive star clusters in giant molecular clouds, *Nature Astronomy* **2**: 725–730.

Karam, J. and Sills, A. (2022). Modelling star cluster formation: mergers, MNRAS **513**(4): 6095–6104.

Karam, J. and Sills, A. (2023). Modelling star cluster formation: Gas accretion, MNRAS **521**(4): 5557–5569.

Kounkel, M., Stassun, K. G., Covey, K. and Hartmann, L. (2022). A gravitational and dynamical framework of star formation: the Orion nebula, MNRAS **517**(1): 161–174.

Kroupa, P. (2001). On the variation of the initial mass function, MNRAS **322**(2): 231–246.

Kuhn, M. A., Hillenbrand, L. A., Feigelson, E. D., Fowler, I., Getman, K. V., Broos, P. S., Povich, M. S. and Gromadzki, M. (2022). The Effect of Molecular Cloud Properties on the Kinematics of Stars Formed in the Trifid Region, ApJ **937**(1): 46.

Kuhn, M. A., Hillenbrand, L. A., Sills, A., Feigelson, E. D. and Getman, K. V. (2019). Kinematics in Young Star Clusters and Associations with Gaia DR2, ApJ **870**(1): 32.

Lada, C. J., Forbrich, J., Lombardi, M. and Alves, J. F. (2012). Star Formation Rates in Molecular Clouds and the Nature of the Extragalactic Scaling Relations, ApJ **745**(2): 190.

Lada, C. J. and Lada, E. A. (2003). Embedded Clusters in Molecular Clouds, *Annual Reviews of* A&A **41**: 57–115.

Lahén, N., Naab, T., Johansson, P. H., Elmegreen, B., Hu, C.-Y. and Walch, S. (2020). Structure and Rotation of Young Massive Star Clusters in a Simulated Dwarf Starburst, ApJ **904**(1): 71.

Li, H., Vogelsberger, M., Marinacci, F. and Gnedin, O. Y. (2019). Disruption of giant molecular clouds and formation of bound star clusters under the influence of momentum stellar feedback, MNRAS **487**(1): 364–380.

Lim, B., Hong, J., Lee, J., Yun, H.-S., Hwang, N. and Park, B.-G. (2023). The Kinematics of the Young Stellar Population in the W5 Region of the Cassiopeia OB6 Association: Implication for the Formation Process of Stellar Associations, AJ **166**(3): 97.

Lyden-Bell, D. (1967). Statistical mechanics of violent relaxation in stellar systems, *Monthly Notices of the Astronomical Society* **136**: 101.

Mackey, A. D., Da Costa, G. S., Ferguson, A. M. N. and Yong, D. (2013). A VLT/FLAMES Study of the Peculiar Intermediate-age Large Magellanic Cloud Star Cluster NGC 1846. I. Kinematics, ApJ **762**(1): 65.

Makino, J. and Aarseth, S. J. (1992). On a Hermite Integrator with Ahmad-Cohen Scheme for Gravitational Many-Body Problems, *PASJ* **44**: 141–151.

Pecaut, M. J. and Mamajek, E. E. (2016). The star formation history and accretion-disc fraction among the K-type members of the Scorpius-Centaurus OB association, MNRAS **461**(1): 794–815.

Pedregosa, F., Varoquaux, G., Gramfort, A., Michel, V., Thirion, B., Grisel, O., Blondel, M., Müller, A., Nothman, J., Louppe, G., Prettenhofer, P., Weiss, R., Dubourg, V.,

Vanderplas, J., Passos, A., Cournapeau, D., Brucher, M., Perrot, M. and Duchesnay, É. (2011). Scikit-learn: Machine Learning in Python, *Journal of Machine Learning Research* **12**: 2825–2830.

Pelupessy, F. I. and Portegies Zwart, S. (2012). The evolution of embedded star clusters, MNRAS **420**(2): 1503–1517.

Pelupessy, F. I., van Elteren, A., de Vries, N., McMillan, S. L. W., Drost, N. and Portegies Zwart, S. F. (2013). The Astrophysical Multipurpose Software Environment, A&A **557**: A84.

Pfalzner, S. and Kaczmarek, T. (2013). The expansion of massive young star clusters - observation meets theory, A&A **559**: A38.

Plummer, H. C. (1911). On the problem of distribution in globular star clusters, MNRAS **71**: 460–470.

Pokhrel, R., Gutermuth, R. A., Krumholz, M. R., Federrath, C., Heyer, M., Khullar, S., Megeath, S. T., Myers, P. C., Offner, S. S. R., Pipher, J. L., Fischer, W. J., Henning, T. and Hora, J. L. (2021). The Single-cloud Star Formation Relation, ApJ **912**(1): L19.

Portegies Zwart, S. F., McMillan, S. L. W. and Gieles, M. (2010). Young Massive Star Clusters, *Annual Reviews of* A&A **48**: 431–493.

Portegies Zwart, S., McMillan, S., Harfst, S., Groen, D., Fujii, M., Nualláin, B. Ó., Glebbeek, E., Heggie, D., Lombardi, J., Hut, P., Angelou, V., Banerjee, S., Belkus, H., Fragos, T., Fregeau, J., Gaburov, E., Izzard, R., Jurić, M., Justham, S., Sottoriva, A., Teuben, P., van Bever, J., Yaron, O. and Zemp, M. (2009). A multiphysics and multiscale software environment for modeling astrophysical systems, *New Astronomy* **14**(4): 369–378.

Portegies Zwart, S., McMillan, S. L. W., van Elteren, E., Pelupessy, I. and de Vries, N. (2013). Multi-physics simulations using a hierarchical interchangeable software interface, *Computer Physics Communications* **184**(3): 456–468.

Rey-Raposo, R., Dobbs, C. and Duarte-Cabral, A. (2015). Are turbulent spheres suitable initial conditions for star-forming clouds?, MNRAS **446**: L46–L50.

Rieder, S., Dobbs, C., Bending, T., Liow, K. Y. and Wurster, J. (2022). The formation and early evolution of embedded star clusters in spiral galaxies, MNRAS **509**(4): 6155–6168.

Sander, J., Ester, M., Kriegel, H.-P. and Xu, X. (1998). Density-Based Clustering in Spatial Databases: The Algorithm GDBSCAN and Its Applications, *Data Mining and Knowledge Discovery* **2**(2): 169.

Springel, V. (2005). The cosmological simulation code GADGET-2, MNRAS **364**(4): 1105–1134.

Vázquez-Semadeni, E., González-Samaniego, A. and Colín, P. (2017). Hierarchical star cluster assembly in globally collapsing molecular clouds, MNRAS **467**(2): 1313–1328.

Wright, N. J., Jeffries, R. D., Jackson, R. J., Bayo, A., Bonito, R., Damiani, F., Kalari, V., Lanzafame, A. C., Pancino, E., Parker, R. J., Prisinzano, L., Randich, S., Vink, J. S., Alfaro, E. J., Bergemann, M., Franciosini, E., Gilmore, G., Gonneau, A., Hourihane, A., Jofré, P., Koposov, S. E., Lewis, J., Magrini, L., Micela, G., Morbidelli, L., Sacco, G. G., Worley, C. C. and Zaggia, S. (2019). The Gaia-ESO Survey: asymmetric expansion of the Lagoon Nebula cluster NGC 6530 from GES and Gaia DR2, MNRAS **486**(2): 2477–2493.

Wright, N. J., Jeffries, R. D., Jackson, R. J., Sacco, G. G., Arnold, B., Franciosini, E., Gilmore, G., Gonneau, A., Morbidelli, L., Prisinzano, L., Randich, S. and Worley, C. C. (2023). The Gaia-ESO Survey: 3D dynamics of young groups and clusters from GES and Gaia EDR3, *arXiv e-prints* p. arXiv:2311.08358.

Wright, N. J. and Mamajek, E. E. (2018). The kinematics of the Scorpius-Centaurus OB association from Gaia DR1, MNRAS **476**(1): 381–398.

Chapter 4

Dynamics of Star Cluster Buildup with Stellar Feedback and Star Formation

The content of this chapter is a second revision of the manuscript text for publication under the following citation:

Karam, J., Fujii, M. S., & Sills, A. (2025). Dynamics of Star Cluster Formation: The Effects of Ongoing Star Formation and Stellar Feedback. The Astrophysical Journal, 984, 75.

The above article was corrected in:

Karam, J., Fujii, M. S., & Sills, A. (2025). Erratum: Dynamics of Star Cluster Formation: The Effects of Ongoing Star Formation and Stellar Feedback. The Astrophysical Journal, 987, 102.

Dynamics of Star Cluster Formation: The Effects of Ongoing Star Formation and Stellar Feedback

Jeremy Karam
Department of Physics and Astronomy
McMaster University, Hamilton, ON, Canada
Email: karamj2@mcmaster.ca

Michiko S. Fujii
Department of Astronomy
The University of Tokyo, Hongo, Bunkyo-ku, Tokyo, Japan
Email: fujii@astron.s.u-tokyo.ac.jp

Alison Sills
Department of Physics and Astronomy
McMaster University, Hamilton, ON, Canada
Email: asills@mcmaster.ca

Abstract

We perform a high resolution zoom-in simulation of star cluster assembly including the merger of two sub-clusters with initial conditions taken from previous large scale giant molecular cloud (GMC) simulations. We couple hydrodynamics to N-body dynamics to simulate the individual stars themselves, and the gas-rich environment in which they evolve. We include prescriptions for star formation and stellar feedback and compare directly to previous simulations of the same region without these prescriptions to determine their role in shaping the dynamics inherited from the cluster assembly process. The stellar mass of the cluster grows through star formation within the cluster and accretion of new stars and star forming gas from a nearby filament. This growth results in an enhancement in the cluster's rotation and anisotropic expansion compared to simulations without star formation. We also analyze the internal kinematics of the cluster once it has lost most of its gas and find that the rotational velocity and the velocity anisotropy

profiles are qualitatively similar to those expected of clusters that have undergone violent relaxation. As well, rotation and anisotropic expansion are still present by the time of gas removal. This implies that evolution within the GMC was unable to completely erase the kinematics inherited by the merger.

Keywords: *Star Clusters (1567) — Star Formation (1569) — Stellar Dynamics (1596) — Hydrodynamics (1963)*

4.1 Introduction

Simulations show that star cluster formation is a hierarchical process involving the mergers of smaller star clusters into larger ones while embedded inside giant molecular clouds (GMCs) (e.g. Howard et al. 2018, Chen et al. 2021, Rieder et al. 2022). Observationally, one cannot pierce through the extinction caused by GMC gas to see the stars themselves, so evidence for hierarchical star cluster buildup comes from dynamical studies of star clusters that have recently removed their surrounding gas through a combination of stellar feedback and star formation. For example, observations of cluster age gradients (e.g. Fahrion and De Marchi 2023), asymmetric dynamics (e.g. Wright and Mamajek 2018, Wright et al. 2019, Wright et al. 2024, Armstrong and Tan 2024), and preferential directions of high velocity (runaway) stars (e.g. Polak et al. 2024, Stoop et al. 2024) are interpreted as dynamical signatures of mergers as a build up mechanism for star clusters (e.g. Schoettler et al. 2022, Lahén et al. 2024, Karam and Sills 2024, Cournoyer-Cloutier et al. 2024). To completely draw this connection between star cluster formation inside GMCs and the observations of star clusters after they have left their natal cloud, it is important to clearly understand all of the complexities associated with star cluster build up and the environment within which it takes place.

As star clusters merge inside a GMC, gas around them becomes compressed and can go on to form new stars (Karam and Sills 2022, Fujii et al. 2022). New star formation, coupled with the increase in mass from the merger of two clusters can increase the mass of clusters involved in the merger. However, mergers can also result in the ejection of stars from their host cluster (Karam and Sills 2022) and cluster splitting (Dobbs, Bending, Pettitt, Buckner and Bate 2022) which both lead to a decrease in the total cluster mass implying a complex change to the cluster dynamics throughout its assembly. The formation of new stars from cluster mergers may also offer an explanation for the age gradients observed in many clusters and associations, but the origin of the kinematic

substructure among these groups (e.g. Cantat-Gaudin et al. 2019, Zari et al. 2019, Briceño-Morales and Chanamé 2023) is still unclear. It has been shown that kinematic distinction may arise from new stars inheriting motions from dense gas (Ordenes-Huanca et al. 2024) but it is uncertain whether this distinction remains after the surrounding gas distribution has been altered by stellar feedback. Regarding the role played by stellar feedback, Lewis et al. (2023) showed that feedback from massive stars can not only alter the amount of star formation present throughout a GMC, but also the spatial distribution of resultant clusters. Similarly, Dobbs, Bending, Pettitt and Bate (2022) found that the rate of hierarchical cluster buildup can change depending on environment inside a star forming spiral galaxy implying that feedback may be able to alter the efficiency of star cluster assembly inside a GMC. As pre-SNe feedback has been shown to be dominant in removing gas from GMCs and altering the environment (e.g. Deshmukh et al. 2024), it is likely to have an effect on the dynamics of clusters as star formation is ongoing.

A key component to the morphology of the gaseous environment of star forming regions is dense filaments (see Hacar et al. 2023 for a review). These filaments are found around young clusters in the form of hub filament systems (e.g. Wong et al. 2022, Kumar et al. 2022, Dewangan et al. 2024, Seshadri et al. 2024, Rawat et al. 2024, Zhang, Andre, Menshchikov and Li 2024, Zhang, Zhou, Esimbek, Baan, He, Tang, Li, Ji, Wu, Ma, Li, Zhou, Tursun and Komesh 2024) which can be responsible for the host cluster's increase in mass and size through accretion onto the cluster (Kirk et al. 2013, Karam and Sills 2023). As well, recent observation from Maity et al. (2024) suggests convergence of filamentary flows onto dense, massive star forming clumps implying that further evolution of hub filament systems may lead to the formation of star clusters. Understanding the flow of gas onto clusters is necessary to understand the dynamics of the cluster itself because of the star formation that will take place along the filamentary flows.

In Karam and Sills (2024) (hereafter Paper I), we showed that the surrounding gas environment plays a vital role in the build up of clusters through facilitating mergers at early times in the GMCs life. It is therefore important to consider realistic gas environments alongside stellar feedback and star formation to gain a full picture of the impacts of star cluster mergers on the dynamics of the clusters involved. In this work, we take a previous simulation performed in Paper I, and include prescriptions for star formation and stellar feedback to concretely discern their influence on the merger product. We analyze how both processes affect the phase space of the stars belonging to the cluster during and after the merger process. We also analyze the kinematics of

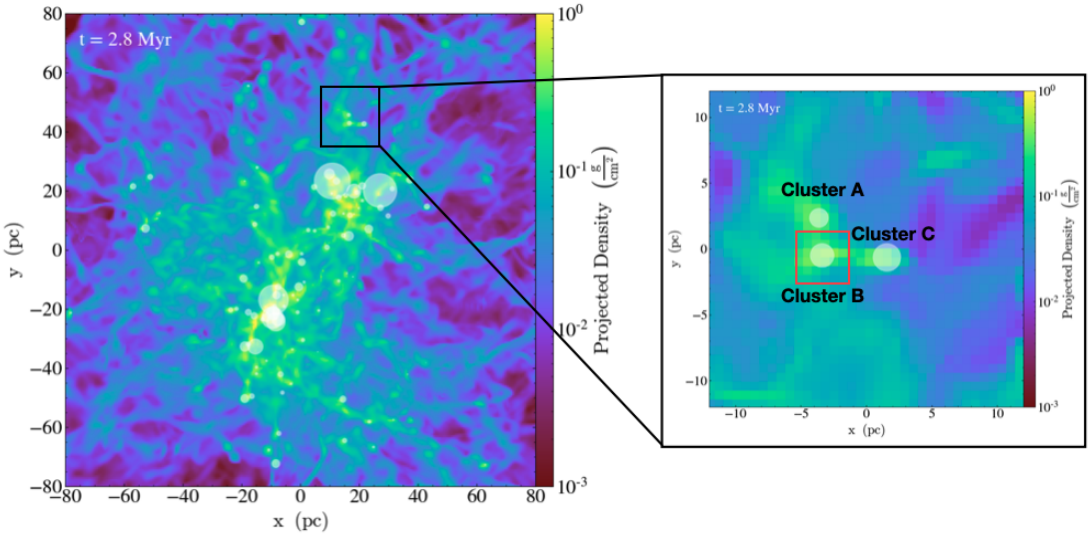

FIGURE 4.1: Left: Snapshot from simulation performed in Howard et al. (2018). White circles show locations of the sink particles with their size representing the mass of the sink. Black box shows the region taken for simulation `region1` in Paper I and `region1_SFFB` in this work. Colour shows gas surface density. Right: Zoom-in of region used as initial conditions for `region1` simulation (see Figure 4.2). Red box shows the sink particle whose stellar mass is plotted as the red line in Figure 4.4.

the cluster after it has removed most of its surrounding gas. This paper is structured as followed: in Section 4.2 we discuss the numerical methods and initial conditions used in our simulation, in Section 4.3 we discuss the evolution of the stars and gas in our star cluster merger simulation, in Section 4.4, we discuss the implications of our results, and in Section 4.5, we summarize our key results.

4.2 Methods

4.2.1 Numerical Methods

We perform our simulations using the ASURA+BRIDGE code (Fujii, Saitoh, Wang and Hirai 2021, Fujii, Saitoh, Hirai and Wang 2021). ASURA+BRIDGE evolves gas using the smoothed particle hydrodynamics (SPH) code `ASURA` (Saitoh et al. 2008, Saitoh et al. 2009), N-body dynamics using `PETAR` (Wang, Iwasawa, Nitadori and Makino 2020) and connects the two using the `BRIDGE` scheme (Fujii et al. 2007). The two codes are connected every bridge timestep which we choose to be $\Delta t_B = 200$yr. In `PETAR`, forces

from distant particles are calculated using a tree method (Barnes and Hut 1986) and nearby particle forces are calculated using a Hermite scheme. As well, `PETAR` includes a slow down algorithmic regularization scheme allowing the evolution of multiple systems and close encounters (Wang, Nitadori and Makino 2020).

ASURA+BRIDGE also includes a star formation prescription outlined in Hirai et al. (2021) and a feedback model outlined in Fujii, Saitoh, Hirai and Wang (2021). Stars form throughout our simulations with a given efficiency per free fall time. Once gas is above a certain density threshold, below a certain temperature threshold, and is converging, it is eligible to form a star. We choose the efficiency per free fall time to be 0.02, the density threshold to be $10^4 \mathrm{cm}^{-3}$, and the temperature threshold to be 30K. Once the above conditions are satisfied, a stellar mass is randomly chosen from a Kroupa (2001) mass function between $0.1\mathrm{M}_\odot$ and $150\mathrm{M}_\odot$. To form the star, we assemble mass from the surrounding region within a given radius. We choose this radius to be 0.2pc because Hirai et al. (2021) shows that this value results in star formation that fully samples the Kroupa (2001) mass function. The position and velocity of the newly formed star are inherited from the gas used to create the star.

Feedback is modelled through HII regions around massive stars. Once stars are massive enough, a Strömgren (Strömgren 1939) radius is estimated around the star using local density and ionizing photon rates from Lanz and Hubeny (2003). Gas inside the radius is injected with mechanical energy in the form of momentum to account for radiation (Kim et al. 2016) and stellar winds (Renaud et al. 2013). As well, thermal energy is injected into the surrounding gas to raise the temperature to 10^4K. Such feedback is implemented for stars more massive than $10\mathrm{M}_\odot$.

4.2.2 Initial Conditions

We take our initial conditions from previously run GMC simulations performed in Howard et al. (2018) (hereafter H18) using the `Flash` grid code (Fryxell et al. 2000) and convert the background gas into an SPH representation using the method outlined in Paper I. In summary, we take each grid cell present in the region of interest in the H18 simulation and place $\mathrm{N_{SPH}} = \mathrm{M_{cell}}/\mathrm{m_{SPH}}$ (where $\mathrm{M_{cell}}$ is the mass of the given grid cell, and $\mathrm{m_{SPH}}$ is the initial SPH particle mass) gas particles in a Gaussian distribution around the centre of each grid cell. The velocity of the gas in each grid cell is assigned to every SPH particle placed in that grid cell. We also give all gas in the simulation a velocity dispersion of $10\mathrm{kms}^{-1}$ which is consistent with simulations of star forming

regions (Pillsworth and Pudritz 2024). Lastly, we provide every SPH particle with the same internal energy as that of the grid cell it is placed around.

In the region chosen for this work, there are three sink particles, two of which eventually merge. Each sink contains a stellar and a gas component. We convert the sink particles to star clusters in a similar way as that presented in Karam and Sills (2022). We initialize the stellar component as a Plummer (Plummer 1911) sphere. We choose the size of the stellar distribution such that the density at the half mass radius is consistent with young massive cluster observations (Portegies Zwart et al. 2010). We choose the velocities of the stars such that the cluster is initially in virial equilibrium. We let the stellar distribution relax in a background gas distribution whose mass is given by the sink particle gas mass before placing the stars in the larger simulation alongside the background gas. We initialize the gas component of each sink as a uniform distribution in the larger simulation. We choose the size of the gas distribution such that the average density of the sink particle gas is $10^4 \mathrm{cm}^{-3}$ which is the threshold value for sink formation in H18. We give the gas a velocity dispersion of $10 \mathrm{kms}^{-1}$ to match the background gas. The region chosen is the same as `region1` from Karam and Sills (2024) allowing us to directly test the roles played by feedback and star formation (see Figure 4.1). This region contains three clusters (cluster A, B, and C). Clusters A and B participate in the merger, while cluster C does not. We call the simulation in this work `region1_SFFB`.

4.2.3 Identifying Star Clusters

Throughout the simulations, as clusters merge, and new stars form, the membership of our star clusters changes. We keep track of the components of each star cluster using a similar method as that outlined in Karam and Sills (2024).

We first use HDBSCAN (McInnes et al. 2017) to cluster the stars in 3D position space. To be considered part of a given cluster, we ensure that the spatially clustered stars are gravitationally bound. We then check whether the spatially unclustered stars are bound to each of the clusters present. If they are, we assign those spatially unclustered stars to the cluster with which it is most bound. If they are not bound to any cluster, we consider that star unbound. When checking for boundedness, we also consider all of the gas present in the simulation.

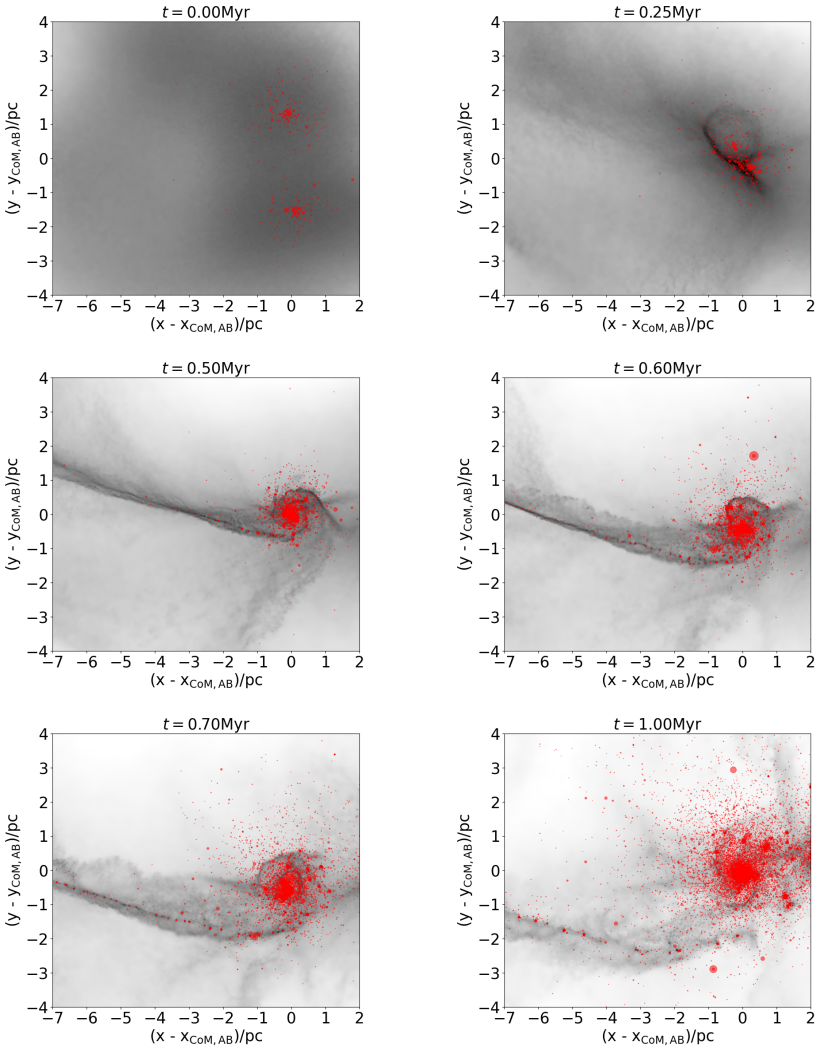

FIGURE 4.2: Snapshots of gas and bound stars around cluster AB from the `region1_SFFB` simulation. The x and y axes show the x and y positions subtracted by the centre of mass of cluster AB. Red circles represent the stars in each cluster and their size scales with the stars mass. Gas is shown in black with darker regions showing gas with higher densities. The range in gas densities shown is $0.1{-}10^3 \mathrm{M}_\odot \mathrm{pc}^{-3}$.

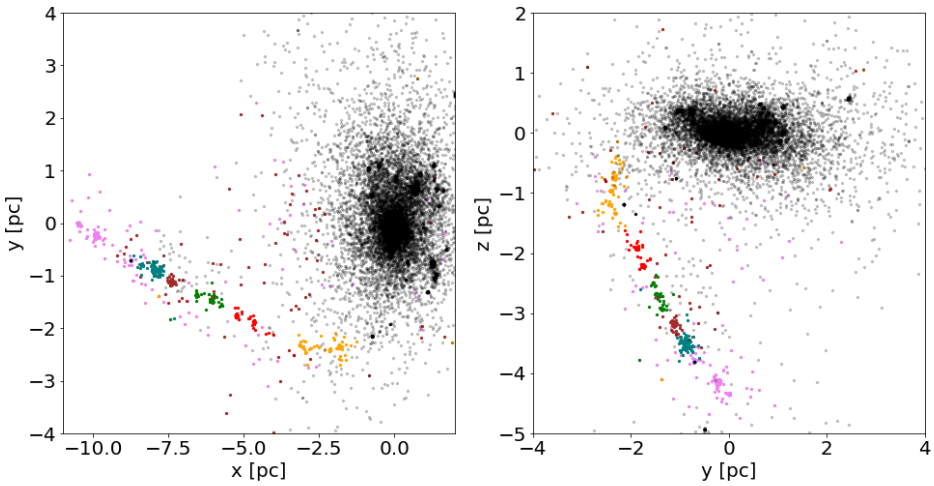

FIGURE 4.3: The locations of stars at t=1Myr after the beginning of the `region1_SFFB` simulation. The colours of the points indicate which subgroup each star belongs to as determined by `HDBSCAN`. The black points are made more translucent than the coloured points to make it easier to see the coloured clumps.

4.3 Results

We show the evolution of the `region1_SFFB` simulation in Figure 4.2. In this simulation, cluster A begins merging with cluster B at t≈ 0.06Myr which is roughly the same as the merger time in the `region1` simulation from Paper I. We call the merged cluster "cluster AB".

To discern the role played by the newly added physics (star formation, feedback, and cooling), we analyze cluster AB at t=1Myr and compare it to cluster AB at the same time from the `region1` simulation from Paper I. We show the distribution of bound stars at t=1Myr in the `region1_SFFB` simulation in Figure 4.3. Stars belonging to cluster AB are shown as black and grey points while coloured clumps can be seen along the negative x and z axes. These coloured clumps are the result of star formation taking place along a filament that is feeding gas to cluster AB throughout the simulation (this filament can be seen in the top-right panel of Figure 4.2, and we discuss it more in Section 4.3.2). The substructure we see in position space from Figure 4.3 is not present in velocity space. All of the stars belonging to cluster AB are mixed in velocity space as expected from a merger (Karam and Sills 2024). As well, the clumps which form along the filament are

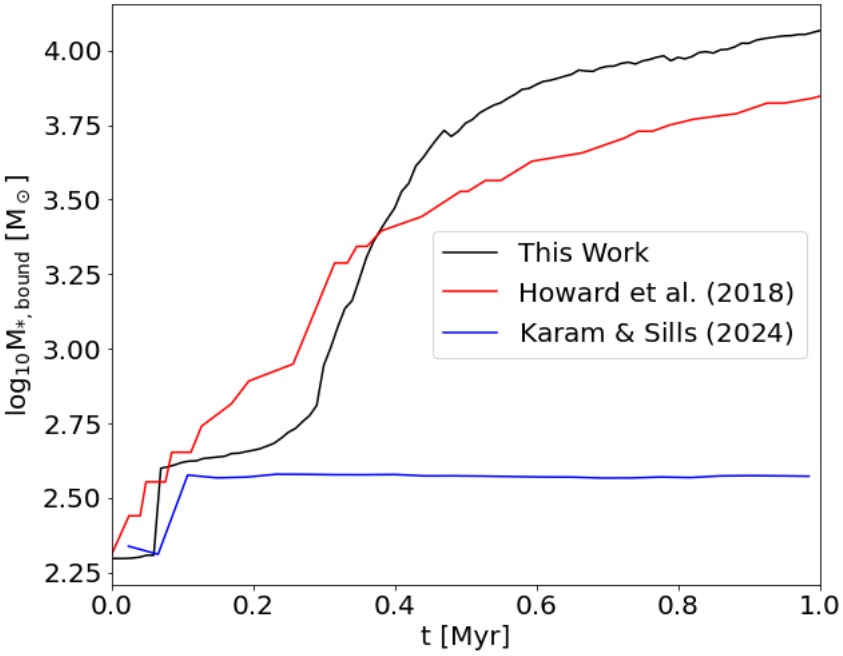

FIGURE 4.4: Bound stellar mass of cluster AB in `region1_SFFB` from this paper (black) and `region1` from Paper I (blue). Red line shows the mass of the most massive sink that participates in the merger from the region in the H18 simulation (see Figure 4.1).

mixed with each other and with cluster AB in velocity space at t=1Myr.

Figure 4.4 shows the mass of cluster AB as a function of time after the beginning of the simulation. We see here that the bound stellar mass of the cluster increases drastically as the merger takes place thanks to star formation. We compare this change in mass to that of the original sink particles from the H18 simulation as shown by the red line in Figure 4.4 which shows the bound stellar mass of the most massive sink that participates in the merger as a function of time (see Figure 4.1). The merger in the H18 simulation happens at a later time than in this work. In the H18 simulations, a sink particle converted gas into stars at a constant rate of 20% every free-fall time (0.36Myr). Our simulations show that the rate at which cluster AB gains bound stellar mass is not constant. This, along with our simulations ability to resolve gas at higher resolution than H18, results in our cluster having an overall higher mass than the corresponding H18 sink by t=1Myr. The mass of the H18 sink is $\approx$ 78% of the mass of cluster AB at t=1Myr. Lastly, the mass of cluster AB in the `region1` simulation stays constant after the merger takes place (blue line in Figure 4.4). This is because we did not include star formation in this simulation from Paper I.

There are two main processes contributing to this increase in mass in our simulation. The first is star formation taking place within cluster AB from the newly compressed gas. The second is the accretion of stellar clumps and star forming gas from the filament that traveled into cluster AB. Both of these processes together result in an increase in the bound stellar mass by $\approx$2.5 orders of magnitude in the `region1_SFFB` simulation when compared to the `region1` simulation in Paper I.

4.3.1 Ejected Stars From In-Situ Star Formation

With ASURA+BRIDGE, we resolve star formation and the formation of dynamical binaries but do not account for primordial binaries. The simulation begins with 31 binary systems in total. There are 9 and 7 binary systems in cluster A and B respectively at the beginning of the simulation. In the `region1_SFFB` simulation, dynamical binaries form as a result of the high density environment created by the merger of cluster A with cluster B.

Before the merger takes place, the binary fraction stays roughly constant. Consequently, only 1 star becomes unbound before the merger begins. Throughout the simulation after the merger, the number of binary systems increases. By t=1Myr, 5% of all stars belonging to cluster AB are in a binary system. Out of all the binary systems present in the simulation, 71% of them are in cluster AB at t=1Myr. The high

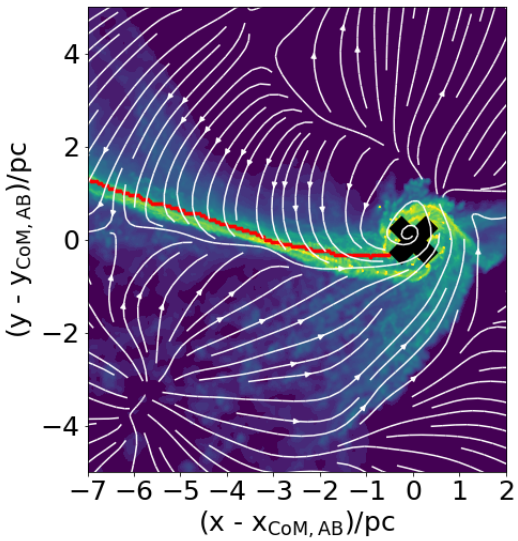

FIGURE 4.5: Dynamics of the gas around cluster AB in the `region1_SFFB` simulation at t=0.5Myr. Red line shows the identified filament using `fil_finder`, and the white stream lines show the density-weighted velocities of the gas. The gas density is shown as the colourmap with yellow regions showing denser gas. The range of gas densitiies is 10-$10^5 M_\odot pc^{-3}$. The black cross shows the location of the centre of mass of cluster AB.

concentration of binaries in cluster AB results in the dynamical ejection of stars and increases the unbound fraction of stars after the merger takes place. At t=1Myr, $\approx$ 25% of the stars that formed in cluster AB have become unbound. This is higher than the unbound fraction found as a result of mergers in both Karam and Sills (2022), and Cournoyer-Cloutier et al. (2024) implying that, while the merger process itself can increase the fraction of unbound stars around a cluster, new star formation in the dense environment created by the cluster merger results in a higher unbound fraction through dynamical ejections.

4.3.2 Filament Accretion

We use the `python` packages `fil_finder` (Koch and Rosolowsky 2015) and `radfil` (Zucker and Chen 2018) to identify filamentary shapes and calculate filament parameters in our simulations. To employ `fil_finder`, we convert our SPH particle data into a grid using `pynbody` (Pontzen et al. 2013) to average the gas density 5pc along the z-axis

around cluster AB to ensure we are not including gas that belongs to cluster C.

We find that a filament is well defined at t≈0.5Myr as seen in Figure 4.5. The width of the filament as given by the width of the Gaussian best fit is ≈ 0.4pc at this time in the simulation. We also show the dynamics of the gas as streamlines in the same figure and find that after the start of the merger, gas along the filament has net motions towards cluster AB. Furthermore, the merger has offset the densest component of the filament from the centre of mass of cluster AB and has wrapped around the cluster which imparts a large amount of angular momentum onto the stars in cluster AB (we discuss this more in Section 4.3.3). As most of the stellar mass belonging to cluster AB by t=1Myr comes from newly formed stars, and these newly formed stars inherit the motions of the gas they form from, the dynamics of the gas has a direct impact on the dynamics of stellar component of the cluster.

At t=1Myr, the centres of mass of the stellar clumps along the filament (see Figure 4.3) are separated by 2.0pc on average. We can compare the separation of these cores to that expected of an isothermal cylindrical gas distribution from the derivation presented in Nagasawa (1987), namely:

$$\lambda = 7.8 c_s \sqrt{\frac{2}{\pi G \rho_0}} \tag{4.1}$$

where λ is the separation between dense cores in a filament, c_s is the sound speed of the gas, G is the gravitational constant, and ρ_0 is the central gas density of the filament. Using the density and temperature thresholds for star formation to provide an upper limit (see Section 4.2.1) we calculate λ=5.1pc, a factor of ≈2.5 larger than the separation of the HDBSCAN clumps at t=1Myr. This calculation, however, does not take into account the changing density of the filament, or the external pressure from the surrounding environment. We discuss this more in Section 4.4.

4.3.3 Stellar Dynamics

We see from Figure 4.3 that the structure of cluster AB in physical space is flattened along the z-axis. This pattern is also seen in the velocity structure of the cluster as can be seen in Figure 4.6 where we find that the velocity dispersion along the z-axis is lower than that along the x and y axes. The trend present in the evolution of the velocity dispersion of cluster AB is an increase after the start of the merger, and a slow decrease throughout the remainder of the simulation. In Paper I, we used this to determine a violent relaxation timescale for the merger of cluster A and B of 0.4Myr. Because the

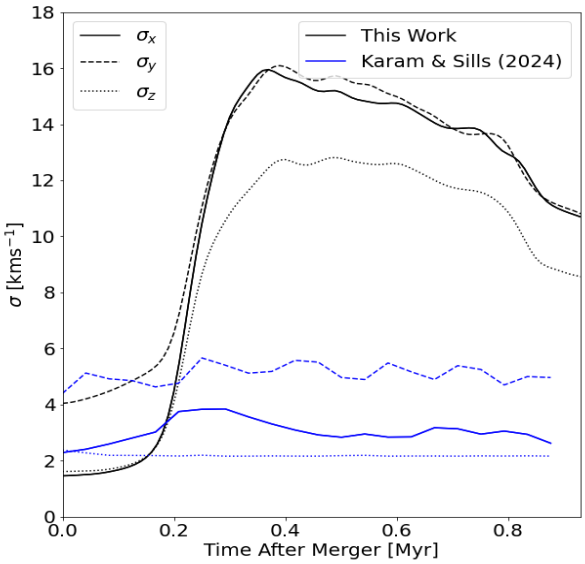

FIGURE 4.6: Velocity dispersion along each axis for cluster AB from the `region1` simulation in this paper (black) and in Paper I (blue).

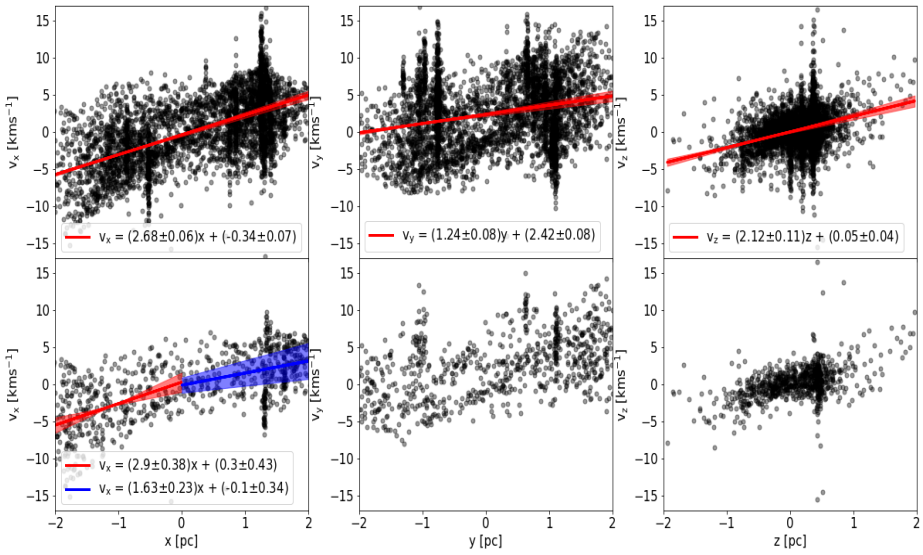

FIGURE 4.7: The position against velocity for stars belonging to cluster AB at distances between the 75% mass radius and the nearest clump identified by HDBSCAN (top), and between the 90% mass radius and the nearest clump identified by HDBSCAN (bottom). Left, middle, and right panels show this along the x, y, and z axes respectively. Red lines in the top panel show the lines of best fit data with the errors obtained through bootstrapping 10^5 times. Red and blue lines in the bottom panel show the lines of best fit for the data with $x < 0$ and $x > 0$ respectively. Shaded regions for all lines show the 3σ uncertainty of the best fit line. Positions and velocities are around the centre of mass position and velocity respectively of cluster AB.

velocity dispersion has not plateaued by the 1Myr mark shown in Figure 4.6, we conclude that star formation has extended the dynamical timescale of the merger process. As well, star formation has caused the velocity dispersion to increase compared to the `region1` simulation from Paper I. We find that the velocity dispersion of the gas that participates in the merger follows a similar trend to the stars in the `region1_SFFB` simulation. This implies that the increase in velocity dispersion comes from the formation of stars with velocity inherited from the dense gas.

After the merger, the 75% and 90% mass radii increase while the 50% mass radius remains constant implying that there is expansion present in the outer regions of the cluster (similar to Paper I). To analyze this expansion in detail, we show position-velocity diagrams of the cluster AB stars in the `region1_SFFB` simulation at radii between the 75% mass radius and the distance to the nearest clump identified by HDBSCAN in the top row of Figure 4.7. We see that there are signals of expansion along each axis by fitting a line to the data and using the slope to tell us the rate of expansion. We find that the expansion rates shown in Figure 4.7 are higher than those calculated for the `region1` simulation in Paper I. As well, anisotropic expansion is present in Figure 4.7 with the strongest expansion signature along the x-axis and the weakest along the y-axis. Furthermore, there is anisotropic expansion in the outer regions of the cluster present along the x-axis. We see this when considering stars beyond the 90% mass radius and within the distance to the nearest HDBSCAN clump as shown in the bottom row of Figure 4.7. By fitting lines to the stars along the negative and positive x-axes separately, we see that the expansion rate along the negative x-axis is 1.80±0.34 times that along the positive x-axis. The anisotropic expansion comes from a combination of the rotation induced onto cluster AB from the surrounding gas, and the centre of mass motion of the cluster which is along the positive x-axis.

The vertical streaks present along each axis in the data shown in Figure 4.7 show the substructure of cluster AB. As the cluster is growing in mass after the merger, it accretes new clumps of stars that have formed along a filament (see Section 4.3.2) and these clumps do not coalesce with the rest of the stars that make up cluster AB at this point in the simulation and instead show up as vertical streaks in the position-velocity diagrams. We check whether the accreted clumps contribute to the overall substructure in cluster AB by calculating the Q parameter (Cartwright and Whitworth 2004):

$$Q = \frac{\bar{m}}{\bar{s}} \tag{4.2}$$

where $\bar{m}$ is the mean edge length of the branches of a minimum spanning tree created

for the star cluster, and $\bar{s}$ is the mean separation between stars divided by the cluster radius. A value of Q < 0.8 implies substructure, while a value of Q > 0.8 implies a smooth distribution with a radial density gradient. At t=1Myr, the Q parameter is 1.36 implying that cluster AB is heavily centrally concentrated and lacks detectable substructure. This is expected as the accreted clumps are low in size and mass compared to that of cluster AB.

We now analyze the change in angular momentum of cluster AB as the `region1_SFFB` simulation evolves. We find that after the merger takes place, the total z-component specific angular momentum increases and continues doing so by t=1Myr after the start of the simulation. This is contrary to the results we found for the `region1` simulation in Paper I where the z-component specific angular momentum slowly decreased after reaching a peak at the beginning of the merger. To investigate the cause of this difference, we show the distribution of the z-component of the specific angular momentum for all cluster AB stars at t=1Myr in Figure 4.8. The blue histogram shows those stars which formed in-situ, and the orange histogram shows those stars which were accreted. We define an accreted star as a star which formed outside the 90% mass radius of cluster AB, but was then bound to cluster AB at t=1Myr.

From Figure 4.8 we see that the distribution of the z-component specific angular momentum of the accreted stars is shifted compared to the same distribution for the in-situ stars by t=1Myr. The accreted stars account for 23% of the total z-component specific angular momentum of cluster AB, but only account for 7% of the total number of stars belonging to the cluster. This is a similar result to the `region2` simulation from Paper I and further illustrates the importance of the cluster environment in shaping the angular momentum of a merging star cluster. This result also shows that, while mergers can result in an increase in angular momentum, they are not the drivers of that increase in our simulations. Accretion of new stars from a filament or nearby cluster is necessary for the continuous supply of angular momentum in a cluster.

4.3.4 Evolution Up To Gas Removal

By t=2Myr in the `region1_SFFB` simulation, the bound stellar mass of cluster AB stops growing at $1.3\times10^4 M_\odot$. At this point, the mass of gas within cluster AB has decreased to 13% of its original value. Because of this, we stop the simulation at t=2Myr. We also see that the star formation rate in the entire simulation has decreased drastically from its peak during the merger in Figure 4.9. The crossing time of cluster AB at t=2Myr is 0.3Myr meaning that $\approx$3 crossing times have passed since t=1Myr. The half-mass

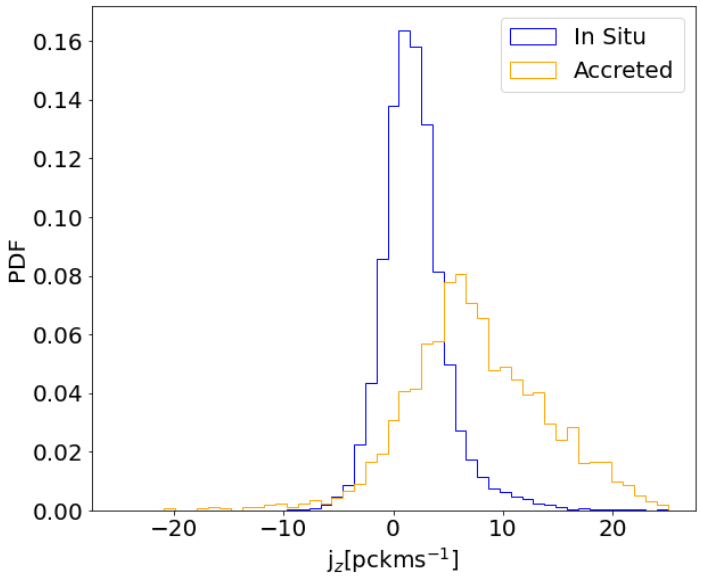

FIGURE 4.8: Distribution of z-component of specific angular momentum (j_z) for all stars belonging to cluster AB at t=1Myr in the `region_1SFFB` simulation. Blue line shows stars which were formed in-situ of cluster AB, and orange line shows stars which were accreted onto cluster AB.

relaxation time of cluster AB at 2Myr is 10.6Myr. The virial parameter ($\alpha = 2K/|U|$ where K is the kinetic energy of the stellar component of the cluster and U is the potential energy of the stellar and gas component of the cluster) of cluster AB at this time is 1.4 implying that the cluster is supervirial. Though the cluster has survived only a very small fraction of its half-mass relaxation time, studying its dynamics at this phase of its evolution gives us crucial insight into the initial conditions for massive star cluster evolution after the clusters have emerged from their embedded phase.

We now discuss the survivability of the dynamical signatures we found to be inherited from the merger of cluster A with cluster B in the `region1_SFFB` simulation (see Section 4.3.3) at the time of gas removal in the cluster. At t=2Myr, cluster AB is still flattened along the z-axis in all of phase space. The velocity dispersions along the x and y axes remain ≈1.3 times higher than the velocity dispersion along the z-axis throughout the entire simulation after the onset of star formation triggered by the merger of cluster A and cluster B. We do not see any substructure in velocity space in cluster AB at t=2Myr.

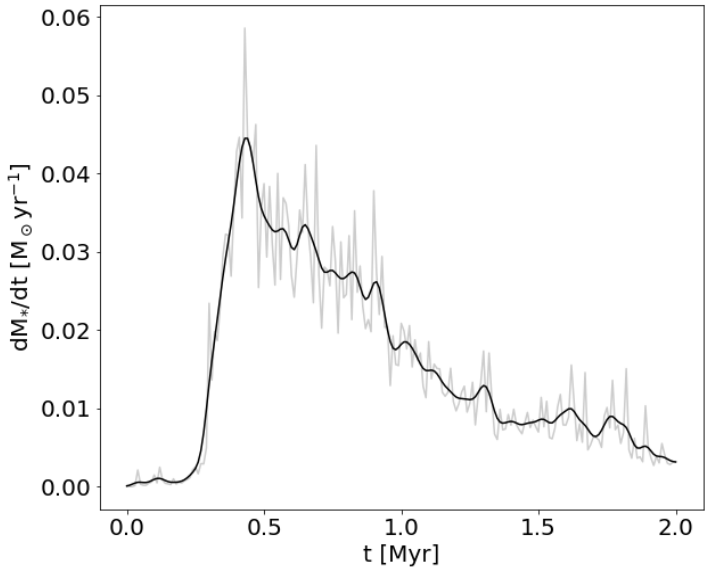

FIGURE 4.9: Star formation rate as a function of time throughout the `region1_SFFB` simulation. Grey line shows original data and black line shows a Gaussian smoothing of the data over 0.02Myr.

By t=2Myr, the expansion rates in the outer regions of cluster AB along each axis have decreased from their maxima during the height of star formation and are $0.48\pm0.02\text{Myr}^{-1}$, $0.36\pm0.02\text{Myr}^{-1}$, $0.40\pm0.03\text{Myr}^{-1}$ along x, y, and z respectively. The magnitude of the anisotropic expansion of cluster AB between x, y, and z present has decreased from its peak which occurred during the merger. We also calculate the strength of the anisotropic expansion along the x-axis and compare it to that present at t=1Myr (bottom left panel of Figure 4.7). The expansion rate along the negative x-axis is $0.92\pm0.21\text{Myr}^{-1}$ that along the positive x-axis which is lower than the same fraction calculated at t=1Myr. Therefore, as cluster AB has stopped growing through star formation and accretion, its rate of expansion has decreased and so too has the magnitude of the anisotropic expansion. However, both are still present in the cluster.

The z-component angular momentum of cluster AB decreases slightly from its peak value by 2Myr as seen in Figure 4.10. This begins when clumps which were accreted onto cluster AB from the star forming filament split off of cluster AB instead of becoming fully accreted onto the cluster. The accreted stars still contribute a disproportionate amount to the z-component specific angular momentum though to a lesser extent than earlier on in the simulation. The accreted stars account for 6.5% of the total number of stars belonging to cluster AB but account for 15% of the total z-component specific angular momentum at t=2Myr. This is because the accreted stars remain in the outskirts of cluster AB after becoming accreted converse to the in-situ stars which remain closer to the cluster centre.

We also construct the rotational velocity profile of cluster AB by calculating the rotational velocity in spherical coordinates in evenly spaced bins from the centre of the cluster (Figure 4.11). The lack of rotation in the ϕ direction comes from the fact that the merger takes place mostly in the x-y plane resulting in counter clockwise rotation. The v_θ profile shows differential rotation is present inside the cluster with a profile that has also been seen in clusters that have experienced violent relaxation from core collapse: low rotation in the inner regions, a peak in rotational velocity in the intermediate regions, and lower to no rotational velocity in the outermost regions (e.g. Tiongco et al. 2022). We discuss this more in Section 4.4.

Lastly, to understand the future dynamical evolution of cluster AB, we calculate the velocity anisotropy defined as in Binney and Tremaine (2008):

$$\beta = 1 - \frac{\sigma_\phi^2 + \sigma_\theta^2}{2\sigma_r^2} \tag{4.3}$$

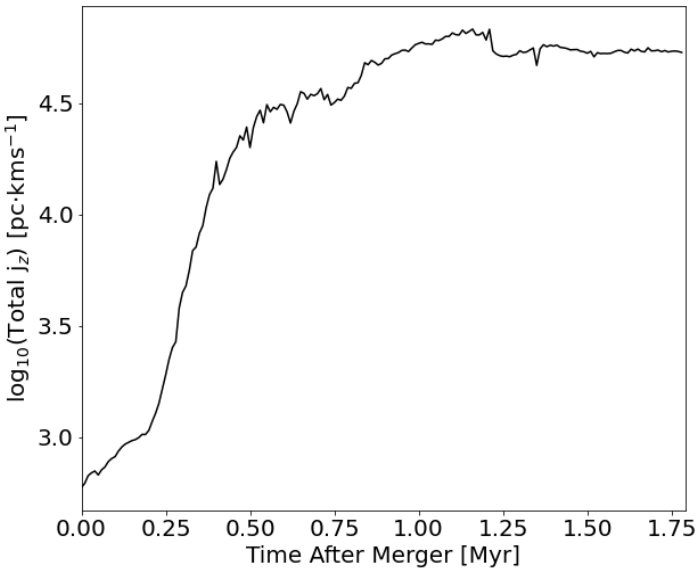

FIGURE 4.10: Total z-component specific angular momentum of stellar component of cluster AB in the `region1_SFFB` simulation.

where σ_ϕ and σ_θ are the dispersions of the tangential component of the velocity, and σ_r is the dispersion of the radial component of the velocity in spherical coordinates. The presence of velocity anisotropy has implications for the long term evolution of a cluster (e.g. Tiongco et al. 2016, Pavlík and Vesperini 2021, Pavlík et al. 2024) by controlling timescales upon which relaxation processes including core collapse take place. In the `region1_SFFB` simulation we find that cluster AB begins developing very slight velocity anisotropy post merger and by 2Myr, has β =0.17 implying that it will begin its post embedded phase evolution with only mild radial anisotropy. We show the distribution of the velocity anisotropy as a function of radial distance away from the cluster centre in Figure 4.11. Qualitatively, this profile is similar to that presented in Vesperini et al. (2014): an isotropic core, and a radially anisotropic intermediate region (note that by 2Myr, 10 half mass radii is equal to the 90% mass radius). This trend is similar to that of the virial parameter which is much higher in the outer regions of the cluster than in the inner regions. The velocity anisotropy profile presented here does not return to isotropy in the outer regions like that from Vesperini et al. (2014) likely because our simulation does not include the long term evolution of the cluster inside an external tidal field (Baumgardt and Makino 2003). In Vesperini et al. (2014), this profile emerged as a response to the violent relaxation process felt by a cluster as it reaches core collapse

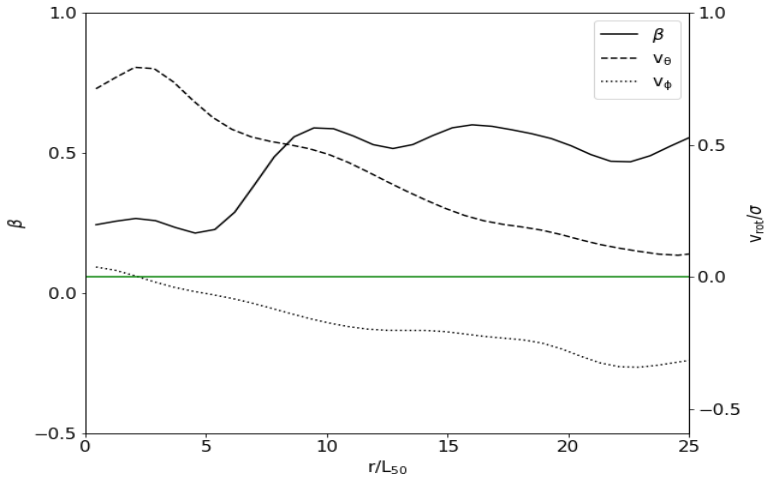

FIGURE 4.11: Velocity anisotropy (solid, left y-axis) and rotational velocity profiles of cluster AB in the `region1_SFFB` simulation in spherical coordinates (dashed, and dotted, right y-axis) at t=2Myr. The rotational velocity is normalized by $\sigma = \sqrt{\sigma_r^2 + \sigma_\theta^2 + \sigma_\phi^2}/3$. All black lines show a Gaussian smoothing of the respective data over 0.5pc. The horizontal green line shows a value of zero.

alongside an external tidal field. As a star cluster merger can be described using violent relaxation (see Paper I), it is expected that we see a similar velocity anisotropy profile. Our results here show that evolution within the natal gas cloud is not enough to erase the signatures of violent relaxation in the outer regions of the cluster that were inherited from the cluster merger before the star cluster removes its surrounding gas.

4.4 Discussion

Fukushima and Yajima (2021) show that stellar feedback is inefficient at suppressing star formation when cloud surface densities reach $\Sigma \approx 100 M_\odot pc^{-2}$. Such a suppression can lead to high star formation efficiencies $\epsilon_* = M_*/M_{gas,0}$ where M_* is the stellar mass formed, and $M_{gas,0}$ is the mass of gas at the beginning of the simulation. We calculate ϵ_* at the end of our simulation and find $\epsilon_* = 51\%$. Such a high star formation efficiency is expected in our simulation as the gas distribution we use as our initial condition contains gas with $\Sigma \gtrapprox 1000 M_\odot pc^{-2}$ within each sub-cluster. Furthermore, as the merger of cluster A with cluster B increases gas density within the cluster, feedback is expected to be even less effective at stopping star formation.

The runaway stars produced in the `region1_SFFB` simulation are almost all stars that were formed as a result of the compression of gas from the cluster merger. We do not find a preferred direction for the runaway stars converse to results found in simulations by Polak et al. (2024) and in observations by Stoop et al. (2024). This is likely due to the fact that cluster A and cluster B in our simulation have similar masses, and in turn, similar potentials which is converse to the potential distribution from Polak et al. (2024). As a consequence, we do not see the slingshot effect that was seen in Polak et al. (2024) to produce runaways with a preferred direction. Allowing for the formation of primordial binaries will also likely affect runaway star production (Cournoyer-Cloutier et al. 2024).

In Paper I, we predicted that a cluster may be able to develop kinematic subgroups associated with age gradients as they grow through mergers. We do not see these subgroups in the `region1_SFFB` simulation presented in this work. The clumps that form along the nearby filament and become accreted onto cluster AB are too small compared to the amount of star formation that takes place within cluster AB during the merger and do not show up as distinct shapes in velocity space. However, if we only consider the HDBSCAN clumps that are not clusters AB or C (i.e. those that form along the filament), we do find the presence of subgroups in velocity space meaning that kinematic subgroups in clusters may preferentially arise in dry star cluster mergers.

The filament seen in Figure 4.5 is influenced by the surrounding gas within the cloud. As seen by the velocity streamlines in this figure, gas is flowing onto the filament from above and below its principal axis. This process acts as external pressure onto the filament which has a bearing on its core separation leading to smaller core separations than those expected from Equation 4.1 (Nagasawa 1987). Anathpindika and Di Francesco (2024) showed that high pressure environments can push core separations down to the order of 0.1pc. As well, the average gas density along the filament in our simulation presented here is greater than the star formation threshold density during star formation across the filament leading to a further decrease in the expected core separation. We therefore propose the following method of clump growth in filaments: the filament begins by forming stars at low separations, and these stars collect together to form the HDBSCAN identified clumps. In our scenario, gas cores form quickly after the formation of the filament, collapse to form stars, and the stars collect to form clumps.

The addition of star formation and cooling into our simulation has reinforced a key conclusion from Paper I: the distribution of gas is extremely important in influencing the dynamics of clusters as they merge embedded inside a GMC. Our results from this

work suggest that dynamical signatures that are inherited from the hierarchical cluster formation process are able to persist throughout the embedded phase of a clusters life and beyond.

We can use the rotation and velocity anisotropy present in cluster AB at t=2Myr in the `region1_SFFB` simulation to predict its long-term evolution. We estimate the concentration c = $\log_{10}(L_{90}/L_{10})$ where L_{90} is the 90% mass radius, and L_{10} is the 10% mass radius, of the cluster at t=2Myr and find that c≈2. This along with the mass and size of cluster AB at t=2Myr suggests that it will likely be destroyed by evaporation in $\approx 40 t_{rh}$ where t_{rh} is the half-mass relaxation time of cluster AB (Gnedin and Ostriker 1997). Beginning with rotation, Livernois et al. 2022 find that clusters with initial rotation can develop mass dependent rotation in as little as $1 t_{rh}$ well before the expected evaporation of cluster AB. As the cluster evolves further, the distribution of angular momentum is expected to move outwards and the cluster will lose mass and memory of its initial rotation before its expected evaporation time (Tiongco et al. 2017). Lastly, the velocity anisotropy profile of cluster AB at t=2Myr suggests a quicker evolution towards core-collapse and energy equipartition than a cluster with an isotropic profile with both processes occurring well before the expected evaporation time (Pavlík and Vesperini 2021).

The decrease in overall expansion present in cluster AB is consistent with observations presented in Della Croce et al. (2024) where the authors observe a trend of decreasing expansion magnitude with increasing age. We cannot compare the expansion rates present in this work to those found in Wright et al. (2024) because those clusters have much lower stellar mass than cluster AB in this work. Future work involving the simulation of star cluster formation from a wider array of initial gas morphologies will allow us to perform a comparison.

4.5 Summary

We have run a zoom-in simulation of star cluster assembly with the inclusion of star formation and a stellar feedback prescription to analyze the role played by star cluster mergers in shaping the dynamics of star clusters as they evolve embedded inside their natal gas cloud. We have compared this simulation to the same one without star formation or stellar feedback (`region1` from Paper I). Star cluster growth in the simulation with star formation and feedback happens via star formation within the merged cluster as a result of gas compression, and through accretion of nearby star forming gas from

a filament. Clumps of stars have also formed along the filament and become accreted onto the merged cluster. In the simulation presented in this work with star formation and feedback, the magnitudes of the rotation and anisotropic expansion of the stellar component of the resultant cluster are stronger than in the same simulation from Paper I without star formation or feedback. Rotation is enhanced by gas accretion from a nearby filament, and this contributes to the anisotropic expansion towards the merger axis. We also analyze the dynamics of the resultant cluster after it has removed most of its surrounding gas through star formation and feedback. By the end of the simulation, the difference between the expansion rates along each axis has decreased implying the magnitude of the anisotropic expansion has decreased. Conversely, the angular momentum increases until t≈1Myr and stays roughly constant until the end of the simulation with only slight decreases whenever clumps become removed from the merged cluster. The rotational velocity profile of the resultant cluster is peaked in the intermediate region of the cluster. We also analyze the velocity anisotropy profile of the cluster and find that the merged cluster has an isotropic core with a radially anisotropic outer region.

Because of the strong influence of gas morphology on cluster dynamics, we suggest that future simulations should employ an accurate modelling of the interstellar medium within which star formation and star cluster build up can occur if they are to accurately reproduce the emerging star cluster.

Bibliography

Anathpindika, S. V. and Di Francesco, J. (2024). On the formation of cores in accreting filaments and the impact of ambient environment on it, PASA **41**: e091.

Armstrong, J. J. and Tan, J. C. (2024). Expansion kinematics of young clusters: I. Lambda Ori, A&A **692**: A166.

Barnes, J. and Hut, P. (1986). A hierarchical O(N log N) force-calculation algorithm, *Nature Astronomy* **324**(6096): 446–449.

Baumgardt, H. and Makino, J. (2003). Dynamical evolution of star clusters in tidal fields, MNRAS **340**(1): 227–246.

Binney, J. and Tremaine, S. (2008). *Galactic Dynamics: Second Edition.*

Briceño-Morales, G. and Chanamé, J. (2023). Substructure, supernovae, and a time-resolved star formation history for Upper Scorpius, MNRAS **522**(1): 1288–1309.

Cantat-Gaudin, T., Jordi, C., Wright, N. J., Armstrong, J. J., Vallenari, A., Balaguer-Núñez, L., Ramos, P., Bossini, D., Padoan, P., Pelkonen, V. M., Mapelli, M. and Jeffries, R. D. (2019). Expanding associations in the Vela-Puppis region. 3D structure and kinematics of the young population, A&A **626**: A17.

Cartwright, A. and Whitworth, A. P. (2004). The statistical analysis of star clusters, MNRAS **348**(2): 589–598.

Chen, Y., Li, H. and Vogelsberger, M. (2021). Effects of initial density profiles on massive star cluster formation in giant molecular clouds, MNRAS **502**(4): 6157–6169.

Cournoyer-Cloutier, C., Karam, J., Sills, A., Zwart, S. P. and Wilhelm, M. J. C. (2024). Binary Disruption and Ejected Stars from Hierarchical Star Cluster Assembly, ApJ **975**(2): 207.

Della Croce, A., Dalessandro, E., Livernois, A. and Vesperini, E. (2024). Young, wild, and free: The early expansion of star clusters, A&A **683**: A10.

Deshmukh, S., Linden, S. T., Calzetti, D., Adamo, A., Messa, M., Grasha, K., Sabbi, E., Smith, L. and Johnson, K. E. (2024). The Clearing Timescale for Infrared-selected Star Clusters in M83 with HST, ApJ **974**(2): L24.

Dewangan, L. K., Bhadari, N. K., Maity, A. K., Eswaraiah, C., Sharma, S. and Jadhav, O. R. (2024). Galactic 'Snake' IRDC G11.11-0.12: a site of multiple hub-filament systems and colliding filamentary clouds, MNRAS **527**(3): 5895–5915.

Dobbs, C. L., Bending, T. J. R., Pettitt, A. R. and Bate, M. R. (2022). The formation of massive stellar clusters in converging galactic flows with photoionization, MNRAS **509**(1): 954–973.

Dobbs, C. L., Bending, T. J. R., Pettitt, A. R., Buckner, A. S. M. and Bate, M. R. (2022). The formation of clusters and OB associations in different density spiral arm environments, MNRAS **517**(1): 675–696.

Fahrion, K. and De Marchi, G. (2023). The hierarchical formation of 30 Doradus as seen by JWST, *arXiv e-prints* p. arXiv:2311.06336.

Fryxell, B., Olson, K., Ricker, P., Timmes, F. X., Zingale, M., Lamb, D. Q., MacNeice, P., Rosner, R., Truran, J. W. and Tufo, H. (2000). FLASH: An Adaptive Mesh Hydrodynamics Code for Modeling Astrophysical Thermonuclear Flashes, ApJS **131**(1): 273–334.

Fujii, M., Iwasawa, M., Funato, Y. and Makino, J. (2007). BRIDGE: A Direct-Tree Hybrid N-Body Algorithm for Fully Self-Consistent Simulations of Star Clusters and Their Parent Galaxies, *PASJ* **59**: 1095.

Fujii, M. S., Saitoh, T. R., Hirai, Y. and Wang, L. (2021). SIRIUS project. III. Star-by-star simulations of star cluster formation using a direct N-body integrator with stellar feedback, PASJ **73**(4): 1074–1099.

Fujii, M. S., Saitoh, T. R., Wang, L. and Hirai, Y. (2021). SIRIUS project. II. A new tree-direct hybrid code for smoothed particle hydrodynamics/N-body simulations of star clusters, PASJ **73**(4): 1057–1073.

Fujii, M. S., Wang, L., Hirai, Y., Shimajiri, Y., Kumamoto, J. and Saitoh, T. (2022). SIRIUS Project - IV. The formation history of the Orion Nebula Cluster driven by clump mergers, MNRAS **514**(2): 2513–2526.

Fukushima, H. and Yajima, H. (2021). Radiation hydrodynamics simulations of massive star cluster formation in giant molecular clouds, *Monthly Notices of the Royal Astronomical Society* **506**(4): 5512–5539.
URL: *http://dx.doi.org/10.1093/mnras/stab2099*

Gnedin, O. Y. and Ostriker, J. P. (1997). Destruction of the Galactic Globular Cluster System, ApJ **474**(1): 223–255.

Hacar, A., Clark, S. E., Heitsch, F., Kainulainen, J., Panopoulou, G. V., Seifried, D. and Smith, R. (2023). Initial Conditions for Star Formation: a Physical Description of the Filamentary ISM, *in* S. Inutsuka, Y. Aikawa, T. Muto, K. Tomida and M. Tamura (eds), *Protostars and Planets VII*, Vol. 534 of *Astronomical Society of the Pacific Conference Series*, p. 153.

Hirai, Y., Fujii, M. S. and Saitoh, T. R. (2021). SIRIUS project. I. Star formation models for star-by-star simulations of star clusters and galaxy formation, PASJ **73**(4): 1036–1056.

Howard, C. S., Pudritz, R. E. and Harris, W. E. (2018). A universal route for the formation of massive star clusters in giant molecular clouds, *Nature Astronomy* **2**: 725–730.

Karam, J. and Sills, A. (2022). Modelling star cluster formation: mergers, MNRAS **513**(4): 6095–6104.

Karam, J. and Sills, A. (2023). Modelling star cluster formation: Gas accretion, MNRAS **521**(4): 5557–5569.

Karam, J. and Sills, A. (2024). Dynamics of Star Cluster Formation: Mergers in Gas-rich Environments, ApJ **967**(2): 86.

Kim, J.-G., Kim, W.-T. and Ostriker, E. C. (2016). Disruption of Molecular Clouds by Expansion of Dusty H II Regions, ApJ **819**(2): 137.

Kirk, H., Myers, P. C., Bourke, T. L., Gutermuth, R. A., Hedden, A. and Wilson, G. W. (2013). Filamentary Accretion Flows in the Embedded Serpens South Protocluster, ApJ **766**(2): 115.

Koch, E. W. and Rosolowsky, E. W. (2015). Filament identification through mathematical morphology, MNRAS **452**: 3435–3450.

Kroupa, P. (2001). On the variation of the initial mass function, MNRAS **322**(2): 231–246.

Kumar, M. S. N., Arzoumanian, D., Men'shchikov, A., Palmeirim, P., Matsumura, M. and Inutsuka, S. (2022). Filament coalescence and hub structure in Mon R2. Implications for massive star and cluster formation, A&A **658**: A114.

Lahén, N., Naab, T. and Szécsi, D. (2024). Star clusters forming in a low-metallicity starburst - rapid self-enrichment by (very) massive stars, MNRAS **530**(1): 645–667.

Lanz, T. and Hubeny, I. (2003). A Grid of Non-LTE Line-blanketed Model Atmospheres of O-Type Stars, ApJS **146**(2): 417–441.

Lewis, S. C., McMillan, S. L. W., Mac Low, M.-M., Cournoyer-Cloutier, C., Polak, B., Wilhelm, M. J. C., Tran, A., Sills, A., Portegies Zwart, S., Klessen, R. S. and Wall, J. E. (2023). Early-forming Massive Stars Suppress Star Formation and Hierarchical Cluster Assembly, ApJ **944**(2): 211.

Livernois, A. R., Vesperini, E., Varri, A. L., Hong, J. and Tiongco, M. (2022). Long-term evolution of multimass rotating star clusters, MNRAS **512**(2): 2584–2593.

Maity, A. K., Dewangan, L. K., Bhadari, N. K., Fukui, Y., Haj Ismail, A., Jadhav, O. R., Sharma, S. and Sano, H. (2024). G321.93-0.01: A Rare Site of Multiple Hub-Filament Systems with Evidence of Collision and Merging of Filaments, *arXiv e-prints* p. arXiv:2411.13870.

McInnes, L., Healy, J. and Astels, S. (2017). hdbscan: Hierarchical density based clustering, *The Journal of Open Source Software* **2**(11): 205.

Nagasawa, M. (1987). Gravitational Instability of the Isothermal Gas Cylinder with an Axial magnetic Field, *Progress of Theoretical Physics* **77**(3): 635–652.

Ordenes-Huanca, C., Zoccali, M., Bayo, A., Cuadra, J., Contreras Ramos, R. and Rojas-Arriagada, A. (2024). Unveiling the structural content of NGC 6357 via kinematics and NIR variability, MNRAS **533**(1): 841–859.

Pavlík, V., Heggie, D. C., Varri, A. L. and Vesperini, E. (2024). Dynamics of star clusters with tangentially anisotropic velocity distribution, A&A **689**: A313.

Pavlík, V. and Vesperini, E. (2021). New insights into star cluster evolution towards energy equipartition, MNRAS **504**(1): L12–L16.

Pillsworth, R. and Pudritz, R. E. (2024). Necessary conditions for the formation of filaments and star clusters in the cold neutral medium, MNRAS **528**(1): 209–233.

Plummer, H. C. (1911). On the problem of distribution in globular star clusters, MNRAS **71**: 460–470.

Polak, B., Mac Low, M.-M., Klessen, R. S., Portegies Zwart, S., Andersson, E. P., Appel, S. M., Cournoyer-Cloutier, C., Glover, S. C. O. and McMillan, S. L. W. (2024). Massive Star Cluster Formation II. Runaway Stars as Fossils of Sub-Cluster Mergers, *arXiv e-prints* p. arXiv:2405.12286.

Pontzen, A., Roškar, R., Stinson, G. S., Woods, R., Reed, D. M., Coles, J. and Quinn, T. R. (2013). pynbody: Astrophysics Simulation Analysis for Python. Astrophysics Source Code Library, ascl:1305.002.

Portegies Zwart, S. F., McMillan, S. L. W. and Gieles, M. (2010). Young Massive Star Clusters, *Annual Reviews of* A&A **48**: 431–493.

Rawat, V., Samal, M. R., Walker, D. L., Ojha, D. K., Tej, A., Zavagno, A., Zhang, C. P., Elia, D., Dutta, S., Jose, J., Eswaraiah, C. and Sharma, E. (2024). The Giant Molecular Cloud G148.24+00.41: gas properties, kinematics, and cluster formation at the nexus of filamentary flows, MNRAS **528**(2): 2199–2219.

Renaud, F., Bournaud, F., Emsellem, E., Elmegreen, B., Teyssier, R., Alves, J., Chapon, D., Combes, F., Dekel, A., Gabor, J., Hennebelle, P. and Kraljic, K. (2013). A sub-parsec resolution simulation of the Milky Way: global structure of the interstellar medium and properties of molecular clouds, MNRAS **436**(2): 1836–1851.

Rieder, S., Dobbs, C., Bending, T., Liow, K. Y. and Wurster, J. (2022). The formation and early evolution of embedded star clusters in spiral galaxies, MNRAS **509**(4): 6155–6168.

Saitoh, T. R., Daisaka, H., Kokubo, E., Makino, J., Okamoto, T., Tomisaka, K., Wada, K. and Yoshida, N. (2008). Toward First-Principle Simulations of Galaxy Formation: I. How Should We Choose Star-Formation Criteria in High-Resolution Simulations of Disk Galaxies?, PASJ **60**(4): 667–681.

Saitoh, T. R., Daisaka, H., Kokubo, E., Makino, J., Okamoto, T., Tomisaka, K., Wada, K. and Yoshida, N. (2009). Toward First-Principle Simulations of Galaxy Formation: II. Shock-Induced Starburst at a Collision Interface during the First Encounter of Interacting Galaxies, PASJ **61**: 481.

Schoettler, C., Parker, R. J. and de Bruijne, J. (2022). Constraining the initial conditions of NGC 2264 using ejected stars found in Gaia DR2, MNRAS **510**(3): 3178–3206.

Seshadri, A., Vig, S., Ghosh, S. K. and Ojha, D. K. (2024). Massive star formation in the hub-filament system of RCW 117, MNRAS **527**(2): 4244–4259.

Stoop, M., de Koter, A., Kaper, L., Brands, S., Portegies Zwart, S., Sana, H., Stoppa, F., Gieles, M., Mahy, L., Shenar, T., Guo, D., Nelemans, G. and Rieder, S. (2024). Two waves of massive stars running away from the young cluster R136, Nature **634**(8035): 809–812.

Strömgren, B. (1939). The Physical State of Interstellar Hydrogen., ApJ **89**: 526.

Tiongco, M. A., Vesperini, E. and Varri, A. L. (2016). Velocity anisotropy in tidally limited star clusters, MNRAS **455**(4): 3693–3701.

Tiongco, M. A., Vesperini, E. and Varri, A. L. (2017). Kinematical evolution of tidally limited star clusters: rotational properties, MNRAS **469**(1): 683–692.

Tiongco, M. A., Vesperini, E. and Varri, A. L. (2022). Early dynamical evolution of rotating star clusters in a tidal field, MNRAS **512**(2): 1584–1597.

Vesperini, E., Varri, A. L., McMillan, S. L. W. and Zepf, S. E. (2014). Kinematical fingerprints of star cluster early dynamical evolution., MNRAS **443**: L79–L83.

Wang, L., Iwasawa, M., Nitadori, K. and Makino, J. (2020). PETAR: a high-performance N-body code for modelling massive collisional stellar systems, MNRAS **497**(1): 536–555.

Wang, L., Nitadori, K. and Makino, J. (2020). A slow-down time-transformed symplectic integrator for solving the few-body problem, MNRAS **493**(3): 3398–3411.

Wong, T., Oudshoorn, L., Sofovich, E., Green, A., Shah, C., Indebetouw, R., Meixner, M., Hacar, A., Nayak, O., Tokuda, K., Bolatto, A. D., Chevance, M., De Marchi, G., Fukui, Y., Hirschauer, A. S., Jameson, K. E., Kalari, V., Lebouteiller, V., Looney, L. W., Madden, S. C., Onishi, T., Roman-Duval, J., Rubio, M. and Tielens, A. G. G. M. (2022). The 30 Doradus Molecular Cloud at 0.4 pc Resolution with the Atacama Large Millimeter/submillimeter Array: Physical Properties and the Boundedness of CO-emitting Structures, ApJ **932**(1): 47.

Wright, N. J., Jeffries, R. D., Jackson, R. J., Bayo, A., Bonito, R., Damiani, F., Kalari, V., Lanzafame, A. C., Pancino, E., Parker, R. J., Prisinzano, L., Randich, S., Vink, J. S., Alfaro, E. J., Bergemann, M., Franciosini, E., Gilmore, G., Gonneau, A., Hourihane, A., Jofré, P., Koposov, S. E., Lewis, J., Magrini, L., Micela, G., Morbidelli, L., Sacco, G. G., Worley, C. C. and Zaggia, S. (2019). The Gaia-ESO Survey: asymmetric expansion of the Lagoon Nebula cluster NGC 6530 from GES and Gaia DR2, MNRAS **486**(2): 2477–2493.

Wright, N. J., Jeffries, R. D., Jackson, R. J., Sacco, G. G., Arnold, B., Franciosini, E., Gilmore, G., Gonneau, A., Morbidelli, L., Prisinzano, L., Randich, S. and Worley, C. C. (2024). The Gaia-ESO Survey: 3D dynamics of young groups and clusters from GES and Gaia EDR3, MNRAS **533**(1): 705–728.

Wright, N. J. and Mamajek, E. E. (2018). The kinematics of the Scorpius-Centaurus OB association from Gaia DR1, MNRAS **476**(1): 381–398.

Zari, E., Brown, A. G. A. and de Zeeuw, P. T. (2019). Structure, kinematics, and ages of the young stellar populations in the Orion region, A&A **628**: A123.

Zhang, G.-Y., Andre, P., Menshchikov, A. and Li, J.-Z. (2024). Probing the filamentary nature of star formation in the California giant molecular cloud, *arXiv e-prints* p. arXiv:2406.08004.

Zhang, W., Zhou, J., Esimbek, J., Baan, W., He, Y., Tang, X., Li, D., Ji, W., Wu, G., Ma, Y., Li, J., Zhou, D., Tursun, K. and Komesh, T. (2024). Kinematics and star formation of hub-filament systems in W49A, *arXiv e-prints* p. arXiv:2406.08906.

Zucker, C. and Chen, H. H.-H. (2018). RadFil: A Python Package for Building and Fitting Radial Profiles for Interstellar Filaments, ApJ **864**(2): 152.

Chapter 5

Discussion and Future Work

5.1 Summary of Thesis Results

We have performed numerical simulations to study the response of a star cluster to evolution within its surrounding gas-rich environment during the very early stages of its evolution.

We began with simulations of a star cluster accreting gas from uniformly distributed background gas environments with varying densities and velocities. Our simulations show that interaction with the background gas strips bound gas from the star cluster. The amount of mass stripped depends on the gas properties but the stripped gas is not likely star forming. Because of the complex removal of gas from the cluster, typical Bondi-Hoyle accretion (Bondi 1952) prescriptions do not accurately describe the change in gas mass of the cluster. We then considered a star cluster accreting from dense filaments of gas with parameters that were inspired by observations of star forming regions. Accretion from these filaments provides the star cluster with bound, star forming material regardless of the number of filaments or their parameters (i.e. mass or density). When we included a background gas distribution alongside filamentary accretion onto a star cluster, we found that the cluster was better able to hold on to its accreted material thanks to the added pressure from the background gas.

We then performed controlled simulations to study the role played by mergers that are not head-on in the enhancement of cluster rotation. This acts as a direct followup to the work performed in Karam (2021). This controlled study showed that off axis mergers increase the angular momentum induced onto the resultant cluster while also leading to less gravitational unbinding of stars and gas. As well, off-axis mergers were more likely to create non-monolithic clusters (clusters with two identifiable cores). We then took three regions from the Howard et al. (2018) giant molecular cloud simulations that contained

gas and sink particles meant to represent star clusters, resolved the sink particles as star clusters, and studied the effects of mergers inside a gas-rich environment on the dynamics of the clusters involved. In every simulation performed, we found that mergers produce clusters that are expanding anisotropically, and rotating similar to recent *Gaia* space telescope observations of young star clusters. The rotation is concentrated in the central regions (within $3L_{50}$ where L_{50} is the radius enclosing half of the cluster mass) of the star cluster unless there is accretion of stars from a nearby cluster. Those accreted stars are in the cluster outskirts and contribute significantly to the total cluster angular momentum. Lastly from this study, we find that background environment is vital in promoting cluster mergers. A simulation of one region that normally led to a cluster merger did not lead to said merger when the background gas distribution was removed.

Finally, we improved our computational framework to study mergers in gas-rich environments with the inclusion of prescriptions for star formation and stellar feedback. We reran the `region1` simulation from Chapter 3 with this improved framework to constrain the role played by star formation and stellar feedback in shaping star cluster dynamics. The merger simulated resulted in a drastic increase in the formation of bound stars and, in turn, the stellar mass of the resultant cluster. Star formation also took place in clumps along a nearby filament that were then accreted onto the merged cluster. These clumps were identifiable in an analysis of the expansion of the stellar component of the cluster. This, along with flattening of the star cluster in position space, lead to the formation of a non-spherical cluster as a result of the merger process. Star formation also leads to an increase in the overall velocity dispersion, expansion, and rotation of the cluster. A disproportionate amount of rotation comes from stars that were accreted onto the cluster. We then analyzed the cluster dynamics after it had removed most of its background gas and found that the merger induced a velocity anisotropy profile similar to that expected from core collapse of older star clusters. By comparing with the literature, we find that this profile is likely to have an effect on the long term evolution of the cluster. Lastly, we find that the dynamical signatures of the merger are still present by the time the cluster has removed most of its surrounding gas.

Our results point towards a need for higher resolution of star cluster formation with the inclusion of accurate background gas distributions. It is clear from our simulations that background gas plays a vital role in shaping the dynamics of clusters as they assemble inside giant molecular clouds. Not only does the background gas promote mergers, but the mergers themselves impart unique dynamical signatures on the clusters involved

that can last until they are observable thus drawing a direct connection between simulations and observations. These observable signatures are heightened when accounting for stars that form from the dense gas as these stars inherit their positions and velocities from the gas. Filaments that accrete material onto young star clusters continuously provide the cluster with angular momentum allowing it to continue rotating until the gas is removed.

We show that star cluster formation is not a spherical process, and that this can be seen when analyzing the dynamics of the cluster as it forms.

5.2 Future Work: Realistic Simulation Initial Conditions

To fully understand the dynamics associated with star cluster assembly inside molecular clouds, a range of molecular cloud initial conditions needs to be simulated. Molecular clouds with varying masses, surface densities, filamentary structures, and virial parameters will all give rise to clusters that, when compared against each other, can tell us the important molecular cloud parameters (e.g. gas density, velocity dispersion, or filament population) that shape star cluster dynamics. The simulations from which we took our initial conditions for the simulations presented in Chapters 3 and 4 of this thesis were themselves initialized as spheres. While these simulations have given us important insight into the star formation process, there is a step we can take to improve on them: inheriting our molecular cloud initial conditions directly from observations.

This process has been performed by Sills et al. (2023), who took observations from Hacar et al. (2017) and Friesen et al. (2017) to simulate star cluster buildup inside the Orion Nebula Cluster (ONC). The ONC, however, is a very simple star forming region that contains only one filament. As many star forming regions contain overlapping filaments in hub-filament systems, it is important to consider a wide range of gas morphologies to gain a full picture of star cluster formation. We will begin this process by considering the far infrared observations of star forming clouds along the Milky Way's Gould Belt from the *Herschel* space telescope which are cataloged in the Herschel Gould Belt Survey (HGBS) (André et al. 2010). The HGBS offers an extensive view of the star forming regions along the Gould Belt and provides column density and temperature data for the gas that comprises these regions. Using similar methods to those used in Chapter 3 of this thesis to convert from grid data into SPH particle data, we will convert column density maps from the HGBS into SPH particle representations and use the temperature maps to calculate the internal energies of each particle using equation 1.8.

The HGBS contains maps of the column density and temperature of each region imaged. For the information regarding the gas velocities and velocity dispersions, we will turn to the Green Bank Ammonia Survey (GAS) which acts as a kinematic counterpart to the HGBS. The data presented in GAS are derived from radio observations performed using the Green Bank Observatory and cover the same star forming regions as the HGBS (Friesen et al. 2017). Combining these observations with the HGBS provides us with the parameters necessary to simulate these star forming regions and study the clusters that may form.

We can also move beyond the Gould Belt in search of star cluster formation initial conditions. Since the Atacama Large Millimeter Array (*ALMA*) began observing, there has been an enormous release of detailed spectrometry of the gas present in nearby star forming regions at unprecedented resolutions. An example of such observations are those presented as part of the ALMA-IMF program (Motte et al. 2022). These are low mass ($\approx 10^3 - 10^4$ $M_\odot$) clouds with a wide range of phase space morphologies that are likely to produce low mass star clusters ($\approx 10^2 - 10^3$ $M_\odot$). The range in phase space morphologies will have an affect on the final cluster dynamics which we will constrain. To study the formation of more massive star clusters, we will consider observations of hub-filament systems (e.g. Fukui et al. 2019, Rawat et al. 2024, Shen et al. 2024, Zhang et al. 2024) whose masses can reach up to 10^5 $M_\odot$. The clusters that form from these simulations will have a range of phase space distributions. We can then simulate these clusters forward with the inclusion of a galactic potential to determine which clusters will survive and what they will look like much later in their life.

In recent years, astronomers have come to terms with the necessity of including gas in their star cluster simulations. Our work shows that the phase space distribution of this gas matters, and is strong evidence that we should move beyond spherical initial conditions. As telescopes continue to improve, so too should our simulation conditions.

Bibliography

André, P., Men'shchikov, A., Bontemps, S., Könyves, V., Motte, F., Schneider, N., Didelon, P., Minier, V., Saraceno, P., Ward-Thompson, D., di Francesco, J., White, G., Molinari, S., Testi, L., Abergel, A., Griffin, M., Henning, T., Royer, P., Merín, B., Vavrek, R., Attard, M., Arzoumanian, D., Wilson, C. D., Ade, P., Aussel, H., Baluteau, J. P., Benedettini, M., Bernard, J. P., Blommaert, J. A. D. L., Cambrésy, L., Cox, P., di Giorgio, A., Hargrave, P., Hennemann, M., Huang, M., Kirk, J., Krause, O., Launhardt, R., Leeks, S., Le Pennec, J., Li, J. Z., Martin, P. G., Maury, A., Olofsson, G., Omont, A., Peretto, N., Pezzuto, S., Prusti, T., Roussel, H., Russeil, D., Sauvage, M., Sibthorpe, B., Sicilia-Aguilar, A., Spinoglio, L., Waelkens, C., Woodcraft, A. and Zavagno, A. (2010). From filamentary clouds to prestellar cores to the stellar IMF: Initial highlights from the Herschel Gould Belt Survey, A&A **518**: L102.

Bondi, H. (1952). On spherically symmetrical accretion, MNRAS **112**: 195.

Friesen, R. K., Pineda, J. E., co-PIs, Rosolowsky, E., Alves, F., Chacón-Tanarro, A., How-Huan Chen, H., Chun-Yuan Chen, M., Di Francesco, J., Keown, J., Kirk, H., Punanova, A., Seo, Y., Shirley, Y., Ginsburg, A., Hall, C., Offner, S. S. R., Singh, A., Arce, H. G., Caselli, P., Goodman, A. A., Martin, P. G., Matzner, C., Myers, P. C., Redaelli, E. and GAS Collaboration (2017). The Green Bank Ammonia Survey: First Results of NH_3 Mapping of the Gould Belt, ApJ **843**(1): 63.

Fukui, Y., Tokuda, K., Saigo, K., Harada, R., Tachihara, K., Tsuge, K., Inoue, T., Torii, K., Nishimura, A., Zahorecz, S., Nayak, O., Meixner, M., Minamidani, T., Kawamura, A., Mizuno, N., Indebetouw, R., Sewiło, M., Madden, S., Galametz, M., Lebouteiller, V., Chen, C. H. R. and Onishi, T. (2019). An ALMA View of Molecular Filaments in the Large Magellanic Cloud. I. The Formation of High-mass Stars and Pillars in the N159E-Papillon Nebula Triggered by a Cloud-Cloud Collision, ApJ **886**(1): 14.

Hacar, A., Alves, J., Tafalla, M. and Goicoechea, J. R. (2017). Gravitational collapse of the OMC-1 region, A&A **602**: L2.

Howard, C. S., Pudritz, R. E. and Harris, W. E. (2018). A universal route for the formation of massive star clusters in giant molecular clouds, *Nature Astronomy* **2**: 725–730.

Karam, J. (2021). *Modelling young massive cluster formation: Mergers*, Master's thesis, McMaster University.
URL: *http://hdl.handle.net/11375/27342*

Motte, F., Bontemps, S., Csengeri, T., Pouteau, Y., Louvet, F., Stutz, A. M., Cunningham, N., López-Sepulcre, A., Brouillet, N., Galván-Madrid, R., Ginsburg, A., Maud, L., Men'shchikov, A., Nakamura, F., Nony, T., Sanhueza, P., Álvarez-Gutiérrez, R. H., Armante, M., Baug, T., Bonfand, M., Busquet, G., Chapillon, E., Díaz-González, D., Fernández-López, M., Guzmán, A. E., Herpin, F., Liu, H. L., Olguin, F., Towner, A. P. M., Bally, J., Battersby, C., Braine, J., Bronfman, L., Chen, H. R. V., Dell'Ova, P., Di Francesco, J., González, M., Gusdorf, A., Hennebelle, P., Izumi, N., Joncour, I., Lee, Y. N., Lefloch, B., Lesaffre, P., Lu, X., Menten, K. M., Mignon-Risse, R., Molet, J., Moraux, E., Mundy, L., Nguyen Luong, Q., Reyes, N., Reyes Reyes, S. D., Robitaille, J. F., Rosolowsky, E., Sandoval-Garrido, N. A., Schuller, F., Svoboda, B., Tatematsu, K., Thomasson, B., Walker, D., Wu, B., Whitworth, A. P. and Wyrowski, F. (2022). ALMA-IMF. I. Investigating the origin of stellar masses: Introduction to the Large Program and first results, A&A **662**: A8.

Rawat, V., Samal, M. R., Walker, D. L., Ojha, D. K., Tej, A., Zavagno, A., Zhang, C. P., Elia, D., Dutta, S., Jose, J., Eswaraiah, C. and Sharma, E. (2024). The Giant Molecular Cloud G148.24+00.41: gas properties, kinematics, and cluster formation at the nexus of filamentary flows, MNRAS **528**(2): 2199–2219.

Shen, X., Liu, H.-L., Ren, Z., Tej, A., Li, D., Liu, H. B., Fuller, G. A., Xie, J., Jiao, S., Yang, A., Koch, P. M., Xu, F., Sanhueza, P., Diep, P. N., Peretto, N., Yadav, R. K., Kramer, B. H., Sugiyama, K., Rawlings, M. G., Lee, C. W., Tatematsu, K., Harsono, D., Eden, D., Kwon, W., Tsai, C.-W., White, G. J., Kim, K.-T., Liu, T., Wang, K., Zhang, S., Jiao, W., Yang, D., Das, S. R., Wu, J. and Wang, C. (2024). JCMT 850 μm Continuum Observations of Density Structures in the G35 Molecular Complex, ApJ **974**(2): 239.

Sills, A., Rieder, S., Buckner, A. S. M., Hacar, A., Portegies Zwart, S. and Teixeira, P. S. (2023). Using molecular gas observations to guide initial conditions for star cluster simulations, MNRAS **519**(3): 4142–4151.

Zhang, W., Zhou, J., Esimbek, J., Baan, W., He, Y., Tang, X., Li, D., Ji, W., Wu, G., Ma, Y., Li, J., Zhou, D., Tursun, K. and Komesh, T. (2024). Kinematics and star formation of hub-filament systems in W49A, A&A **688**: A99.